#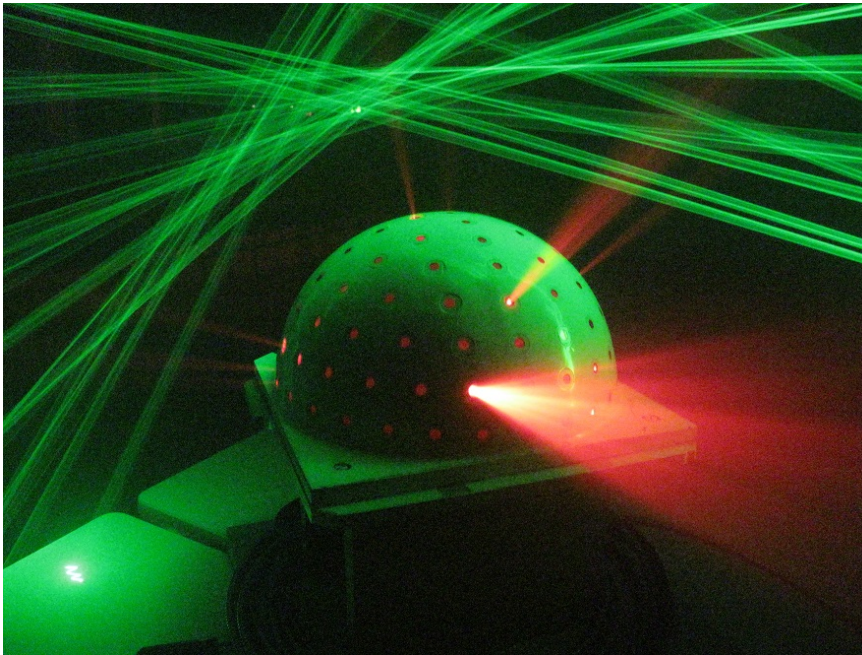 Simultaneous measurement of spectral sky radiance: Development, characterization and validation of a non-scanning multidirectional spectroradiometer (MUDIS)

Von der Fakultät für Mathematik und Physik
der Gottfried Wilhelm Leibniz Universität Hannover
zur Erlangung des Grades

Doktor der Naturwissenschaften
- Dr. rer. nat. -

genehmigte Dissertation
von
Dipl.-Met. Stefan Riechelmann
geboren am 21.01.1982 in Großburgwedel

2014

Kurzfassung

Die spektrale und räumliche Verteilung der Strahldichte des Himmels unterliegt auf Grund von Wolken, Aerosolen und Variation des Sonnenstandes großen zeitlichen Schwankungen. Bisherige Instrumente, welche in der Lage sind die Strahldichte des Himmels in hoher spektraler Auflösung im UV zu erfassen, basieren auf einem Scanprinzip, bei dem die räumliche Verteilung durch sequentielle Messungen unterschiedlicher Zenit- und Azimutwinkel am Himmel erfasst wird. Besonders die zeitliche Variation von Wolken führt während dieses Scanprozesses zu einer Verzerrung der gemessenen Strahldichte des Himmels. Aus diesem Grund wurde ein nichtscannendes, multidirektionales Spektralradiometer (MUDIS) entwickelt. Es ist in der Lage die spektrale Strahldichte in 113 Richtungen zeitgleich in weniger als zwei Sekunden in einem Wellenlängenbereich von 250 bis 680 nm zu erfassen.

Für die Kalibrierung und Validierung der mit MUDIS durchgeführten Strahldichtemessungen des Himmels wurde ein Instrumentenvergleich mit einem punktscannenden CCD Zeilenspektrometer (SCCD) durchgeführt. Der systematische Unterschied aller MUDIS/SCCD Quotienten der spektralen Strahldichte, aufgenommen bei Cirrus fibratus-, Stratus- und Cumulus-Bewölkung, ist kleiner als 3% zwischen 310 und 600 nm. Bei Cirrus fibratus-Bewölkung wurde die geringste 1σ Standardabweichung der Quotienten mit 4%-8% zwischen 310 und 600 nm beobachtet. Strahldichtemessungen bei durchbrochener Bewölkung und bedecktem Himmel weisen höhere Standardabweichungen von 6%-18% auf. Aktinische Bestrahlungsstärke, abgeleitet von MUDIS und SCCD Strahldichtemessungen, zeigen eine gute Übereinstimmung mit einem systematischen Unterschied von weniger als 3% und einer 1σ Standardabweichung von weniger als 3% bei 320 und 500 nm.

Zusätzlich wurden Strahldichtemessungen im Zenit mit MUDIS und einem UV Spektroradiometer, zertifiziert vom Network for the Detection of Atmospheric Composition Changes (NDACC), verglichen. Der mittlere systematische Unterschied, berechnet aus allen Quotienten des MUDIS und NDACC-Instrumentes die in acht Messtagen aufgenommen wurden, ist kleiner als 6% zwischen 310 und 600 nm und weist eine 1σ Standardabweichung von 4%-13% auf. Trotz des geringen systematischen Unterschieds treten Variationen des Tagesgangs in Abhängigkeit der vorherrschenden meteorologischen Bedingungen auf. Beispielsweise wird bei wolkenfreiem Zenit sowohl bei Vergleichen mit dem NDACC-Instrument als auch bei Vergleichen mit dem SCCD ein Tagesgang des systematischen Unterschieds zu MUDIS von 20% beobachtet.

Die bei den Instrumentenvergleichen beobachteten Variationen werden durch die Kombination aus Sichtfeldunterschieden, unerwünschter Verkippungen der MUDIS Blickrichtungen und einigen weiteren Geräteeigenschaften verursacht. Die Parameter können durch Gerätevergleiche nicht einzeln untersucht werden, da sie voneinander abhängen und zudem nicht änderbar sind. Aus diesem Grund wurde ein Algorithmus entwickelt, der Messungen mit variablen Geräteeigenschaften auf der Basis von Allskybildern simuliert. Der Algorithmus ermöglicht die Durchführung von Parameterstudien unter realistischen Bedingungen basierend auf Allskybildern, welche an den Tagen der Vergleichskampagnen aufgenommen wurden. Die Parameterstudien führen zu einem besseren Verständnis des Einflusses der untersuchten Geräteparameter auf die Strahldichtemessungen von MUDIS. Auf diesem Weg konnte der beobachtete Tagesgang des systematischen Unterschieds zwischen MUDIS Zenitmessungen und den Vergleichsgeräten auf eine 2,5° Neigung der Zenitblickrichtung von MUDIS zurückgeführt werden. Die durchgeführten Parameterstudien ermöglichen eine Korrektur der MUDIS Blickrichtungen und sind ein nützliches Werkzeug für die Bewertung von Geräteunterschieden bei zukünftigen Instrumentenvergleichen.

Schlagworte: UV Spektroradiometrie, UV Strahldichte, UV Imaging Spektroradiometer

Abstract

The spectral and spatial distribution of sky radiance is rapidly changing due to the influence of clouds, solar elevation and aerosols. Current instruments that measure sky radiance in a high spectral resolution in the UV rely on a point scanning process, where the spatial distribution is derived by performing sequential measurements at different zenith and azimuth angles of the sky. Especially the temporal variation of clouds during the scanning process leads to a severe distortion of the measured sky radiance. Therefore, a non-scanning multidirectional spectroradiometer (MUDIS) has been developed. It is capable of measuring spectral radiance in 113 directions simultaneously in less than two seconds with an operational wavelength range between 250 and 680 nm.

In order to calibrate and validate sky radiance measurements performed with MUDIS, an instrument comparison with a point scanning charged coupled device array spectroradiometer (SCCD) has been carried out. The systematic difference of all MUDIS/SCCD spectral radiance measurement ratios derived under translucent (cirrus fibratus), overcast (stratus) and broken clouds (cumulus) is less than 3% between 310 and 600 nm. The lowest 1σ standard deviation of the ratios is observed during cirrus fibratus covered sky with 4%-8% between 310 and 600 nm. Measurements performed during broken clouds and overcast sky show a higher standard deviation between 6% and 18%. Actinic irradiance derived from MUDIS and SCCD sky radiance measurements shows a good agreement with a systematic difference of less than 3% and a 1σ standard deviation of less than 3% for 320 and 500 nm.

In addition, diurnal zenith radiance measurements performed with MUDIS and a UV spectroradiometer certified by the Network for the Detection of Atmospheric Composition Changes (NDACC) were compared. The mean systematic difference calculated from eight days of MUDIS/NDACC zenith radiance ratios is less than 6% between 310 and 600 nm with a 1σ standard deviation of 4%-13% between 310 and 600 nm. However, diurnal deviations during specific meteorological conditions and at specific times of the day can be observed. For instance, a 20% diurnal shift of the systematic difference between MUDIS and both NDACC and SCCD zenith radiance measurements was observed for a cloudless zenith.

The combination of field of view differences, unintended tilts of the MUDIS viewing angles and several additional instrument parameters is responsible for the variations observed during the instrument comparisons. These parameters cannot be examined separately by intercomparison, since they are not changeable and depend on each other. Therefore, an algorithm has been developed that simulates measurements with variable instrument parameters based on allsky pictures. The algorithm enabled the performance of parameter studies under realistic conditions based on allsky pictures taken on the measurement days of the comparison campaign. The studies lead to a better understanding of the impact of the examined instrument parameters on MUDIS sky radiance measurements. This way the observed diurnal shift of the zenith sky radiance could be traced back to a 2.5° eastward tilt of the MUDIS zenith point. The conducted parameter studies enable the correction of the MUDIS pattern and are a useful tool for the evaluation of instrument differences during future intercomparisons.

Keywords: UV spectroradiometry, UV sky radiance, UV imaging spectroradiometer

Contents

List of Figures

List of Tables

List of Symbols

Abbreviations

Ac	Altocumulus
ADC	Analog Digital Converter
AMS	Allsky-based Measurement Simulator
Ca	Calcium
Ci	Cirrus
Cu	Cumulus
CCD	Charged Coupled Device
DT	Detection Threshold
FOV	Field Of View
FWHM	Full Width at Half Maximum
GAW	Global Atmosphere Watch
HgAr	Mercury Argon
HSI	Hemispherical Sky Imager
IMuK	Institute of Meteorology and Climatology
Kr	Krypton
MB	MegaByte
MUDIS	MUltiDIrectional Spectroradiometer
NDACC	Network for the Detection of Atmospheric Composition Changes
NER	Noise Equivalent Radiance
NIR	Near InfraRed
NLF	Non-Linearity Factor
SCCD	Scanning Charged Coupled Device array spectroradiometer
SDF	Stray light Distribution Function
SL	Stray Light
SLC	Stray Light Correction
Sc	Stratocumulus
St	Stratus
UTC	Universal Time Coordinated
UV	UltraViolet
VIS	VISible
WMO	World Meteorological Organization

Greek Symbols

α	Angular tilt
β	Horizontal Angular tilt
λ	Wavelength
Ω	Solid angle
φ	Azimuth angle
σ	Standard deviation
θ	Zenith angle

Latin Symbols

A	Area
C	Count value
E	Spectral irradiance
F_{DIFF}	Spectral actinic irradiance
L_λ	Spectral radiance
n	Number of layers
p	Pixel
P	Point
Q	Radiant Energy
R	Bidirectional reflectance factor
S	Sensitivity
t	Time
U	Uncertainty
X	Signal
Y	Lamp housing measurement
Z	Angular response

Indices

Ψ_λ	Spectral quantity
Ψ_{DARK}	Dark current measurements
Ψ_{Lab}	Lab measurement
Ψ_{MUDIS}	MUDIS measurement
Ψ_t	Measurement at time t
Ψ_{STRAY}	Stray light measurement
Ψ_{SCCD}	SCCD measurement

1 Introduction

All constituents of the Earth's atmosphere interact with the radiation originated from the sun in form of scattering and absorption processes. This interaction results in a complex radiation field at ground level with a high spatial, spectral and temporal variation. Diffuse radiation originating from the sky hemisphere contributes significantly to the total amount of radiation reaching the ground. The diffuse radiation originating from the sky can be expressed by the spectral radiance, defined as the spectral radiant flux emitted per solid angle, which falls with a certain angle on a receiving surface. Measurements of the spectral sky radiance provide spatial, spectral and temporal information of the radiation field at a measurement site. Possible applications are the calculation of power yield of tilted solar cells at a specific location (Beringer et al., 2011) or the determination of light doses received by complex objects like the human body (Seckmeyer et al., 2013). Spectral sky radiance also contains information due to its interaction with the atmosphere. It can be used to derive aerosol properties (Dubovik and King, 2000), cloud properties (Hirsch et al., 2012) as well as aerosol and trace gas profiles (Hönninger et al., 2004).

A measurement of spectral sky radiance is a three dimensional dataset, consisting of two spatial dimensions (zenith angle, azimuth angle) and one spectral dimension (wavelength) and is referred to as a datacube (Hagen et al., 2012). By sequentially measuring datacubes, time is added as a fourth dimension in spectral sky radiance measurements. There are many different instruments, capable of measuring datacubes of sky radiance in varying spatial, spectral and temporal resolutions. The following enumeration gives a brief overview over the main instrument categories relevant for observations of the sky:

- **Wavelength and point scanning devices**
  Measurements of spectral sky radiance were performed with spectroradiometers based on wavelength scanning double monochromators e.g., by Blumthaler et al. (1996), Weihs et al. (2000), Wuttke et al. (2006) and Cordero et al. (2013). Double monochromator spectroradiometers fulfill high standards in terms of instrument stability, stray light reduction and wavelength resolution and thus provide excellent performance in the UV. They also have been thoroughly tested through instrument intercomparison campaigns (Lantz et al., 2008; Pissulla et al., 2009). However, due to their single entrance optics and their wavelength scanning principle these instruments have to scan both spatial and spectral dimensions. In this work the double monochromator-based spectroradiometer developed by Wuttke (2005) is only used for measurements of spectral radiance in a single direction of the sky. Measuring a single spectrum in a wavelength range between 280 and 1000 nm with a spectral resolution of 0.25 nm in the UV and 1 nm in the VIS part of the spectrum takes about 21 min.

- **Point scanning array devices**
  To overcome the shortage of wavelength scanning spectroradiometers, systems based on charged coupled device (CCD) array spectrometers instead of double monochromators have been developed e.g., by Kouremeti et al. (2008) and Dunagan et al. (2013). These instruments are capable of measuring their whole operational wavelength range simultaneously. In this thesis a point scanning CCD array spectroradiometer with an operational wavelength range between 265 and 900 nm is used. The instrument is capable

of acquiring sky radiance with a spatial resolution of 113 directions in the sky in about 12 min due to the speed of the positioning device turning the entrance optics and the measuring speed of the spectrometer.

- **Hemispheric sky imaging devices**
  A technical solution, capable of measuring sky radiance with a high spatial and temporal resolution, is provided by commercially available compact cameras equipped with fish-eye lenses (Román et al., 2012; Tohsing et al., 2013). Unfortunately, these instruments provide only very limited spectral information at three broad wavebands in the visible range of the spectrum, namely the red, green and blue channel. Since no spatial or spectral scanning process is involved in the acquisition, these instruments can be referred to as snapshot instruments. Another downside of commercial compact cameras is their poor dynamic range. It is impossible to acquire bright regions of the sky like the circumsolar region and comparably dark patches of blue sky with the same exposure time. This can be overcome by high dynamic range acquisitions where pictures with different exposure times are taken and merged together (Tohsing et al., 2013). Unfortunately, this technique defies the snapshot nature of these devices, leading to scanning artifacts due to moving clouds during the acquisition period.

- **Wavelength scanning sky imaging devices**
  More sophisticated hemispheric sky imaging devices consist of scientific grade monochromatic cameras combined with fish-eye lenses and tunable filters (Hardeberg et al., 2002) or Fabry-Perot interferometers (Pisani and Zucco, 2009). Since these devices are based on wavelength scanning techniques, a considerable measurement time is needed for the acquisition of spectra with wavelength sampling intervals comparable to CCD array spectroradiometers. Since there is currently no UV transmitting fish-eye lens commercially available, UV sky radiance measurements of the whole hemisphere at once cannot be performed by these techniques yet.

- **Snapshot spectral imaging devices**
  Instruments that measure a datacube of spectral radiance with non-scanning techniques in a single acquisition are commonly referred to as snapshot imaging spectrometers (Hagen et al., 2012). There are at least 13 different snapshot technologies which are summarized in an excellent review article by Hagen and Kudenov (2013). Every technique boils down to the general problem of measuring a three dimensional quantity with a two dimensional sensor element. A high spectral resolution therefore inevitably leads to a low spatial resolution and vice versa.

Snapshot techniques are especially promising for the astronomy community and for the development of medical diagnostic tools. Both applications benefit from the high light collection efficiency of these techniques and the resulting measurement speed. Due to these two main application areas most snapshot techniques provide high spatial resolutions of a rather small field of view, consequentially the spectral resolution is rather low. An example for a state of the art snapshot imaging spectrometer is presented by Bedard et al. (2013). The instrument is capable of measuring datacubes with a spatial resolution of $350x355$ pixels and a spectral resolution of 41 intervals in the visible part of the spectrum, each interval providing a bandwidth of 6–16 nm. Such instrument characteristics would not be feasible for the calculation of erythemally or vitamin D weighted doses received by a human body, since for these applications the UV sky radiance needs to be acquired with a high wavelength accuracy and

a small wavelength sampling interval. This is crucial in order to reduce uncertainties due to the exponential increase of radiance in the UV part of the spectrum (Seckmeyer et al., 2013; Cordero et al., 2008).

A feasible instrument for snapshot measurements of sky radiance with a high spectral resolution in the UV part of the spectrum has therefore been developed in this thesis. The instrument is capable of measuring UV sky radiance in 113 directions simultaneously in less than two seconds, which is especially useful when measuring under rapidly changing sky radiance conditions due to cloud movement and change of cloud coverage (Kuchinke et al., 2004).

In order to validate the developed instrument, comparisons with a point scanning CCD array spectroradiometer and a double monochromator-based spectroradiometer were conducted. While plenty of comparisons of instruments measuring spectral global irradiance are found in the literature, only a single publication concerning the comparison of instruments measuring spectral sky radiance was found (Pissulla et al., 2009). The intercomparison methods used by Pissulla et al. (2009) were limited to spectral ratios at around noon time and to the diurnal variation of only 12 measurements for three wavelengths (325, 360 and 420 nm). In this work, the comparison methods for sky radiance spectroradiometers are further developed by additionally conducting a statistical and an integral comparison. Especially the statistical approach enables the examination of instrument performance with regard to various weather conditions.

Variations determined during the instrument comparisons result from the combination of field of view differences, unintended tilts of the MUDIS viewing angles, and several additional instrument parameters. Since most parameters are not changeable and also depend on each other, it is impossible to examine those parameters separately by intercomparison methods. Therefore, an algorithm has been developed that simulates measurements with variable instrument parameters based on allsky pictures. This tool enables instrument parameter studies which help to understand systematic and random differences of sky radiance measurements performed with different spectroradiometers.

2 Instruments and Methods

This chapter provides a brief overview of the procedures and instruments used in this work. A definition for sky radiance is introduced and the three spectroradiometers as well as the allsky camera system used in this thesis are presented. In addition, the calibration method that is used in this thesis in order to derive absolute radiance measurements is discussed in this chapter. Finally, a calculation method for the detection threshold of spectroradiometers is presented.

2.1 Spectral Sky Radiance

According to Seckmeyer et al. (2010) the spectral radiance L_λ is defined as "[...] the radiant energy dQ per time interval dt, per wavelength interval $d\lambda$, per area dA, and per solid angle $d\Omega$ on a receiver oriented normal to the source":

$$L_\lambda = \frac{d^3 Q}{dt \, d\lambda \, dA \, d\Omega}.$$ (2.1)

In this thesis only spectral radiance from the upper hemisphere, excluding the direct radiance from the sun, is measured, therefore it is denoted as spectral sky radiance. It has the units $\mathrm{W\,m^{-2}\,nm^{-1}\,sr^{-1}}$.

2.2 Double Monochromator-based Spectroradiometer

A double monochromator-based spectroradiometer, which is certified for the Network for the Detection of Atmospheric Composition Change (NDACC), has been developed in the past by Wuttke (2005) at the Institute of Meteorology and Climatology (IMuK). The instrument consists of three integral parts: A DTMc300 double monochromator (Bentham Instruments Ltd., Reading, United Kingdom), a radiance entrance optics with a field of view (FOV) of approx. 5° and an optical fiber bundle connecting the monochromator and the entrance optics. Measurements are performed in the wavelength range between 280 and 1000 nm with a bandwidth of 0.25 nm in the UV and 1.0 nm in the VIS part of the spectrum. The instrument is operated in a weatherproof and temperature stabilized box, providing a 20°C ambient temperature with a variation of less than ±1°C. Due to its superior stray light reduction and wavelength accuracy the NDACC instrument is used as a reference spectroradiometer. However, the measurement of a single spectrum takes about 21 min, therefore only zenith sky radiance measurements were performed.

2.3 Point scanning CCD Array Spectroradiometer

The first sky radiance measurements conducted with a CCD array spectroradiometer at the IMuK were performed by Pissulla (2006). Comparable to the NDACC instrument the CCD array spectrometer is connected to a 5° FOV radiance entrance optics via a bundle of optical fibers. The entrance optics is mounted on a positioning unit that is capable of scanning a desired pattern of points in the hemisphere sequentially (Figure 2.1). The instrument is therefore referred to as a point scanning CCD array spectroradiometer (SCCD). In this thesis

the SCCD has been further developed: The former "SD2000" spectrometer (Ocean Optics, Dunedin, Florida, USA) has been replaced with a "BlackComet" spectrometer (StellarNet Inc., Tampa, Florida, USA), providing a smaller bandwidth due to a smaller entrance slit and a higher dynamic range due to a 16 bit analogue-digital-converter (ADC). Also a post-measurement stray light correction algorithm after Kreuter and Blumthaler (2009) has been applied, enhancing the measurement quality in the UV part of the spectrum. The operational wavelength range of the instrument is 265 to 900 nm with a bandwidth varying between 0.7 and 1.8 nm. The instrument is also operated in a weatherproof and temperature stabilized box, providing a 20°C ambient temperature with a variation of less than ±1°C. A detailed instrument characterization and a description of the applied correction algorithms is provided in Section 3.1.
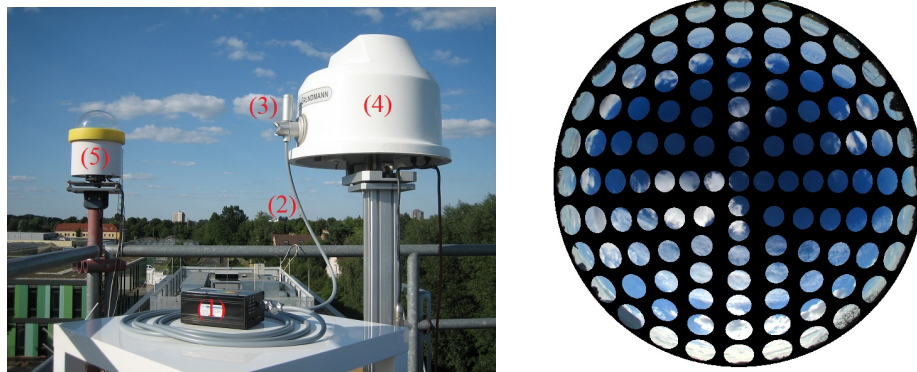
Figure 2.1: The left picture shows the SCCD (1) connected by an optical fiber bundle (2) to an entrance optics (3) which can be directed by a positioning unit (4) to a desired direction of the sky. In the background to the left the hemispherical sky imager (5) is mounted to the ceiling of the IMuK measuring platform. The right picture shows the 113 points scan pattern used by the SCCD to measure sky radiance.

2.4 Multidirectional Hyperspectral Imaging Spectrometer

The main part of the multidirectional spectroradiometer (MUDIS), developed in this thesis, is an Offner hyperspectral imager. This device consists of a UV-sensitive CCD camera (PCO AG, Kelheim, Germany) and an Offner imaging spectrometer (Headwall Photonics, Inc., Fitchburg, USA). The working principle of an Offner hyperspectral imager is shown in Figure 2.2. Light entering the imaging spectrometer through its entrance slit is collimated before hitting a grating where the light is dispersed. After the dispersed light is focused it is detected by the CCD camera sensor which is placed in the focal plane of the spectrometer. The spatial distribution of the entering light along the slit is therefore projected along the y-axis of the sensor and the corresponding spectrum is dispersed along the x-axis.

3D datacubes can be captured with this imager either by scanning one of the two spatial dimensions or by acquiring a limited number of points of a scenery simultaneously by an image slicing technique (Hagen and Kudenov, 2013). Typical spatial scanning instruments are so called pushbroom imagers which are often used in airborne applications (e.g., Davis et al., 2002). The pushbroom principle is shown in Figure 2.2(a). A scenery, e.g., the ground from the perspective of an airplane, is seen by the imager. The entrance slit limits the field of view of the camera lens to a narrow line vertical to the flight direction. A single acquisition of the
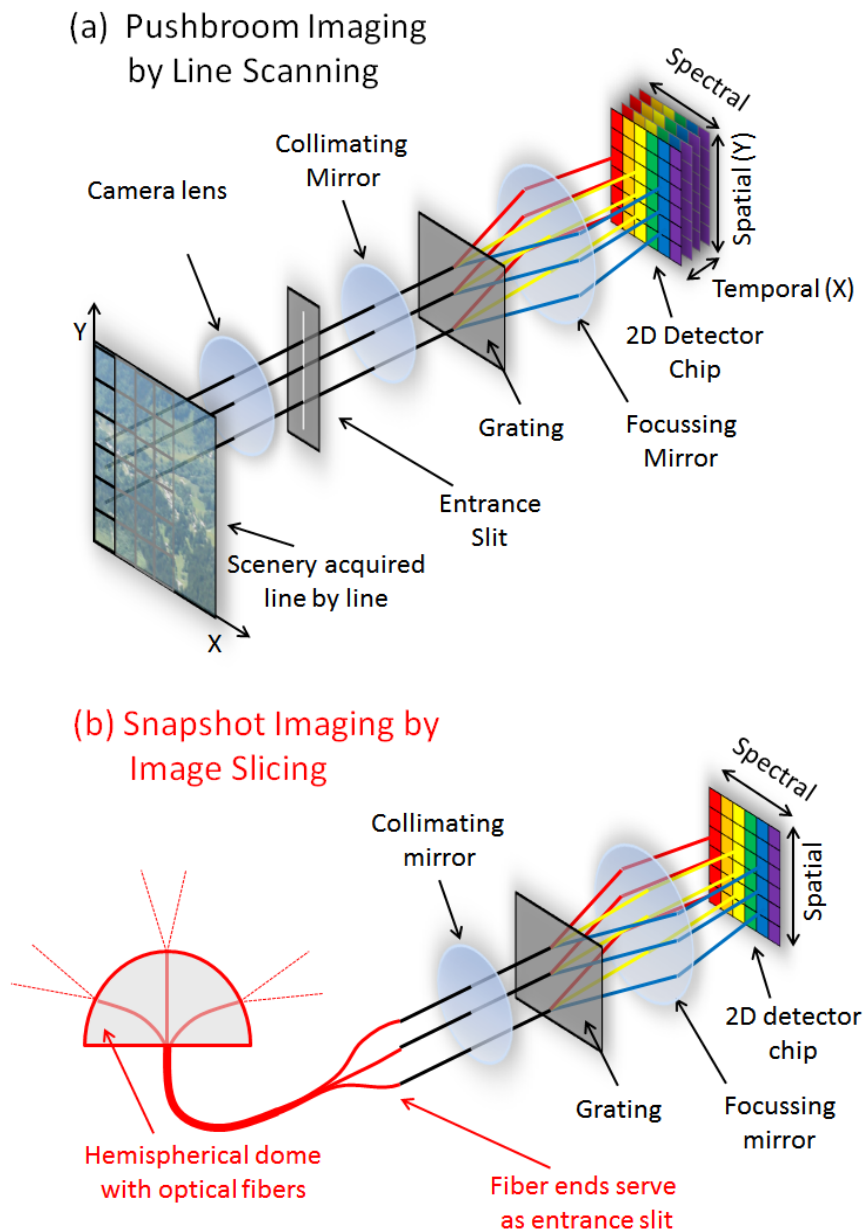
Figure 2.2: Sketch (a) shows the working principle of a pushbroom imager: An observed scenery is sliced in columns and the columns are measured subsequently by scanning along the x-axis. Sketch (b) shows the principle of a snapshot imager: A bundle of fibers is attached to the entrance of the imager. At the other end of the bundle each fiber points to a specific direction at the sky.

imager captures the spectral radiance received from this line with a certain spatial and spectral resolution. The continuous acquisition of lines during aircraft movement results in the spectral measurement of the whole scenery. The process is comparable with pushing a broom over the scenery; hence the term pushbroom imaging has become common in literature.

In this work an image slicing technique based on optical fibers (Kapany, 1958), as shown in Figure 2.2.(b), is used in order to acquire the spatial distribution of spectral sky radiance in 113 directions simultaneously. Instead of an entrance slit and a camera lens a bundle of 113 vertically aligned optical fibers is attached to the entrance of the imager. At the light receiving end of the bundle each fiber is embedded in a dome, pointing to a specific direction at the sky, thus collecting radiance from 113 directions simultaneously. A detailed description of the entrance optics design and the developments necessary in order to perform radiometric measurements is given in Section 3.2.

2.5 Allsky Camera System

In addition to the three spectroradiometers an allsky camera system has been used in order to capture hemispherical images of the sky during the measuring campaigns. This so called hemispherical sky imager (HSI) has been developed at the IMuK and is presented in detail in Tohsing et al. (2013). The HSI consists of a Canon PowerShot G10 compact camera with a resolution of 4416 x 3312 pixels, equipped with a 183° FOV fisheye objective and mounted in a weatherproof housing. The hemispheric part of the image has a diameter of 2150 pixels, resulting in 3.6 million pixels per allsky image. Since the Canon PowerShot G10 uses a Bayer color filter array in order to create color pictures (Bayer, 1976; Shortis et al., 2004), only 50% of the 3.6 million pixels are used for the green channel, 25% for the red channel and 25% for the blue channel, respectively. This results in a spatial sampling rate of 4 pixels per zenith angle in the worst possible case (red or blue channel at the image diagonal). Compared to the spectroradiometers used in this thesis the spatial resolution of the HSI is still approx. 8000 times higher (900,000 pixels in the red or blue channel compared to 113 scan points). Since the HSI provides at least a pixel each 0.24° zenith angle it is suitable for the quantification of uncertainties e.g., arising from different entrance optics FOVs of SCCD and MUDIS. For this task an algorithm capable of simulating different instrument characteristics based on allsky images has been developed in this thesis and is presented in Chapter 6.

2.6 Absolute Radiance Calibration

In order to measure absolute radiance values with SCCD and the NDACC instrument, a calibration procedure described in Pissulla et al. (2009) based on a diffuser plate has been applied. Pictures of the calibration setup are shown in Figure 2.3. The diffuser plate is illuminated uniformly by a calibrated lamp and positioned in the reference distance mentioned in the calibration protocol of the lamp. The radiance entrance optics is placed in a 45° angle relative to the reflectance plate without shading it (Figure 2.3(a)). When the end of the fiber bundle connected to the spectrometer is illuminated with a flash light, the entrance optics emits a light cone, shown in Figure 2.3(b). When the light cone is centered on the reflectance plate the FOV of the optics is adjusted properly. The diffuser plate is now illuminated by the calibration
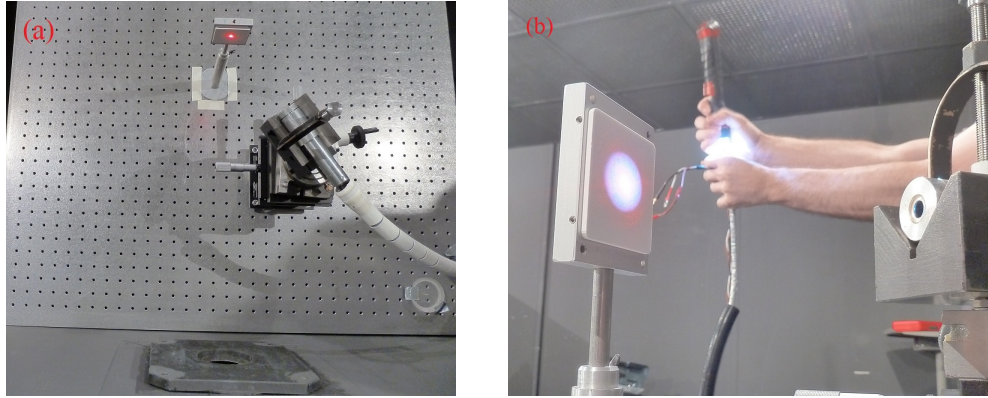
Figure 2.3: The pictures show the absolute radiance calibration described in Pissulla et al. (2009). On the left side the setup is shown from above. The diffuser plate is placed in line with the aperture in the lab wall and the calibration lamp on the other side. The entrance optics is positioned in a 45° angle to the plate. On the right picture the field of view (FOV) of the entrance optics is checked by illuminating the optical fiber bundle attached to the optics with a flashlight. Apparently the whole FOV of the entrance optics is illuminated by the radiance that will be emitted by the diffuser plate during the calibration process.

lamp. According to Pissulla et al. (2009) the spectral radiance L_λ emitted by the diffuser plate can be calculated by:

$$L_\lambda = \frac{R(0°, 45°, \lambda)}{\pi} E_\lambda \tag{2.2}$$

where $R(0°, 45°, \lambda)$ is the bidirectional reflectance factor and E_λ the spectral irradiance in $\mathrm{Wm^{-2}nm^{-1}}$ illuminating the diffuser plate. The spectral sensitivity $S_{Lab}(\lambda)$ of the instrument is determined in the calibration lab of the IMuK by:

$$S_{Lab}(\lambda) = \frac{X(\lambda)}{L_\lambda} \tag{2.3}$$

where $X(\lambda)$ is the signal in counts measured with the spectroradiometer at a certain wavelength λ and L_λ the spectral radiance in $\mathrm{Wm^{-2}nm^{-1}sr^{-1}}$, emitted by the reflectance plate. The radiance sensitivity of the instrument may change over time and due to movement of the spectroradiometer, therefore calibrations need to be performed regularly. It is not feasible to perform the reflection plate based calibration outside the lab, therefore a mobile lamp housing developed by Seckmeyer (1989) is used to perform stability checks of radiance spectroradiometers. By measuring the signal of a 100 W halogen lamp mounted inside the lamp housing the spectral sensitivity at the time t is adjusted by the following equation:

$$S_t(\lambda) = S_{Lab}(\lambda) \frac{Y_t(\lambda)}{Y_{Lab}(\lambda)}. \tag{2.4}$$

$Y_{Lab}(\lambda)$ is a lamp housing measurement performed directly after determining the sensitivity $S_{Lab}(\lambda)$ through the radiance calibration in the lab and $Y_t(\lambda)$ is a lamp housing measurement at the time t during a measurement campaign.

2.7 Determination of the Detection Threshold

The detection threshold (DT) is an important instrument parameter since it is mandatory to know to which extend a spectroradiometer is capable of performing measurements under low light conditions. For the determination of the detection threshold the noise equivalent radiance (NER) is a necessary input value and is defined as the ratio of the standard deviation of the dark current $\sigma_{DARK}(\lambda)$ to the radiance sensitivity $S(\lambda)$ of the instrument (Seckmeyer et al., 2010):

$$NER(\lambda) = \frac{\sigma_{DARK}(\lambda)}{S(\lambda)}. \tag{2.5}$$

The NER expresses the noise of a spectroradiometer in $\mathrm{Wm^{-2}nm^{-1}sr^{-1}}$. The standard deviation of the dark current is dependent on the integration time and the number of measurements averaged for a single acquisition.

The detection threshold $DT(\lambda)$ of the instrument in $\mathrm{Wm^{-2}nm^{-1}sr^{-1}}$ is defined after Seckmeyer et al. (2010) as follows:

$$DT(\lambda) = \Delta U_{DARK}(\lambda) + \Delta U_{STRAY}(\lambda) \tag{2.6}$$

where $\Delta U_{STRAY}(\lambda)$ is the uncertainty of the stray light correction and $\Delta U_{DARK}(\lambda)$ is the uncertainty of the dark current correction. $\Delta U_{DARK}(\lambda)$ includes the statistical noise expressed by the NER and possible systematic errors due to a dark current drift in the time between the dark current correction and the actual measurements of sky radiance. It can be assumed that the systematic error arising from dark current drifts is negligible small, since each measurement is corrected instantaneously for possible drifts based on optically dark pixels of the sensor array.

The determination of $\Delta U_{STRAY}(\lambda)$ is a complex task (Seckmeyer et al., 2010) and is not conducted in this work. Instead, a simple approach is chosen, where $DT(\lambda)$ is defined as $2 \times \mathrm{NER}$. This assumption is based on the fact that the stray light correction methods applied for SCCD and MUDIS includes an offset correction based on the dark region of the spectrum below 285 nm (see Section 3.1.4 and Section 3.2.8). The influence of $\Delta U_{STRAY}(\lambda)$ is therefore assumed to be small compared to the NER and therefore $2\,\mathrm{NER}$ are assumed to be a sufficient measure for DT in the UV region of the spectrum.

3 Instrument Development and Characterization

3.1 Sky Scanning CCD Array Spectroradiometer (SCCD)

In this section the characterization of the scanning CCD spectroradiometer (SCCD) introduced in Section 2.3 is presented. A brief overview over the specifications of the SCCD is given in Table 3.1. The instrument fulfills not all recommendations given by the Global Atmosphere Watch (GAW) programme of the World Meteorological Organization (WMO) in Seckmeyer et al. (2010). Especially the additional coverage of the visible range of the spectrum leads to cutbacks in the bandwidth and sampling interval of the instrument since a wider operational wavelength range has to be covered with the same amount of sensor pixels. The DT of $3\,\mathrm{mWm^{-2}nm^{-1}sr^{-1}}$ is higher than recommended and is a consequence of the short scan times chosen in order to perform as much sky radiance measurements as possible per day.

Specification	Quantity	WMO recommendations
Detector	2048 pixel CCD array	-
ADC	16 bit (65536 counts)	-
Spectral range	265–900 nm	280–400 nm
Sampling interval	0.22–0.39 nm	0.2 nm
Bandwidth	0.7–1.8 nm	1 nm
FOV	5°	5°
DT (310–400 nm)	<3 $\mathrm{mWm^{-2}nm^{-1}sr^{-1}}$	<1 $\mathrm{mWm^{-2}nm^{-1}sr^{-1}}$
Measurement time	2 s	<10 s

Table 3.1: Specifications of the SCCD instrument and the corresponding recommendations given by the GAW programme of the WMO (Seckmeyer et al., 2010).

3.1.1 Field of View Characterization

The SCCD is equipped with an entrance optics shown in Figure 2.3. The entrance optics is designed after an optics used by Wuttke (2005). It consists of a metal tube with integrated baffles, limiting the FOV of the optical fiber attached to the entrance optics. The FOV characterization of the optics has been performed according to Wuttke (2005): The entrance optics is mounted on a rotating table and turned by 0.5° steps in front of a tungsten halogen lamp. The region where the measured signal is higher than 0.5 times the maximum signal is defined as the FOV. The result of the FOV characterization is shown in Figure 3.1. The entrance optics limits the FOV of the fiber bundle to 5°. The wavelength dependency over the whole examined wavelength range of 300–900 nm was less than 0.1° and is therefore negligible.

3.1.2 Wavelength Alignment and Bandwidth

The corresponding wavelength of all 2048 SCCD sensor pixels is determined by a third order polynomial (Equation 3.1.2) which coefficients are initially provided by a factory calibration
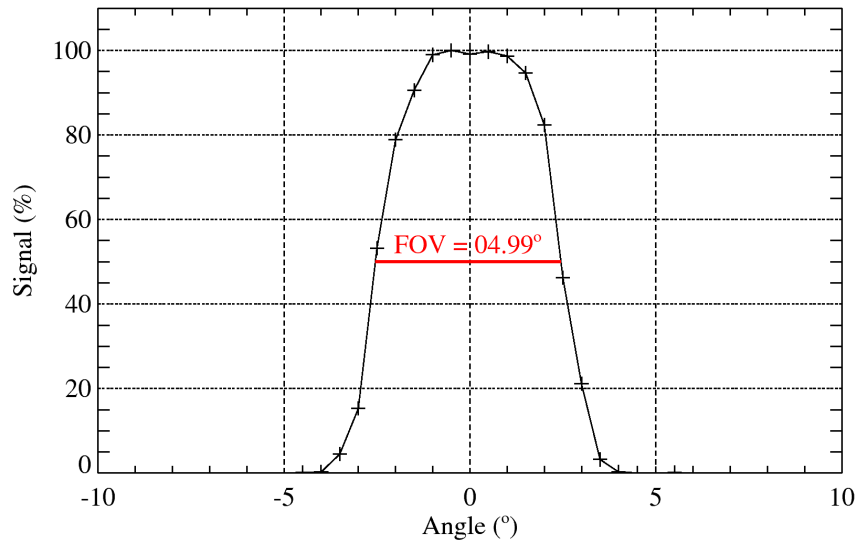
Figure 3.1: FOV of the SCCD entrance optics, acquired by rotating the entrance optics in front of a light source by steps of 0.5°.

of the spectrometer manufacturer, performed with spectral line lamps. Since the wavelength alignment of grating spectrometers is temperature dependent due to thermal expansion of the grating, the procedure has to be performed regularly. For the wavelength calibration of the SCCD the spectra of a mercury argon (HgAr) and a krypton (Kr) line lamp are measured. Twelve different emission lines of the spectral line lamps are selected and their well-known wavelength positions are used for a linear regression which provides the necessary variables for a third order polynomial (Sansonetti et al., 1996; Pissulla, 2006). The following third order polynomial is exemplary for the SCCD, calibrated at an ambient temperature of 20°C:

$$\lambda_i = 263.45 + 0.39381525 p_i + -4.0209719 \cdot 10^{-5} p_i^2 + 5.6358481 \cdot 10^{-11} p_i^3. \tag{3.1}$$

λ_i is the corresponding wavelength of pixel i, where p_i is a number between 0 and 2047. In addition to the wavelength alignment the spectral range and the sampling interval of the spectrometer can be determined from the polynomial. When inserting $p_0 = 0$ and $p_{2047} = 2047$ into the formula the spectral range is derived, ranging from 263.45 to 901.59 nm. The second term of the formula indicates that the sampling interval between pixel 0 and 1 is approx. 0.39. For higher pixel numbers the third term gains importance and since the coefficient is negative the sampling interval decreases to 0.23 between pixel 2046 and 2047.

Measurements of the spectral line lamps can also be used to determine the bandwidth of the instrument by calculating the full width at half maximum of the emission lines (Seckmeyer et al., 2010). In Figure 3.2 the bandwidth calculated from each of the twelve emission lines used for the wavelength calibration is shown. The spectrometer shows a wavelength dependent bandwidth, rising from 0.8 nm at 300 nm up to 1.8 nm at 550 nm and falling to 0.7 nm at 820 nm.

3.1.3 Non-Linearity

The desirable response of a spectrometer sensor is linear: By doubling the input signal the counts measured by the spectrometer should also double. Unfortunately CCD sensors are
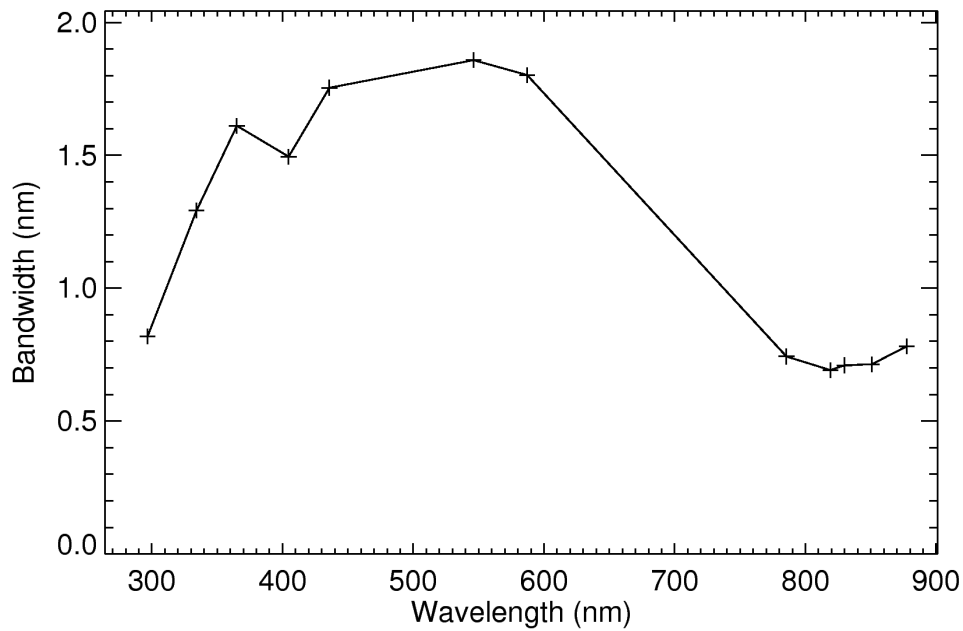
Figure 3.2: Bandwidth of the SCCD acquired from emission lines of HgAr and Kr line lamps. The bandwidth is wavelength dependent: In the UV and NIR part of the spectrum rather small bandwidths of 0.7 nm are observed. The highest bandwidth of 1.8 nm occurs around 550 nm.
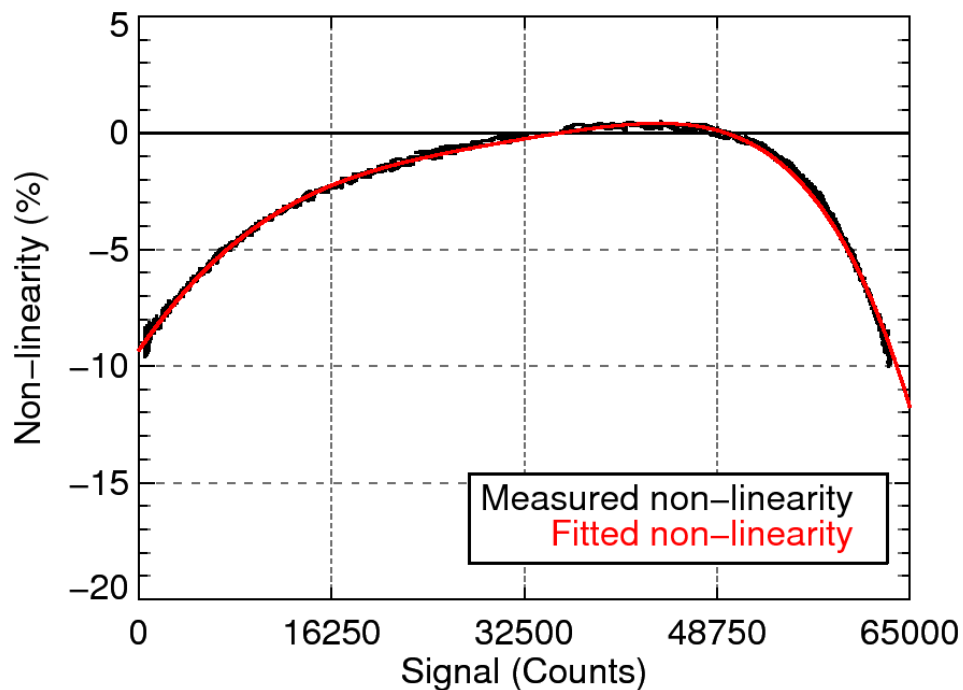
Figure 3.3: Non-linearity of the SCCD sensor in percent.

not perfectly linear and thus a non-linearity characterization and correction is needed. The non-linearity of the SCCD is determined by illuminating the entrance optics with a stable halogen lamp and varying the integration time of the instrument from short to long integration times. This way a set of measurements is generated which covers the whole dynamic range of the sensor. The detector non-linearity is derived by first defining the counts/s at half the dynamic range as a reference point. By multiplying the integration times used for the set of measurements with the reference counts/s the theoretical count values are calculated. The ratio of measured and theoretical count values is now a measure for non-linearity of the sensor. The non-linearity of the SCCD is displayed in Figure 3.3. For low and high count values a non-linearity of up to 10% is observed. By fitting the non-linearity with a fifth order polynomial fit a non-linearity factor (NLF) for each count value C can be calculated:

$$\text{NLF} = 0.907 \cdot C + 7.37 \cdot 10^{-6}C - 2.23 \cdot 10^{-10}C^2 + 1.65 \cdot 10^{-15}C^3 + 5.45 \cdot 10^{-20}C^4 - 8.52 \cdot 10^{-25}C^5.$$
(3.2)

The linearity correction of measurements can now be performed by dividing a measured count value C with its corresponding NLF.

However, the downside of this method is that changing the integration time is also a non-linear process. A characterization without deviating the integration time should therefore be used in the future, e.g., by varying the input signal by a variation of the distance between entrance optics and light source.

3.1.4 Stray Light Correction

Stray light is a major problem for CCD spectrometers based on diffraction grating monochromators. "Monochromators are optical devices designed to transmit radiation of a narrow band of wavelengths. In practice it will also transmit a small radiant flux at wavelengths outside this narrow band. This is commonly referred to as stray light" (Sharpe and Irish, 1978). For example, when measuring monochromatic green laser light (532 nm), the spectrometer also detects a weak signal far outside the nominal bandwidth, e.g., at 300 nm. This stray light is caused by light, scattered inside the instrument mainly by imperfections of the diffraction grating (Sharpe and Irish, 1978), overlap of diffraction orders, but also by mirrors, baffles screw heads and other surfaces. The instrument stray light is several orders of magnitude smaller than the actually measured wavelengths. However, stray light becomes a severe problem when measuring broadband sources like sky radiance, where parts of the measured spectrum also differ from each another by several orders of magnitude. An example on how much stray light occurs for a typical sky radiance measurement in the UVB part of the spectrum is given in Figure 3.4. At 305 nm an uncorrected measurement (black line) shows a 45% higher signal (blue line) compared to the same measurement with an applied stray light correction (red line). Nearly 100% of the detected signal at 300 nm originates from stray light, a proper correction method is therefore crucial.

In order to improve the instrument performance of the SCCD a stray light correction method after Kreuter and Blumthaler (2009) is applied: The so called stray light distribution function (SDF) of the instrument has to be derived from measurements of monochromatic light, emitted by a laser. In addition, measurements with a 360 nm cutoff filter have to be performed in order to correct lamp measurements, since the correction method introduces an offset factor to address stray light originating from outside the spectral range of the instrument. A second offset factor for sky radiance measurements is needed, since the spectral distribution of sky radiance differs strongly from lamp measurements. Ozone absorption acts as a natural cutoff filter,
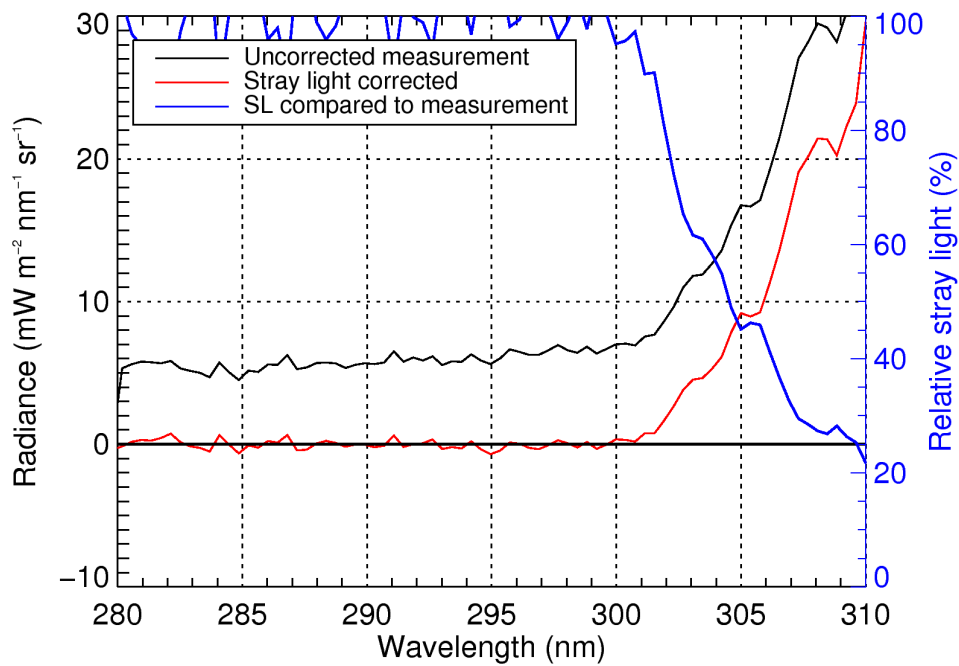
Figure 3.4: Stray light (SL) corrected sky radiance measured with the SCCD. At 305 nm approx. 45% of the measured uncorrected signal consists of stray light (blue line). By applying the stray light correction method the measured signal is improved significantly.
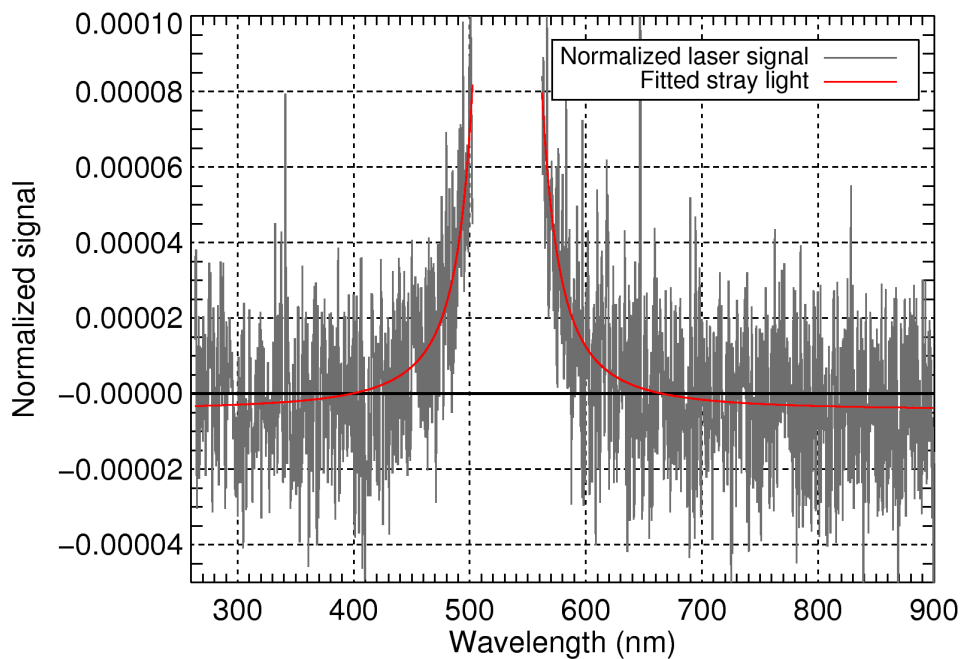
Figure 3.5: Straylight distribution function of the SCCD spectrometer, acquired by measuring the light emitted by a green laser at 534 nm (green line). The black line is a power function fit to the measured stray light according to Kreuter and Blumthaler (2009).

therefore, the second offset factor can be derived from the wavelength region below 285 nm of each sky radiance measurement. The SDF and the offset factors are used to determine a stray light correction (SLC) matrix which is later multiplied with the measured spectrum in order to derive a stray light corrected spectrum.

The SDF, derived from green laser measurements, is shown in Figure 3.5. Despite a total measurement time of 60 min the SDF derived from the laser signal is still noisy. Since the combined uncertainties of dark current and offset correction extend the stray light signal, even negative values are observed. Nevertheless, it is still possible to fit the measured SDF with a power function in order to determine its slope (Kreuter and Blumthaler, 2009). By the determination of the offset factor based on a lamp measurement with a cutoff filter the offset uncertainty is compensated. In this thesis, a 295 nm cutoff filter is used instead of the 360 nm filter proposed by Kreuter and Blumthaler (2009). This ensures that offset uncertainties originating from the 295 to 360 nm wavelength region are also addressed by the determined offset factor, since calculations setting measured signals in this region to 0 show that about 20% of the stray light at 300 nm originates from the 295 to 360 nm wavelength region. The filter measurement performed in order to derive the SDF offset factor is shown in Figure 3.6(a). In addition to the 295 nm cutoff filter a 400 nm filter is used in order to check the performance of the stray light correction method for a wider wavelength range. By choosing a SDF offset factor of $3.4 \cdot 10^{-6}$, a good stray light correction is achieved, reducing the amount of stray light in the UV by at least one order of magnitude (Figure 3.6(b)).

Stray light at longer wavelengths due to an overlapping of diffraction orders is not accounted by the correction method. However, the concave grating installed in the spectrometer provides an efficient reduction of second order efficiency.
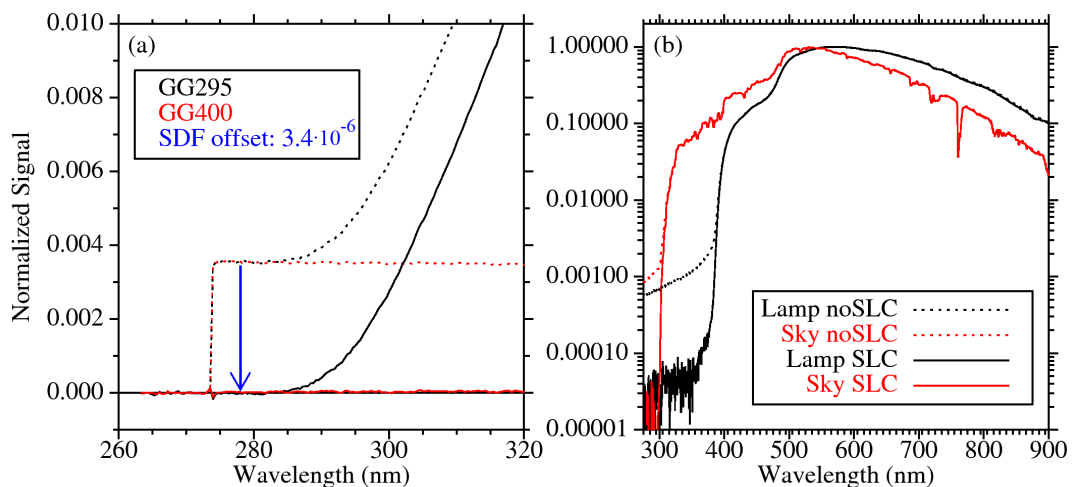
Figure 3.6: SCCD measurements (a) of a halogen quartz lamp through a 295 nm (black lines) and a 400 nm (red lines) cutoff filter. Dashed lines show both measurements after a stray light correction based on the determined SDF without any offset factor applied. Solid lines show measurements after stray light correction with a suitable SDF offset factor of $3.4 \cdot 10^{-6}$. In (b) measured spectra of a calibration lamp (black lines) and the sky (red lines) are shown. A 400 nm filter is applied for the lamp measurement and no filter was used for the sky measurement since ozone absorption provides a natural cutoff filter. Dotted lines show the measurements without stray light correction compared to the same measurements with an applied stray light correction. The stray light is reduced by approximately one order of magnitude.

3.1.5 Sensitivity and Noise Equivalent Radiance

The radiance sensitivity of the SCCD is determined by performing the absolute radiance calibration described in Section 2.6. The highest sensitivity of the SCCD is observed at 550 nm (Figure 3.7(a)). The sensitivity in the UV is about one-third of its maximum value and for wavelengths higher than 675 nm the sensitivity is even lower than in the UV, decreasing rapidly with longer wavelengths.

In this thesis SCCD sky radiance measurements are performed with an integration time of 50 ms and 40 averages, resulting in a measurement time of about 2 s per radiance scan point. These settings yield an NER shown in Figure 3.7. In the UV the NER is about 1.0 to 1.5 mWm^{-2}nm^{-1}sr^{-1}. The minimum NER of the SCCD of 0.3 mWm^{-2}nm^{-1}sr^{-1} is at 550 nm and rises with longer wavelengths up to 6 mWm^{-2}nm^{-1}sr^{-1} at 900 nm.
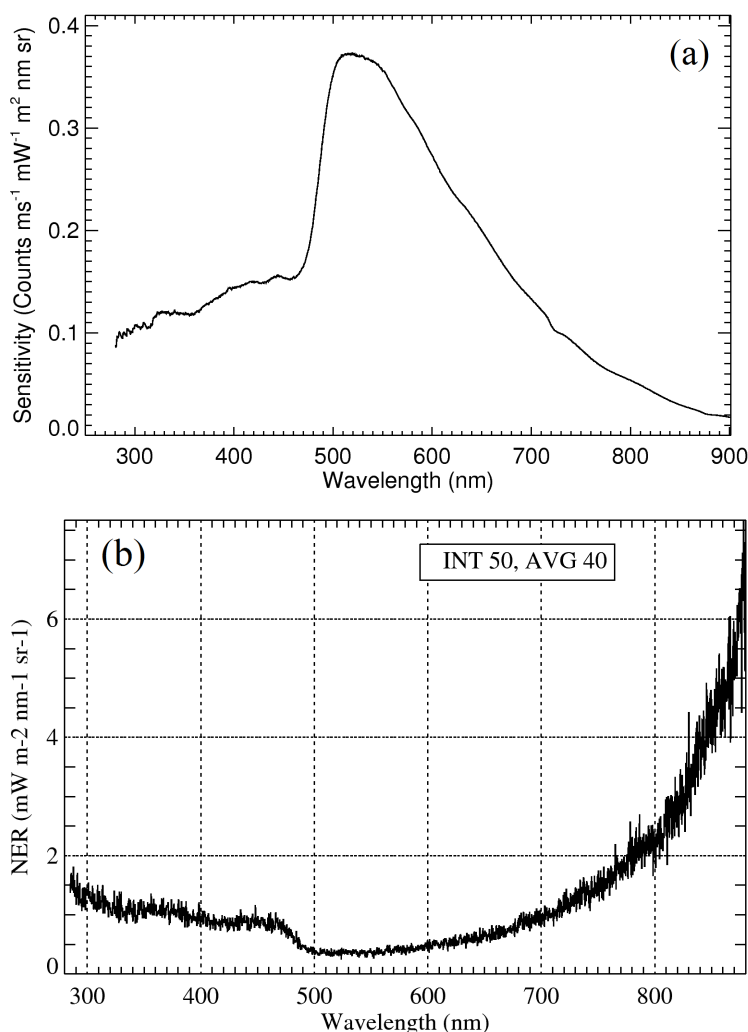
Figure 3.7: Plot (a) shows the sensitivity of the SCCD acquired through the absolute calibration procedure described in Section 2.6. Plot (b) shows the NER of the SCCD, derived from dark current measurements performed with an integration time of 50 ms and 40 averages.

3.2 Multidirectional Spectroradiometer (MUDIS)
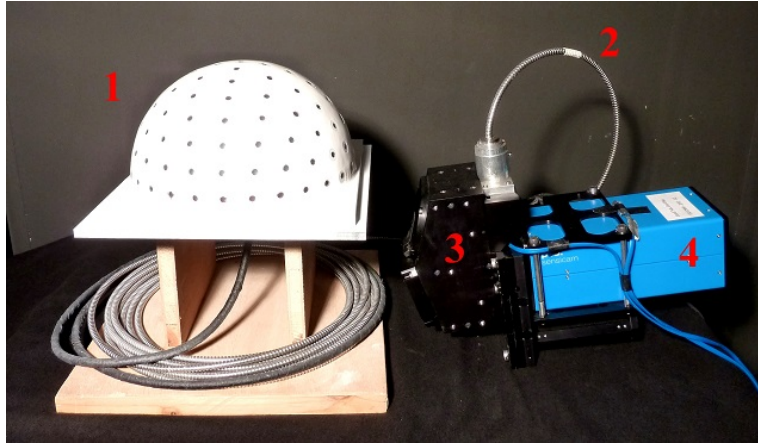
Figure 3.8: Main components of MUDIS: The weatherproof entrance optics dome (1) is connected via an optical fiber bundle (2) with the an Offner imaging spectrometer (3). A UV-sensitive CCD camera (4) is capturing the image provided by the imaging spectrometer.

In this chapter the development and characterization of MUDIS is described. The developed instrument is a snapshot spectral imager based on a fiber image slicing technique as described in 2.4. The main components of MUDIS are shown in Figure 3.8. Attached to the entrance of the imager is a bundle of optical fibers consisting of 135 single fibers vertically aligned to a slit. The receiving ends of the fibers are embedded in a dome in which 113 of the 135 fibers are evenly distributed in zenith and azimuth directions. A brief overview over the specifications of MUDIS is given in Table 3.2. MUDIS is capable of performing measurements in less than two seconds with a DT $< 1\,\mathrm{mWm}^{-2}\mathrm{nm}^{-1}\mathrm{sr}^{-1}$, fulfilling two important recommendations for sky radiance measurements, given by the GAW programme of the WMO in Seckmeyer et al. (2010). Analogous to SCCD the additional coverage of the visible range of the spectrum leads to cutbacks in bandwidth and sampling interval. The recommended FOV is also not fulfilled, this issue is examined with special emphasis in Section 6.1.

Technical Detail	Quantity	WMO recommendations
Detector	1024×1002 pixel camera	-
ADC	12 bit (4096 counts)	-
Spectral range	250–680 nm	280–400 nm
Sampling interval	0.44 nm	0.2 nm
Bandwidth	1.5–2.5 nm	1 nm
FOV	9°–17°	5°
DT (310–400 nm)	$< 1\,\mathrm{mWm}^{-2}\mathrm{nm}^{-1}\mathrm{sr}^{-1}$	$< 1\,\mathrm{mWm}^{-2}\mathrm{nm}^{-1}\mathrm{sr}^{-1}$
Measurement time	2 s	< 10 s

Table 3.2: Specifications of the SCCD instrument and the corresponding recommendations given by the GAW programme of the WMO (Seckmeyer et al., 2010).

3.2.1 Entrance Optics Development

The entrance optics dome displayed in Figure 3.8 is a novel design, developed at the IMuK and partially constructed by an external company (CeramOptec GmbH, Bonn, Germany), since
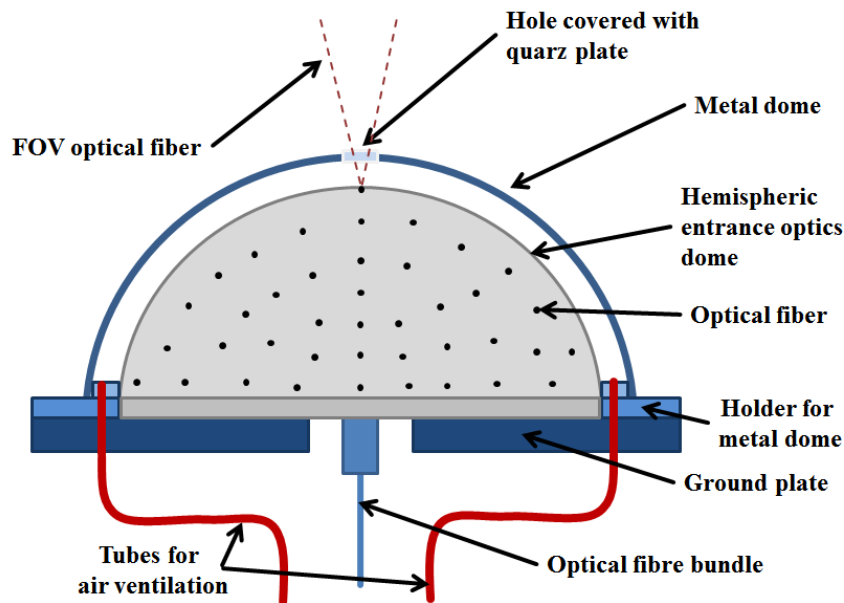
Figure 3.9: Sketch of the MUDIS entrance optics dome.

no comparable entrance optics is currently commercially available. In Figure 3.9 a sketch of the entrance optics dome is presented. The main part of the optics is a hollow plastic dome which is used to align the fiber ends of the fiber bundle to predefined directions of the sky. Therefore small holes are drilled through the wall of the plastic dome. The fiber ends are polished and assembled with metal ferrules and glued inside the holes of the dome. The plastic dome is encased by a larger metal dome in order to provide a weather protection. At each fiber position a hole is drilled inside the metal dome, which is in turn covered by a quartz glass plate. All plates are embedded in filling compound and a final layer of white paint covering the compound seals the dome. The space between inner and outer dome is ventilated with dry air in order to prevent condensation on the quartz glass plates.

Development of a Suitable Measurement Pattern

In contrast to scanning spectroradiometers the measurement directions of MUDIS cannot be variably adjusted after the construction of the entrance optics dome, therefore the measurement pattern has to be designed with great care. A suitable pattern has to fulfill several requirements:

1. **Representative distribution.** In order to determine the sky radiance of the whole hemisphere the measurement pattern has to be representative for this area. It therefore should cover the hemisphere in a homogeneous grid which is increasingly difficult with decreasing numbers of measurement points.

2. **Almucantar symmetry (points on circles parallel to the horizon).** A hemisphere has a natural boundary set by the horizon. Thus, it is feasible to distribute the available measuring points on almucantars with different zenith angles.

3. **Zenith coverage.** The zenith point is a common reference point for instrument comparisons and should be covered by the distribution pattern.

$$1+4+8+12 = 25 \qquad 1+6+12+18 = 37$$
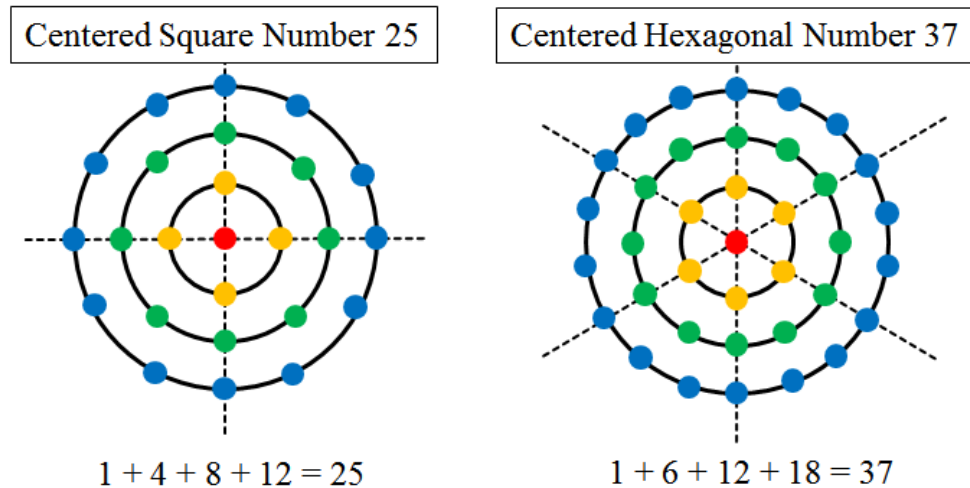
Figure 3.10: Centered polygonal numbers: A polygonal number with P=4 points in the first layer is called centered square number and a number with P=6 points in the first layer is called centered hexagonal number.

4. **Geometrically simple.** An entrance optic dome with a geometrically simple point distribution is easier to construct than one with a random point distribution. A simple distribution also makes it easier to manually orient points during FOV characterization processes.

5. **Sufficient number of fibers.** The distribution pattern is limited by the number of fibers available. From the 135 fibers connected to the spectrometer only 128 undamaged fibers were available at the entrance optics end of the bundle after delivery of the fiber bundle.

In order to fulfill all requirements a pattern has been developed based on the so called centered polygonal numbers. The geometrical expression of such a number is a centered point surrounded by a layer of P points, which in turn is surrounded by the next layer of $P + P$ points (Figure 3.10). Two different layer designs based on a centered square number ($P = 4$) and a centered hexagonal number ($P = 6$) have been considered. Since each additional layer consists of a predefined amount of points only certain polygonal numbers are possible. Centered hexagonal numbers can be calculated by the term $3n^2 + 3n + 1$ where n is the number of layers around the center. Possible point patterns based on hexagonal numbers may therefore consist of 1, 7, 19, 37, 61, 91, 127, 169,... points. Centered square numbers are calculated by the term $n^2 + (n+1)^2$, so possible patterns consist of 1, 5, 13, 25, 41, 61, 85, 113, 145,... points. Since the number of points available is limited to 128 the numbers 113 and 127 have been considered as possible patterns, displayed in Figure 3.11. The pattern with 113 points is chosen for the MUDIS entrance optics dome, since some fibers might break during the entrance optics assembling process and several spare fibers are therefore feasible. In addition, the square pattern provides a more even distribution of points in zenith and azimuth direction since it consists of one more layer (8) compared to the second pattern (7).

3.2.2 Development of an Entrance Optics Ventilation

During the first comparison campaign conducted in October 2012, condensation occurred on the inside of the quartz glass plates of the MUDIS entrance optics (Figure 3.12). In order to
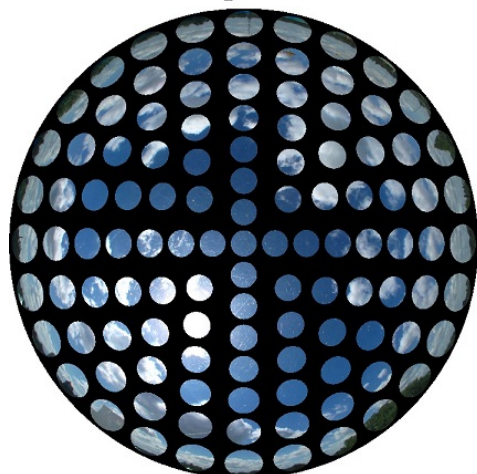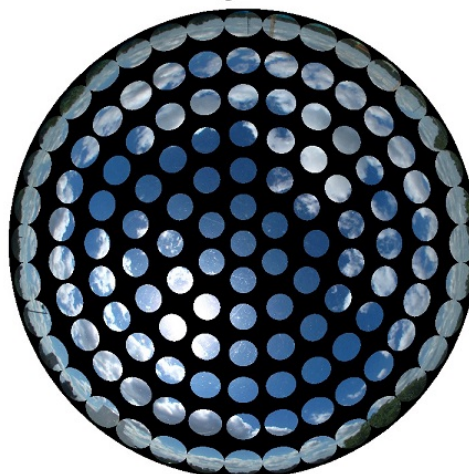
Figure 3.11: The left pattern is based on the centered square number 113 and the right one based on the centered hexagonal number 127. The points are displayed with a FOV of 10°. The left pattern has been chosen for the MUDIS entrance optics dome since it consists of a suitable amount of points and provides a more regular distribution in zenith and azimuth direction than the right pattern.

prevent further condensation, a system based on a diaphragm pump has been developed, which ventilates the space between the inner and outer dome with dry air. Those pumps are commonly used in aquaristics because the pumped air is oil free and no additional filter devices are needed. During the second comparison campaign conducted in July 2013 the pump system was placed in the climate box of the NDACC instrument. The air pumped into the entrance optics dome had a temperature of 20°C and a relative humidity of approx. 30% and effectively prevented any condensation.

Figure 3.12: MUDIS entrance optics with condensation on the inside of the quartz glass plates.

Figure 3.13: MUDIS shading unit, consisting of a stepping motor and a black shadow band.

3.2.3 Development of an Entrance Optics Shading Unit

A further result of the first comparison campaign is the severe influence of direct sunlight on the MUDIS measurements. When fibers are illuminated with direct sunlight, up to 49 of the 113 measuring directions are rendered unusable due to severe stray light effects (Section 3.2.8 and 4.2.3). As a result a shading unit has been developed as part of a master thesis (Niedzwiedz, 2013). The shading unit is shown in Figure 3.13 and consists of a black painted metal shadow band which is rotated by a stepping motor in order to block direct sunlight in the course of a day. The influence of the shadow band on the measurements is discussed in Section 5.2.1.

3.2.4 Fiber-Sensor Assignment

The fibers of MUDIS were not sorted in any kind during the assembling process of the entrance optics dome, thus the fibers are reaching the spectrometer in a random order. The assignment between a fiber of the entrance optics dome and the corresponding sensor area has been achieved by illuminating each of the 113 fibers subsequently with a flashlight. The signal corresponding to a fiber is typically 7–8 rows broad with a peak in the middle of that region. The signal by those three rows providing the strongest signal is binned together and is referred to as a MUDIS channel. Figure 3.14 shows the assignment pattern derived by this characterization.
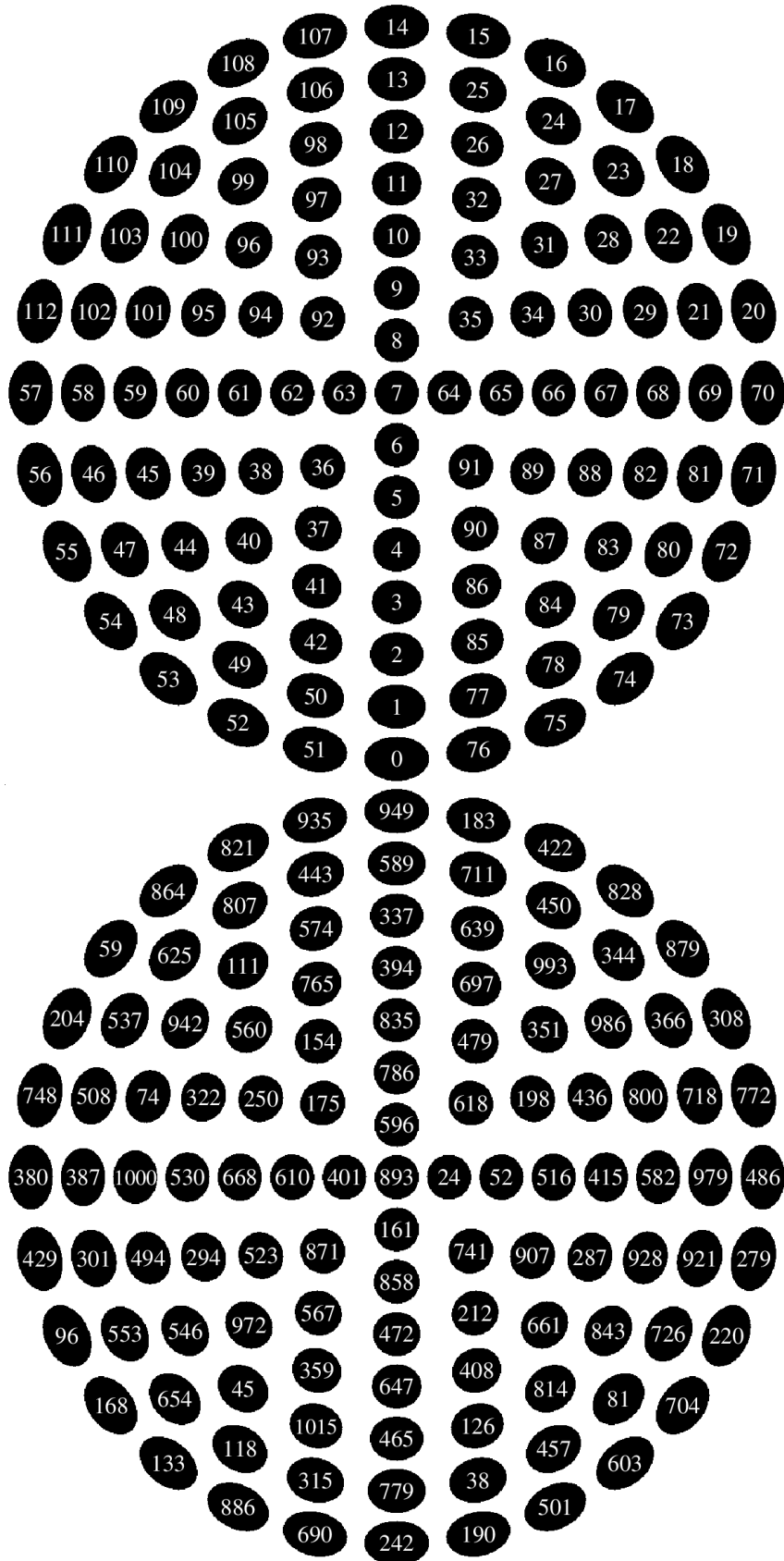
Figure 3.14: The upper plot shows the MUDIS pattern, numerated in the same way like the scan process of the SCCD pattern. The lower plot shows the number of the strongest corresponding sensor row to each MUDIS entrance fiber.

3.2.5 Field of View Characterization

The characterization of the FOV and the viewing direction of several individual channels of the MUDIS entrance optics dome is performed according to Figure 3.15, which demonstrates the setup for the zenith channel. The dome is mounted on a rotating table analogous to the characterization of the SCCD entrance optics in Section 3.1.1. The channel is positioned in the rotatory axis of the table. A halogen lamp is placed in a distance of at least 50 cm from the entrance optics dome. The lamp is aligned on an optical line with the fiber by using a cross line laser. In addition, two mirrors are attached to the ground plate of MUDIS, reflecting a part of the cross laser signal back to its source. This enables an accurate adjustment of the entrance optics relative to the cross line laser, the intended viewing direction of the channel is now aligned to the center of the cross line. The angular response of the channel is then characterized by performing sequential MUDIS measurements while rotating the entrance dome from $\alpha = -15°$ to $15°$ in steps of $0.5°$.
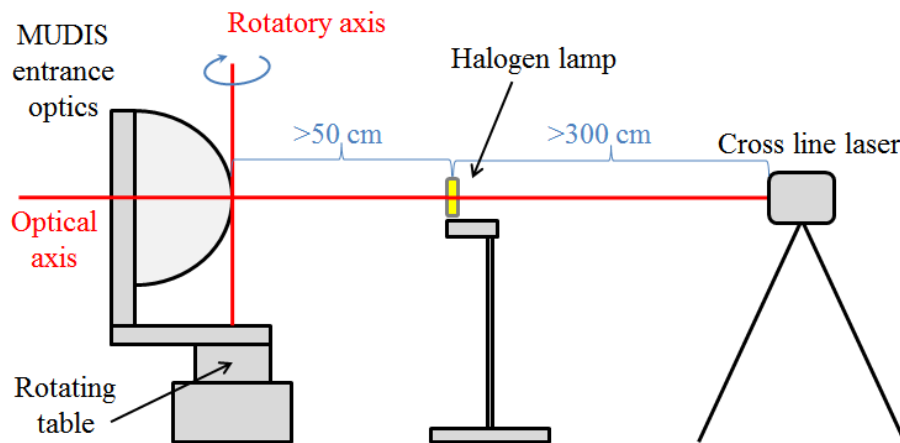
Figure 3.15: Setup for the FOV characterization of the zenith point of the MUDIS entrance optics. The lamp is aligned with the characterized MUDIS fiber by a cross line laser.

Unfortunately, the fibers are not perfectly orientated compared to their intended viewing angle, thus unintended tilts are to be expected. A secondary setup, shown in Figure 3.16, illustrates the problem. A translucent screen is placed in between the MUDIS zenith channel and the cross line laser. When illuminating the end of the fiber bundle normally attached to the imager, the zenith fiber emits laser light according to its acceptance angle at the wavelength of the laser light. The translucent screen now shows the signal of both cross laser and light emitted by zenith fiber. On the right side of Figure 3.16 the FOV of the zenith channel has been visualized for 632.8 nm (red laser light) with this method. The projection image of its FOV is tilted by a few degrees on the horizontal axis (eastwards), but shows no significant tilt on the vertical axis. A tilt on the vertical axis would result in a significantly smaller FOV derived by the FOV characterization, since the measurement would be performed tangential to the FOV projection. A horizontal tilt is not critical for the FOV characterization, since the measurement is performed on the same axis and only the zero point of the axis moves. Vertical tilts were corrected by adjusting the mounting of the entrance optics dome with the help of the projection setup before conducting the FOV measurements. Horizontal tilts are not adjusted,
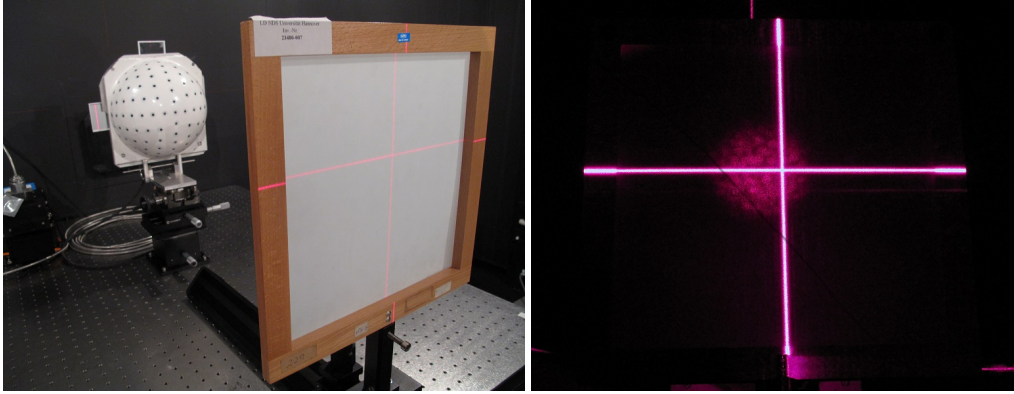
Figure 3.16: Setup for the FOV characterization of the MUDIS entrance optics dome. The upper picture shows a translucent screen which is standing between the entrance optics dome and a cross laser. The lower picture shows the translucent screen in the dark, illuminated by the cross laser on its front side and from laser light emitted by a fiber of the entrance optics dome on the back side.

but characterized during the measurement process. The horizontal angular tilt $\beta(\lambda)$ of the channels is therefore derived by calculating the center of gravity of the wavelength dependent angular response $Z(\alpha, \lambda)$:

$$\beta(\lambda) = \frac{\int_{-15}^{15} \alpha\, Z(\alpha, \lambda)\, d\alpha}{\int_{-15}^{15} Z(\alpha, \lambda)\, d\alpha}. \tag{3.3}$$

The FOV is derived by determining the full width at half maximum (FWHM) of the angular response. In Figure 3.17 the results of the FOV characterization of point 7 (zenith), 8, 9 and 63 of the MUDIS entrance optics dome (Figure 3.14) are shown. The FWHM of the zenith FOV varies between $10°$ at longer wavelengths and $19°$ at shorter wavelengths. The FOV of point 8 varies between $7°$ and $18°$ and for point 9 between $8°$ and $16°$. MUDIS channel 7 shows an angular tilt of about $1.5°$ to $2.5°$ eastwards. Channel 8 shows an angular tilt of about $-3.5°$ to $-2.5°$ westwards. The tilts of channel 9 and 63 is less than $1°$ and show a smaller wavelength dependence of less than $0.5°$.

An explanation for the wavelength dependent variation of the FOV has not been found yet. The observed wavelength dependence has also been reproduced by a FOV characterization where the MUDIS fiber bundle was coupled to the double monochromator-based spectroradiometer, introduced in Section 2.2. This excludes the possibility that an optical interaction of the MUDIS spectrometer with the fiber bundle is causing the wavelength dependence. The result of a second experiment, shown in Figure 3.18, supports the assumption that the wavelength dependence is a fiber characteristic. For this experiment the MUDIS entrance dome has been placed outside during overcast sky, this way each fiber was illuminated by sky radiance originating from clouds. A photo from the end of the fiber bundle was taken at a distance of $2\,cm$, shown in Figure 3.18. The camera was aligned directly over the left end of the line of fibers, the light guided through these fibers appear white. On the opposite side of the line the fibers appear blue, since the camera looks at them with a diagonal angle over $10°$. This is consistent with the measured FOV wavelength dependence, a blue shift in color should be observable from oblique viewing angles, since a lower proportion of light with longer wavelengths is emitted by the fiber at these angles, according to the FOV characterization.
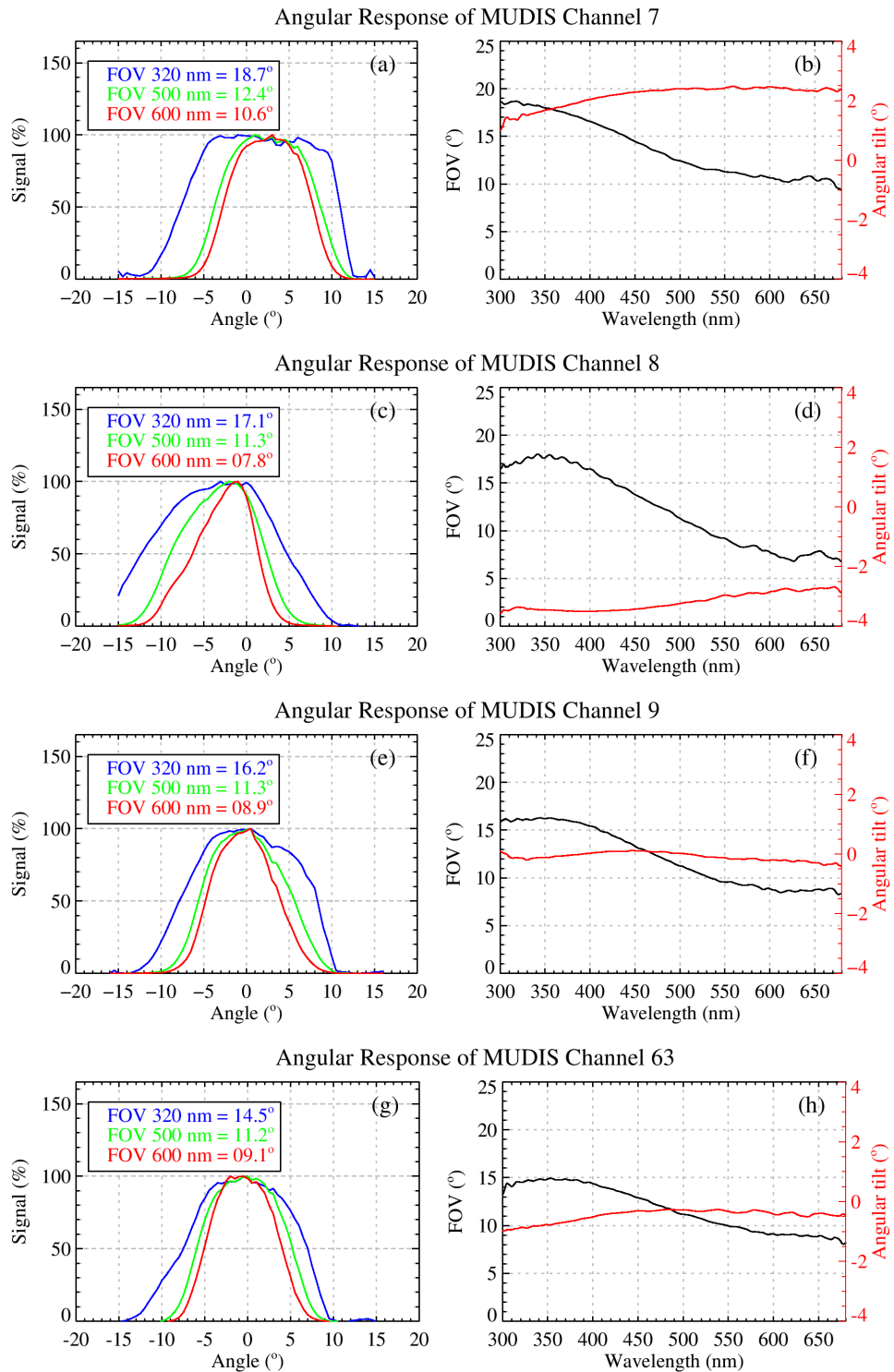
Figure 3.17: FOV characterization of MUDIS channel 7, 8, 9 and 63. Plot (a), (c), (e) and (g) show the angular response at three exemplary wavelengths of the channels, respectively. Plot (b), (d), (f), (g) show the wavelength dependence of the angular response and the angular tilt.
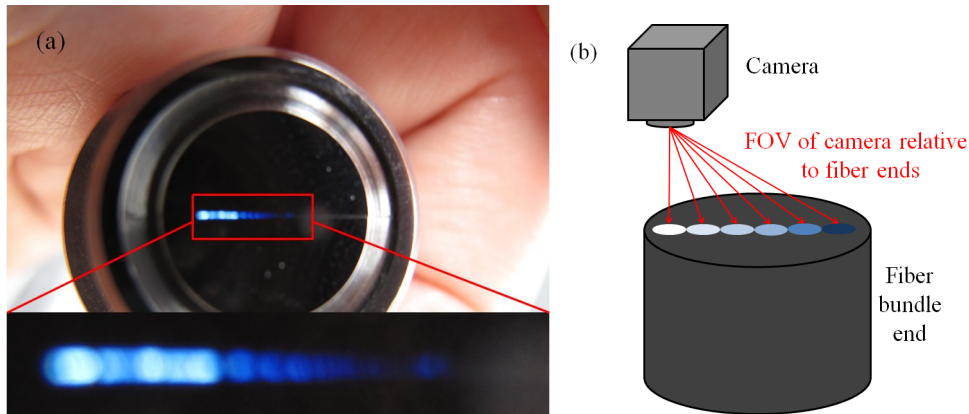
Figure 3.18: Figure (a) shows the end of the MUDIS fiber bundle photographed in a distance of approx. 2 cm. The entrance dome was placed outside during overcast conditions and thus receiving sky radiance from clouds only. The geometry of fiber and camera is shown in (b). The fibers directly below the camera are perceived white, while fibers viewed at a diagonal angle are perceived blue.

3.2.6 Non-Linearity

The MUDIS spectrometer is characterized and corrected for non-linearity with the same method applied to the SCCD spectrometer as shown in Section 3.1.3. Figure 3.19 shows the derived non-linearity. The non-linearity of MUDIS is smaller ($< 5\%$) compared to the non-linearity of SCCD ($< 10\%$) shown in Figure 3.3.
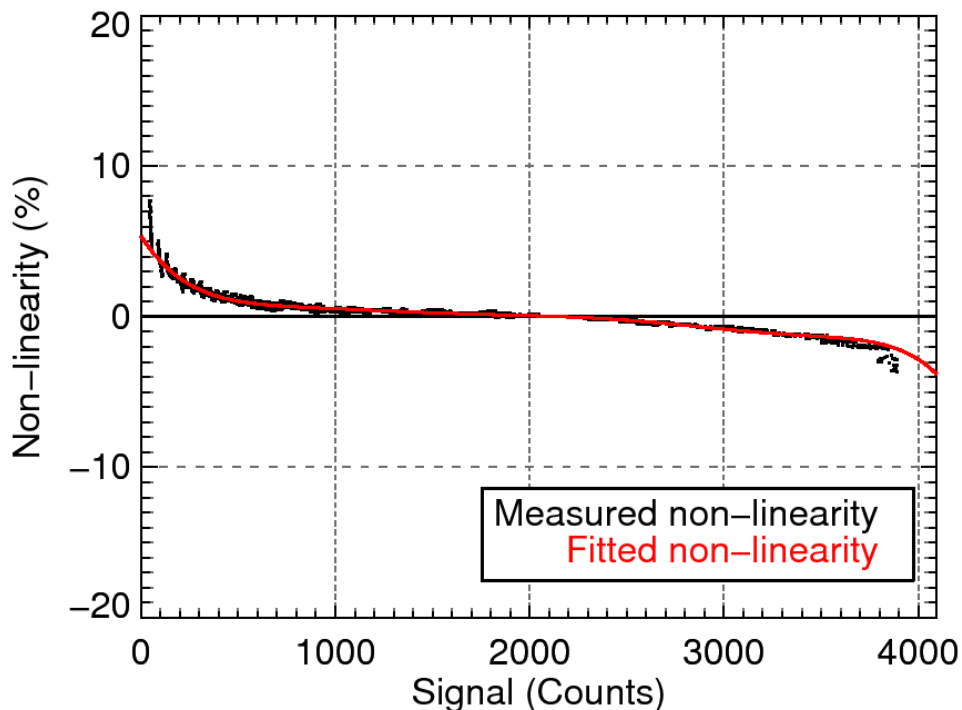
Figure 3.19: Non-linearity of the MUDIS spectrometer.

3.2.7 Wavelength Alignment and Bandwidth

The wavelength alignment of the spectrometer used in the MUDIS instrument is derived similar to the method described for the SCCD in Section 3.1.2. Illuminating each fiber of the MUDIS entrance optics dome sequentially with an HgAr line lamp provides a set of 113 wavelength calibration measurements. Those measurements are used to derive a second order polynomial fit for each fiber channel, shown in Figure 3.20. The spectral range is between approx. 250 and 680 nm and the sampling interval is approx. 0.44 nm for all MUDIS channels.

Since the wavelength calibration is performed in the lab and the fiber bundle has to be unplugged for the transportation of MUDIS, the wavelength calibration has to be checked again after the assembly of the instrument at the actual measuring site. Therefore, a correction method based on the 393.368 nm Ca^+ Fraunhofer line has been applied (Figure 3.21(a,b)). The figure shows that the wavelength calibration of the MUDIS channels deviates from the lab calibration by approx. 1.2 nm. Based on the position of the Ca^+ line at 393.368 nm individual shift factors for each MUDIS channel are calculated and applied to the wavelength alignment of each channel. Measurements corrected by the additional shift factor are shown in Figure 3.21(c,d). The wavelength alignment could be improved sufficiently by the additional correction method.

In Figure 3.22 the bandwidth of all MUDIS channels are plotted for the six emission lines that are used for the wavelength alignment. Most channels are in a bandwidth range of 1.5–2.5 nm.
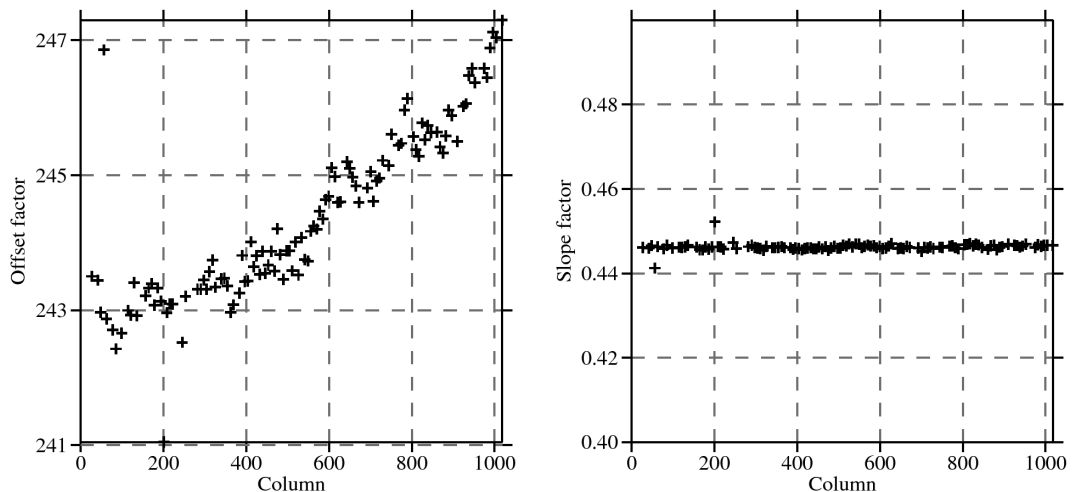
Figure 3.20: The figure shows the 113 offset and slope variables of the second order polynomials for the wavelength alignment of each MUDIS channel.

3.2.8 Stray Light

Comparable to the SCCD, stray light is also a concern for MUDIS. The reasons are basically the same as for SCCD, described in Section 3.1.4. However, a major exception leading to severe problems is an additional two-dimensional stray light component in case of MUDIS. When a fiber of MUDIS is illuminated with a monochromatic light source (Figure 3.23(a)), a stray light component near the illuminated line is observed (blue arrows) as well as a spatial stray light component (red arrows), affecting whole areas of the sensor. When illuminating a fiber with a broadband light source (Figure 3.23(b)) the spatial stray light component leads to blurred areas of stray light (marked with red circles), affecting measurements of adjacent sensor rows. The spatial stray light component is most severe when one or more fibers are illuminated by direct sunlight. Since direct sunlight is several orders of magnitude brighter than blue sky
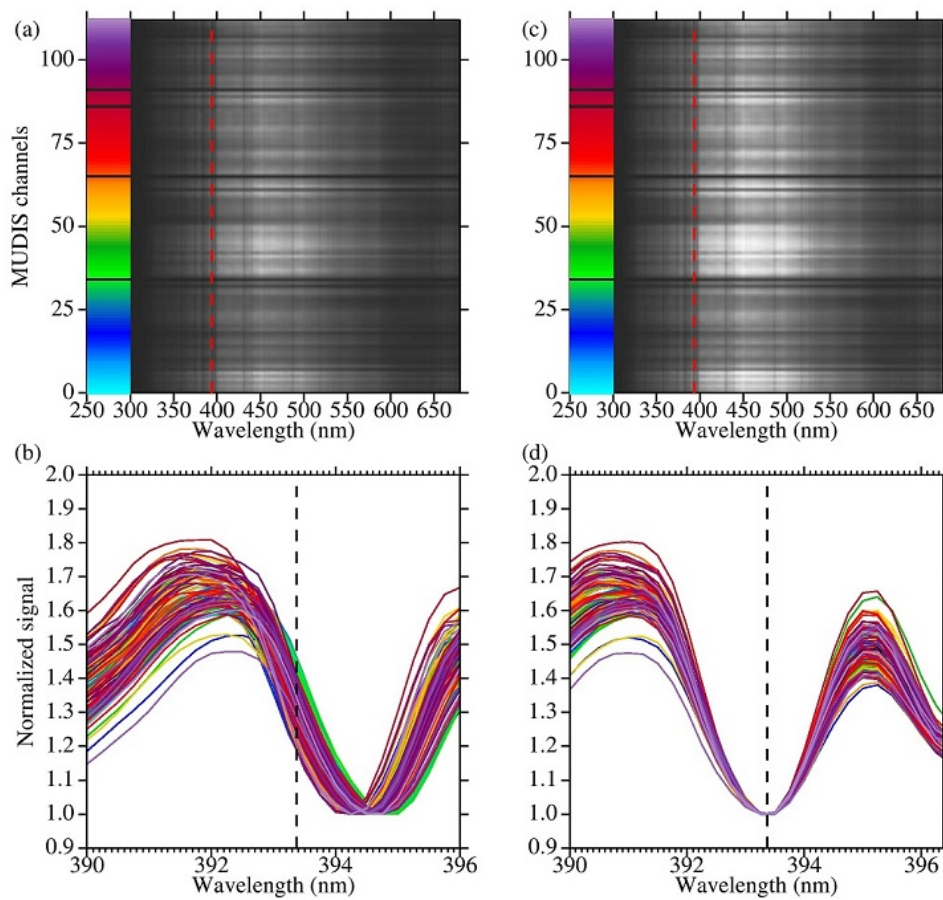
Figure 3.21: Signal of 113 MUDIS channels (a) after the line lamp calibration. Each MUDIS channel has an individual color; gaps are due to broken fibers. In (b) the normalized signals of these channels are shown near the 393.368 nm Ca^+ Fraunhofer line. In plot (c) and (d) an additional correction based on the Fraunhofer line was performed.
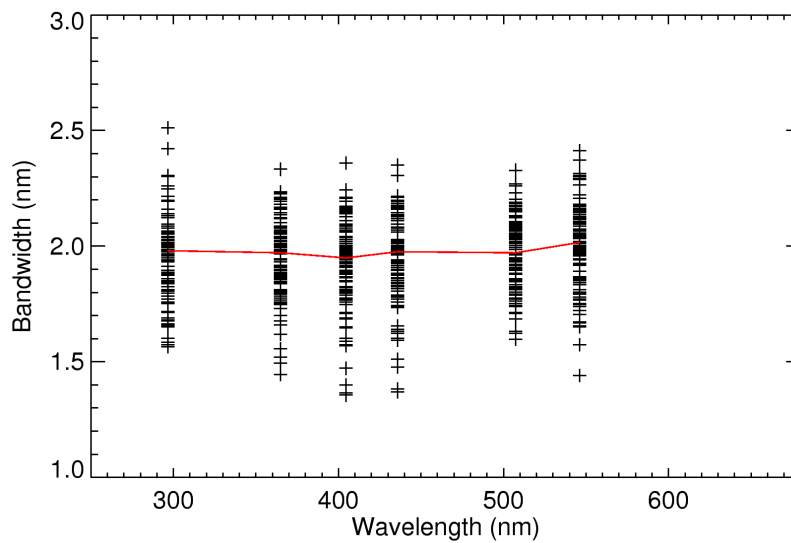
Figure 3.22: Bandwidth of each MUDIS fiber plotted over the wavelength.
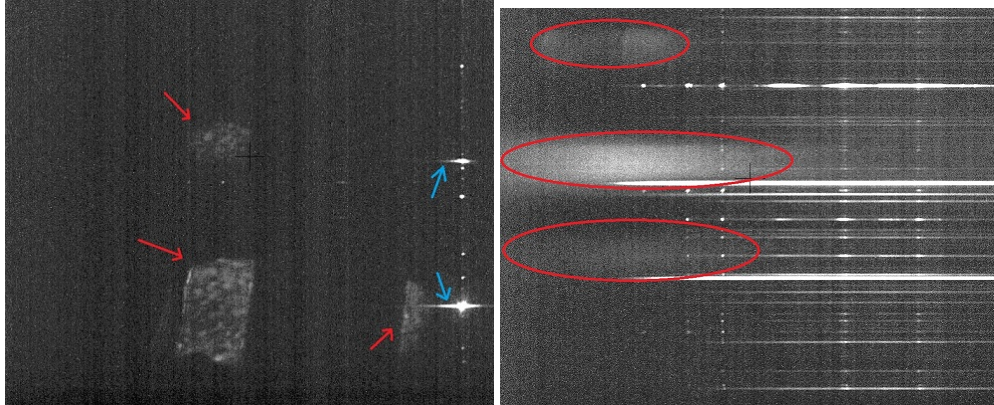
Figure 3.23: Stray light generated by a monochromatic light source on the left and a broadband light source on the right. Red arrows and circles mark stray light far away from the source signal, blue arrows mark stray light close to the light source.

the signal of those fibers causes also severe stray light in adjacent sensor rows. An example for this behavior is shown in Figure 3.24(a), where dark current and offset corrected measurements of MUDIS under cloudless sky are presented. Direct sunlight affects a single fiber and results in oversaturation (blue area) at row 375 of the sensor and the adjacent sensor rows 225–390 are affected by the spatial stray light component. In Figure 3.24(c) the spectra of the sensor rows 10, 100, 258, 502, 677 and 900 are shown, four of them are associated with broken fibers (100, 258, 677, 900) and should not show any signal at all. Nevertheless, row 100, 677 and 900 show a signal of 8 to 12 counts, which is caused by a moderate stray light influence. Due to stray light originating from the fiber illuminated by direct sunlight, row 258 is measuring nearly 400 counts. This is about 40 times higher than an actual measured signal at 310 nm, e.g., from sensor row 502. In addition, the spectral distribution of the stray light observed at row 258 differs strongly from stray light observed at the other rows. These two findings lead to the fact that rows affected by oversaturation induced stray light are beyond any post measurement correction methods. Therefore rows with a stray light signal exceeding 20 counts at 285 nm are discarded.

For each channel with less than 20 counts of stray light, a simple stray light correction method is applied: The signal of several sensor rows associated with broken fibers and measured during overcast sky is averaged and the resulting average stray light spectrum is assumed to be sufficiently representative for the whole sensor area (Figure 3.24(d)). Sensor rows illuminated by intact fibers receive negligible radiation below 290 nm due to ozone absorption in the atmosphere. Each illuminated sensor row is stray light corrected by a two-step method. First, the previously derived average stray light spectrum is scaled to the signal of the illuminated sensor row at 285 nm. Second, the scaled stray light is subtracted from the row. This method is similar to a stray light correction method developed by Jäkel et al. (2007), where spectral filters are used to derive a reference stray light for a CCD array spectroradiometer. In case of MUDIS no filters are needed for the stray light correction due to the optically dark areas on the sensor due to broken fibers.

This simple correction works reasonably well in the UV part of the spectrum. However, it is assumed that stray light derived from overcast sky will vary compared to stray light derived from radiance of a cloudless sky due to differences in the spectral distribution of the radiation where the stray light is originating from. Furthermore, the strong wavelength dependence of second order stray light originating from wavelengths longer than 300 nm, will cause an additional decrease in performance, which is expected for wavelengths longer than 600 nm.
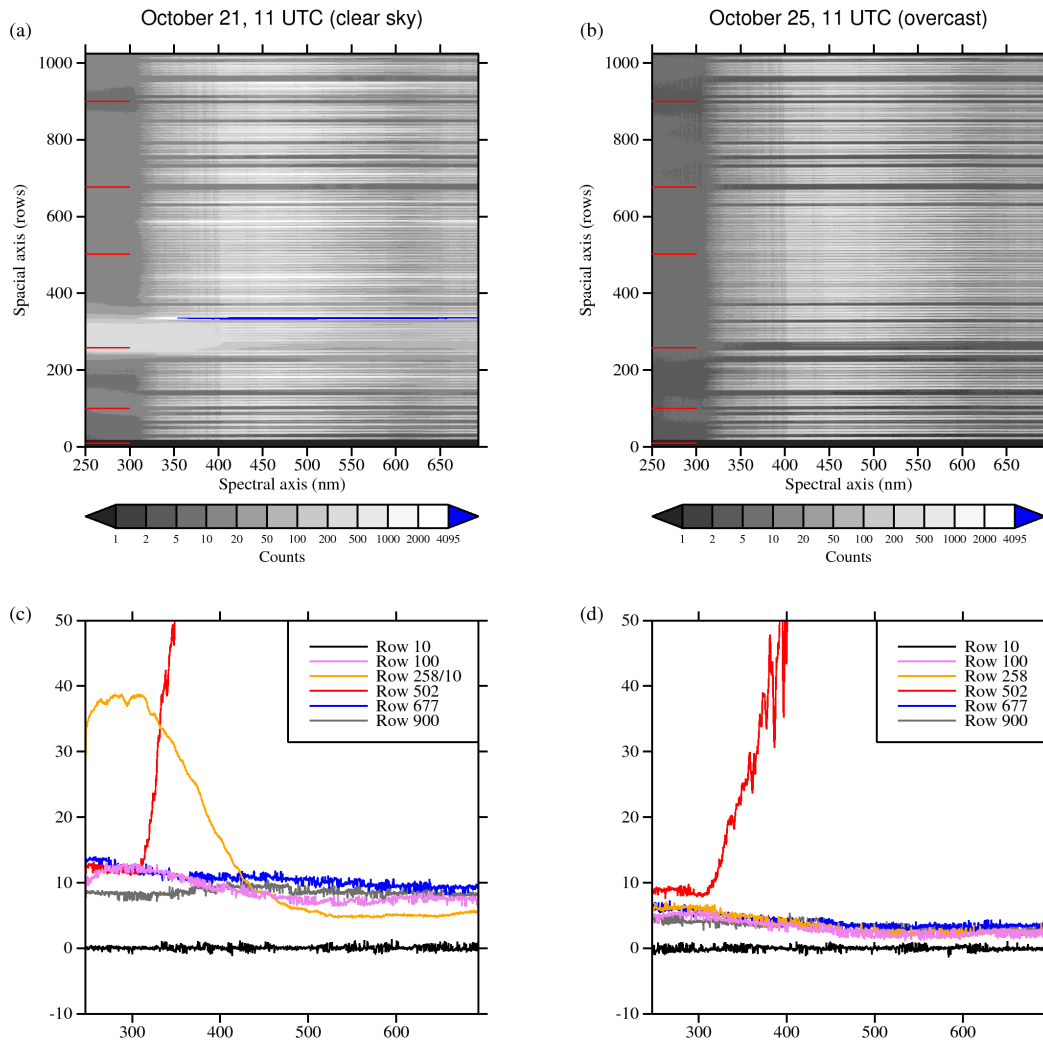
Figure 3.24: Dark current and offset corrected measurements of MUDIS under cloudless sky (a) and overcast sky (b). In (c) and (d) the spectra of different sensor rows of the performed measurements are shown. The rows 10, 100, 258, 677 and 900 should show no signal at all, since they are not illuminated by fibers placed in the entrance optics. The signal measured in this row is therefore stray light.

3.2.9 Intercalibration and Noise Equivalent Radiance

In contrast to the SCCD instrument MUDIS cannot be calibrated by the reflection plate method described in Section 2.6. The calibration process would require rotating and tilting the MUDIS entrance optics dome, in order to illuminate each of its fibers. Moving the dome would lead to sensitivity changes due to bending of the fiber bundle. Thus, a calibration method has to be applied which can be performed directly at the measuring site without a need to move the instrument during or after the calibration. An intercalibration based on synchronous measurements of MUDIS and SCCD is performed in this work in order to derive the sensitivity of the MUDIS instrument. The spectral sensitivity of MUDIS $S_{MUDIS}(\theta, \varphi, t, \lambda)$ at a measurement direction of the sky with a zenith angle of θ and an azimuth angle of φ is

31

calculated by:

$$S_{MUDIS}(\theta,\varphi,t,\lambda) = \frac{X_{MUDIS}(\theta,\varphi,t,\lambda)}{L_{SCCD,\lambda}(\theta,\varphi,t,\lambda)} \qquad (3.4)$$

where $X_{MUDIS}(\lambda)$ is the signal in counts, measured with MUDIS at wavelength λ in a particular direction of the sky with a zenith angle θ and an azimuth angle φ at time t. $L_{SCCD,\lambda}(\theta,\varphi,t,\lambda)$ is the sky radiance in mWm^{-2}nm^{-1}sr^{-1}, measured with SCCD in the same direction of the sky with a zenith angle θ and an azimuth angle φ at time t.

The instruments differ in terms of entrance optics FOV and the measurements have a time asynchronism of up to 10 s, therefore, a temporal deviation of the calculated sensitivity due to temporal and spatial variations of sky radiance during the measurements is observed. Figure 3.25(a) shows the histogram of $S_{MUDIS}(\theta,\varphi,t_i,\lambda)$ for the MUDIS channel 3 ($\theta = 48°$, $\varphi = 180°$) with $\lambda = 500\,nm$, measured 282 times over the course of four days ($i = 0,1,\ldots,281$). In order to derive the best possible MUDIS sensitivity, outliers are removed from the dataset in a four-step process. First of all, outliers greater than 4 times the standard deviation (4σ) are identified and excluded. Most of these outliers have a value of nearly 0 due to the shadow band that is shading channel 3 at around noon of each measurement day. The excluding procedure is repeated similarly by removing outliers with 3σ, 2σ and 1σ away from the mean value, while σ and the mean value are calculated anew each time outliers have been removed (Figure 3.25(b-d)). This process is performed for each wavelength and each sky direction measured by both MUDIS and SCCD. Figure 3.26 shows the spectral sensitivity derived for MUDIS channel 3. In addition the 1σ standard deviation is displayed. The sensitivity and the corresponding standard deviation increase beyond approx. 600 nm. A possible reason is a stray light influence originating from the second order diffraction of the spectrometer grating (Sharpe and Irish, 1978). Light from the wavelength region between 300 and 340 nm is additionally detected by the spectrometer at 600–680 nm due to second order diffraction. Below 300 nm the absolute signal of solar radiation is nearly zero, thus no influence due to stray light originating from the UV part of the spectrum is observed here.

An example for the sensitivity of all MUDIS channels, derived from an intercalibration performed in July 2013, is shown in Figure 3.27(a). Each of the 113 MUDIS channels has an individual sensitivity, since the transmission and the FOV of each fiber is slightly different to each another. Channels with a flat azimuth angle of 84° are marked in purple in the figure. Since a larger extent of the FOV of those MUDIS points is distorted by the horizon compared to the FOV of SCCD, the intercalibration process may cause faulty sensitivities.

Similar to Section 3.1.5 the NER of MUDIS in comparison the NER of SCCD is displayed in Figure 3.27(b). The NER of MUDIS is derived by dark current measurements with an integration time of 100 ms and an averaging of 64 measurements, which is identical to the settings chosen for the sky radiance measurements performed during the intercomparison campaigns in October 2012 and July 2013. The NER of each MUDIS channel is displayed in grey and the mean of all channels except those with a 84° horizon angle is displayed in black. The average NER of MUDIS is less than 0.2 mWm^{-2}nm^{-1}sr^{-1} for wavelengths greater than 310 nm and thus provides a significantly better detection threshold compared to the SCCD. The influence of different averages chosen for MUDIS measurements is displayed in Figure 3.28. Without any averages a measurement with 100 ms integration time is performed in about 200 ms, since the processing time of each picture is also roughly 100 ms. Therefore, a measurement with 5 averages equals to a measurement time of 1 s, 10 averages to 2 s, 20 averages to 4 s and 64 averages to 12 s, respectively. For a measurement time of 2 s, the mean NER of MUDIS is less than 0.5 mWm^{-2}nm^{-1}sr^{-1} for wavelengths longer than 310 nm. MUDIS is therefore capable of measuring sky radiance in less than two seconds with an acceptable 2 NER detection threshold of less than 1 mWm^{-2}nm^{-1}sr^{-1}.
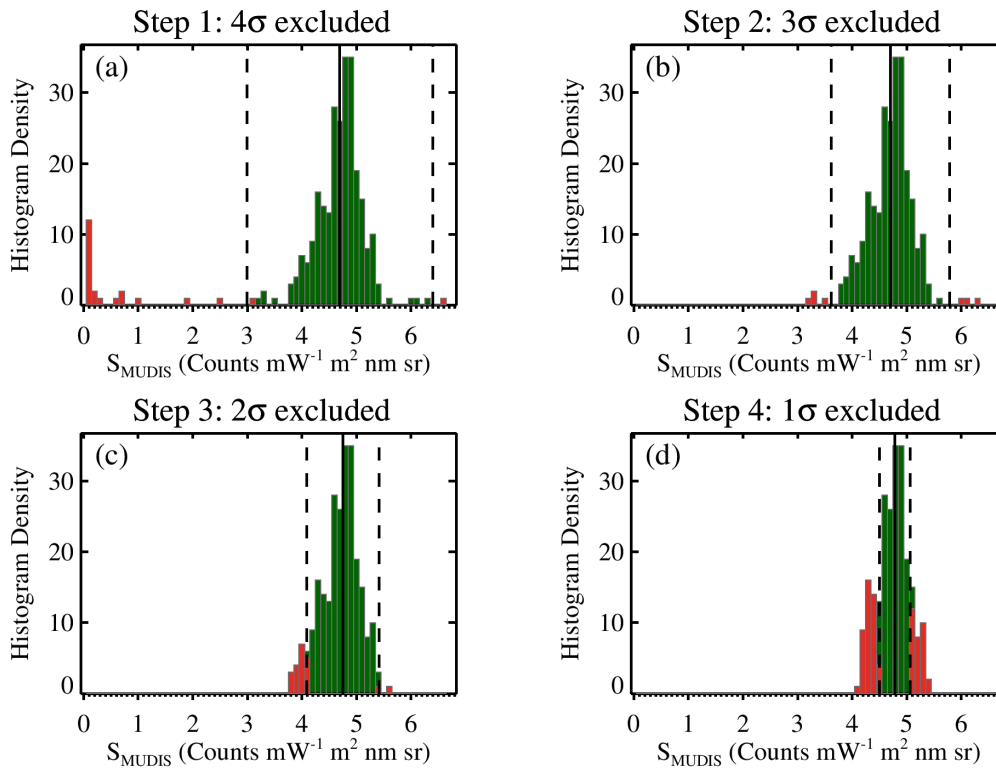
Figure 3.25: Intercalibration process of MUDIS. Shown are histograms of 282 MUDIS sensitivities derived by intercalibration with SCCD for a single viewing direction of the sky (MUDIS channel 3, zenith angle = 48°, azimuth angle = 180°) at a wavelength of 500 nm. The Figures (a-d) show the step-wise exclusion of outliers (red bars) that are 4σ, 3σ, 2σ and 1σ (black dashed line) away from the mean value of the ratios (black solid line), respectively.
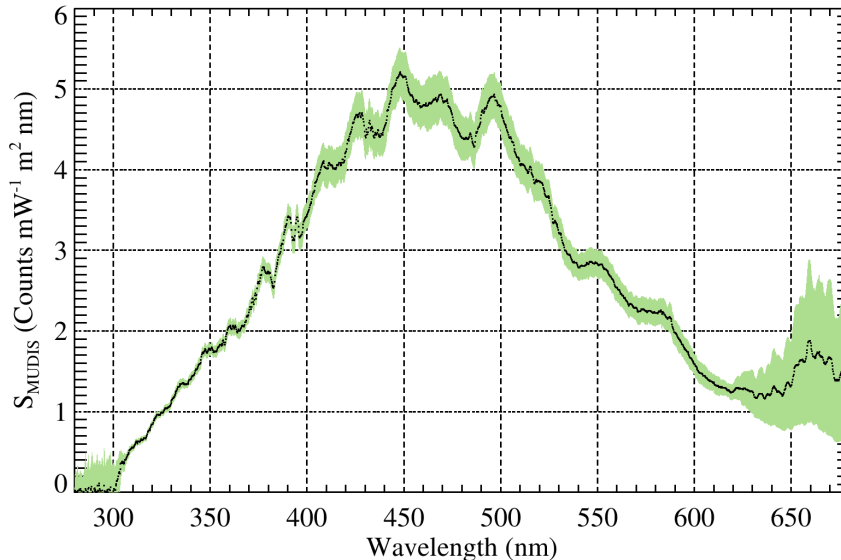
Figure 3.26: Example of spectral sensitivity of MUDIS channel 3. Each black dot of the line was derived by the intercalibration procedure illustrated in Figure 3.25. The green area symbolizes the 1σ standard deviation calculated in step four of the intercalibration process.
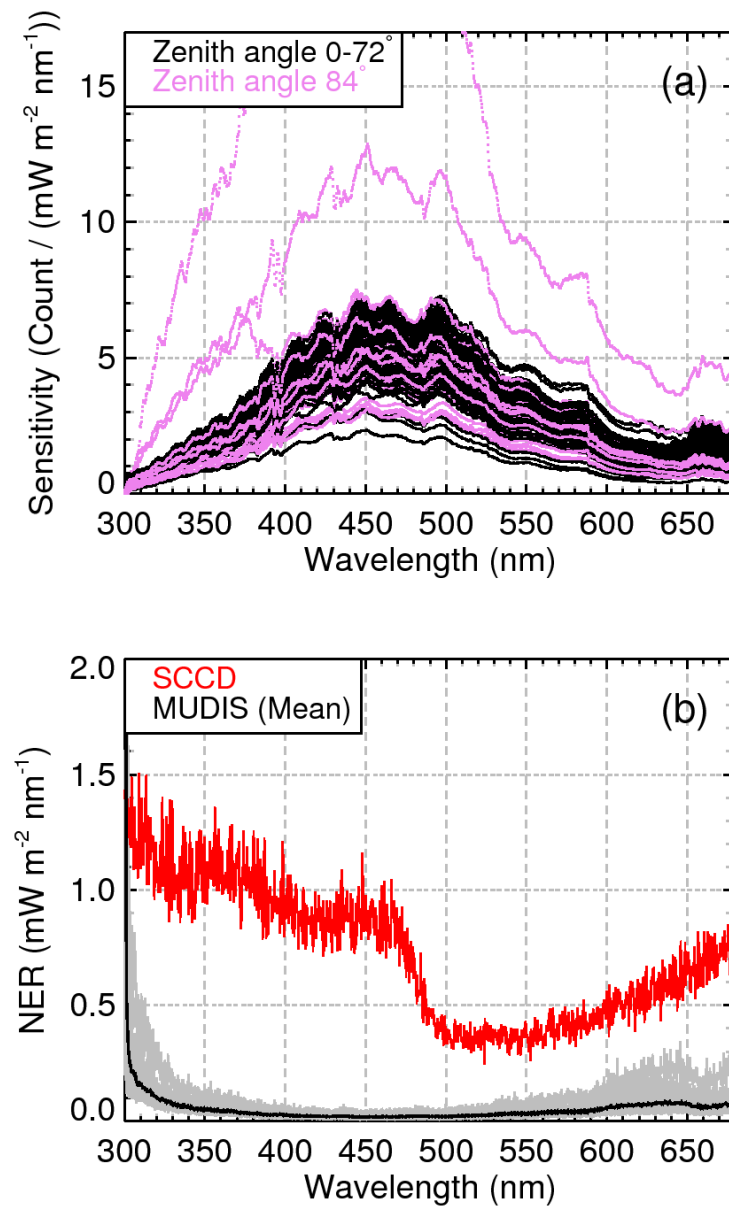
Figure 3.27: In (a) the sensitivity of all MUDIS channels is shown. In (b) the NER of MUDIS in comparison to the NER of SCCD is shown. The NER of MUDIS is derived by dark current measurements with an integration time of 100 ms and an averaging of 64 measurements. The individual NER of each MUDIS channel is plotted in grey, the mean NER derived from all channels with an azimuth angle smaller than 84° is marked in black.
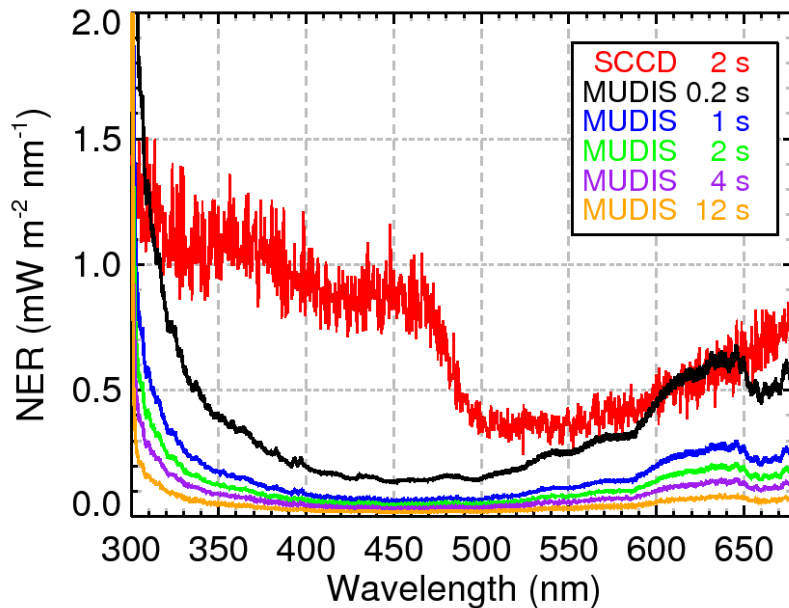
Figure 3.28: Mean NER derived from MUDIS measurements performed with different averages, resulting in measurement durations of 0.2, 1, 2, 4 and 12 seconds. In addition, the NER of SCCD is displayed in red.

3.3 Hemispherical Sky Imager (HSI)

The measurements performed with the HSI system are highly non-linear. This feature is desirable under photographic aspects since a camera should imitate the non-linear behavior of the human eye in order to capture a scenery with both dark and bright illumination. In order to use the pictures for calculations a non-linearity correction needs to be applied to the HSI system. The non-linearity of the HSI has therefore been characterized by capturing the radiance emitted by a reflection plate that is placed in a set of different distances to a 1000 W FEL lamp, varying from 0.5 to 5 m. In Figure 3.29 the results of this characterization are shown. In order to quantify the non-linearity of the instrument a reference point of the dataset derived from the non-linearity characterization is chosen. In this case, the measurement in which the mean count value of the reflectance plate is nearest to half of the maximum count value (127.5 counts) is chosen. By applying the inverse square law the true signal in counts is derived for all pictures taken of the reflection plate, standing in different distances from the 1000 W FEL lamp. The difference between measured and true signal is therefore defined as non-linearity. The relative non-linearity of each separate color channel of the HSI system is shown in Figure3.29(b), especially for high count values a significant non-linearity of up to -80% is observed. By fitting the non-linearity with a seventh order polynomial and multiplying each pixel of a HSI measurement with such a polynomial the allsky pictures are corrected for non-linearity.
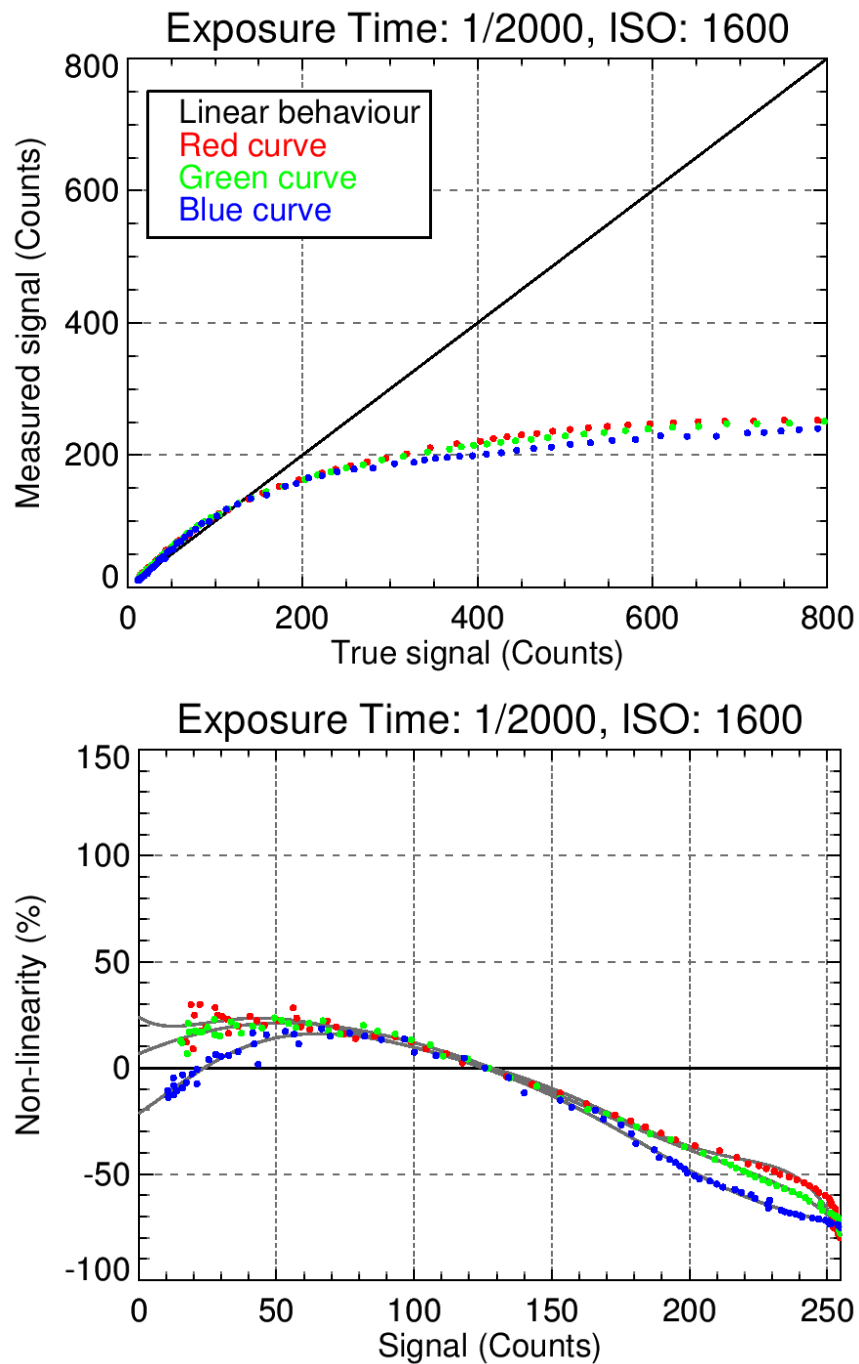
Figure 3.29: In (a) the non-linear response of the three color channels is shown. The black line represents a linear behavior between the true input signal in counts and the measured signal in counts. In (b) the non-linearity is shown in percent.

4 Comparison of MUDIS and SCCD

In October 2012 simultaneous measurements with MUDIS, SCCD and the HSI have been carried out. The first results of the comparison between MUDIS and SCCD have been published in Riechelmann et al. (2013) (see Appendix 8). In the following section the data is evaluated more comprehensively compared to the publication in order to gain more experience with MUDIS, which resulted in instrument improvements for the second measuring campaign presented in Chapter 5.

	SCCD	MUDIS
Detector	2048 pixel CCD array	1024×1002 pixel CCD sensor
ADC	16 bit	12 bit
Spectral range	265–900 nm	250–680 nm
Spectral sampling interval	0.22–0.39 nm	0.44 nm
Spatial sampling interval	113 points (scanning)	113 points (simultaneous)
Integration time	50 ms	100 ms
Averaged spectra	40	64
Temporal sampling interval	12 min	12 sec
Bandwidth	0.7–1.8 nm	1.5–2.5 nm
Radiance optics FOV	5°	9°–17°
DT (310–400 nm)	$< 3 \text{ mWm}^{-2}\text{nm}^{-1}\text{sr}^{-1}$	$< 0.5 \text{ mWm}^{-2}\text{nm}^{-1}\text{sr}^{-1}$

Table 4.1: Technical details and instrument settings of MUDIS and SCCD.

4.1 Campaign Setup and Weather Conditions

MUDIS, SCCD and HSI were set up in October 2012 on a measuring platform at IMuK, Hannover, Germany. The two compared spectroradiometers are different in many aspects. In order to correctly interpret the results of the performed instrument comparison a thorough knowledge of the relevant technical details of both instruments, shown in Table 4.1, is required:

- **Spectral Range and Sampling Interval.** The operational wavelength ranges of both instruments overlap in the UV, however the SCCD provides a wider spectral range compared to MUDIS. In addition, each instrument has an individual sampling interval, therefore the measurements of both instruments are cut to a spectral range of 280–680 nm and are interpolated to a sampling interval of 0.25 nm.

- **Spatial and Temporal Settings.** Sky radiance scans with the SCCD are performed with the same spatial distribution pattern used for the MUDIS entrance optics dome in order to avoid an interpolation. MUDIS performs the measurement of the whole pattern simultaneously with an integration time of 100 ms. In addition, 64 measurements are averaged in order to improve the signal to noise ratio and to reduce the amount of data, since each measurement needs 2 MB disk space. Therefore, a MUDIS sky radiance measurement is performed every 12 s. With an integration time of 50 ms and 40 averages the SCCD needs about 2 s for the measurement of a single pattern point. Including the

setting time of the positioning device this results in a 12 min measurement duration for the whole scan pattern. In order to compare both instruments a set of sky radiance measurements synchronous to the SCCD scan is derived from the MUDIS measurements. Those sky radiance scans derived from the MUDIS measurements can be compared to the SCCD scans, however they include a time asynchronism of up to 10 s due to the different measurement durations of MUDIS and SCCD.

- **Bandwidth Adjustment.** The bandwidth of the SCCD is more narrow compared to the bandwidth of MUDIS. In order to compare both spectra the bandwidth of the SCCD is adjusted by convoluting the measurements with a suitable slit function.

- **Entrance Optics.** The wider FOV of MUDIS compared to the SCCD will lead to different results, especially during broken clouds, where sky radiance underlies a high spatial variation. In addition, uncertainties of the SCCD positioning unit and a tilt of the FOV of individual MUDIS fibers compared to their assumed viewing angle can lead to random and systematic uncertainties in radiance measurements. An approach to quantify the influence of each particular uncertainty source is presented in Chapter 6.

The comparison measurements have been performed on four days in October 2012 in order to cover different meteorological conditions. In Table 4.2 the weather conditions and the number of measurements performed on the specific campaign day are summarized. On 20 October at 11 UTC the sky was covered with five-eighths of thin cirrus fibratus clouds. The cloud coverage varied between three-eighths and seven-eighths during the day. On 21 October the sky was nearly cloudless with only one-eighths of altocumulus clouds occurring in the time period between 09:30 and 16 UTC. On 22 and 25 October the sky was covered with eight-eighths stratocumulus clouds for the whole day. A wavelength and absolute calibration of the SCCD instrument has been performed on 19 October according to the calibration methods described in Section 2.6 and 3.1.2. An intercalibration between MUDIS and SCCD is conducted based on the measurements of the four campaign days according to the intercalibration method described in Section 3.2.9.

	20.10.	21.10.	22.10.	25.10.
MUDIS	3199	3178	3158	3096
SCCD	55	49	57	55
HSI	1826	1815	1802	117
Dominating cloud type	cirrus fibratus	altocumulus	stratocumulus	stratocumulus
11 UTC Cloud cover	5/8	1/8	8/8	8/8
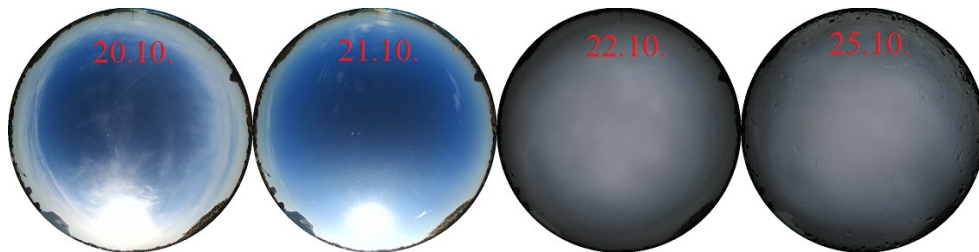
Table 4.2: Number of measurements per day performed with MUDIS, SCCD, NDACC and HSI in October 2012. The numbers in line with the instruments note the measurements performed per day from sunrise to sunset. The allsky pictures captured with the HSI show the weather conditions at 11 UTC on the campaign days.

4.2 Results

In this section the evaluation of radiance measurements performed between sunrise and sunset with MUDIS and SCCD on 20, 21, 22 and 25 October 2012 is presented. First of all, the advantage of MUDIS compared to the SCCD is illustrated in Section 4.2.1. Spectral radiance measured in the zenith direction is compared in Section 4.2.2. In Section 4.2.3 a statistical approach for the examination of the overall performance of all directions measured by MUDIS and SCCD is presented and Section 4.2.4 provides a comparison of spatial sky radiance variations measured with MUDIS and SCCD. In addition, diffuse spectral actinic irradiance (Section 4.2.5) is calculated from measurements of both instruments and intercompared in order to check the validity of spatially integrated values.

4.2.1 The Advantage of MUDIS
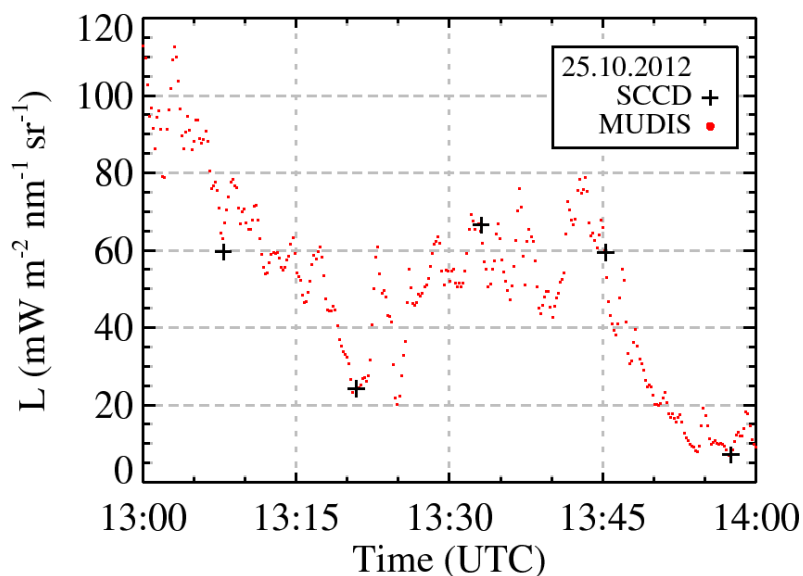
Figure 4.1: Zenith radiance measurements performed at 500 nm between 13 and 14 UTC by MUDIS and SCCD. Since a SCCD measurement takes 12 min, the zenith point is measured only 5 times during this hour. With MUDIS the zenith sky radiance is measured 300 times in the same time interval.

Especially during cloudy sky conditions the spectral radiance of the sky varies strongly. An example of the rapid change of the sky radiance is shown in Figure 4.1. The plot shows zenith radiance measured between 13 and 14 UTC with MUDIS and SCCD under cloudy conditions on 25 October at a wavelength of 500 nm. One SCCD measurement takes about 12 min, therefore the zenith point is measured only 5 times per hour. MUDIS captures the zenith radiance about 300 times in the same time span and is therefore capable of recognizing rapid changes of the angular distribution of sky radiance. In Figure 4.2 two MUDIS measurements performed at 11:04 and 11:16 UTC on 25 October are displayed. This equals the time period needed to perform an SCCD measurement. Sky radiance at 500 nm changed by up to 103%, depending on the measuring direction. This also implies, that compared to MUDIS, a sequential measurement of directions by the SCCD must inevitably lead to distorted sky radiance measurements under rapidly changing sky conditions.
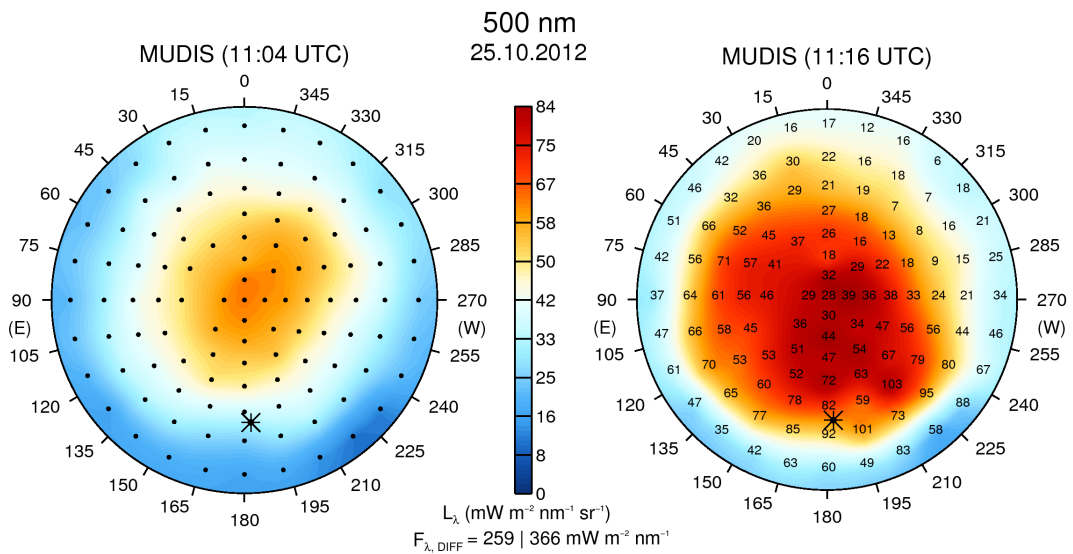
Figure 4.2: The figure shows two MUDIS sky radiance measurements, one performed at 11:04 UTC and the other one at 11:16 UTC. The numbers shown in the 11:16 UTC radiance distribution quantify the change of sky radiance in percent during the 12 min time interval which is needed for one SCCD sky radiance measurement. In this case the sky radiance varies between 6 and 103%, depending on the point of the measurement pattern.

4.2.2 Spectral Zenith Radiance

Analogous to Pissulla et al. (2009) the performance of the two spectroradiometers is compared by calculating the ratio of spectral radiance which was measured with MUDIS and SCCD in the zenith direction of the sky. In Figure 4.3 four pairs of measurements captured around 11 UTC at 20, 21, 22 and 25 October are shown. For the wavelength region between 320 and 600 nm the difference between MUDIS and SCCD is less than 5% except for the cloudless condition, in which the difference increases to 16% at 600 nm. This behavior has been found for several MUDIS channels near the zenith direction. Those channels were always measuring sky radiance of clear blue sky. The increased difference is presumably connected to uncertainties of the stray light correction method applied to MUDIS and discussed in more detail in Section 4.3. MUDIS performance also rapidly decreases in all examined situations for wavelengths longer than 600 nm. It is assumed that this is a result of the inability of the applied correction method to reduce second order stray light (Section 3.2.8) and is also discussed in more detail in Section 4.3. In order to check if the observed spectral variations at 11 UTC are random or systematic differences, the diurnal variation is examined in the following at 320 nm and 500 nm.

Figure 4.4 shows the diurnal variation of spectral radiance measured with MUDIS and SCCD between sunrise and sunset in the zenith direction at the two chosen wavelengths 320 and 500 nm. Measurements below the detection threshold of the SCCD instrument ($< 3 \, \mathrm{mWm^{-2}nm^{-1}sr^{-1}}$) were excluded from the dataset. Throughout the first two campaign days the ratios of zenith sky radiance measured with both instruments show a 1σ standard deviation of up to 6.5% with an insignificant bias of less than 1.7%. On 22 October a standard deviation of up to 8% at 320 nm is observed, while the standard deviation at 500 nm is less than 2.7%. Data measured on 25 October show an even higher standard deviation of up to 11.6% at 320 nm and 7.5% at 500 nm with a bias of -2.6% at 320 nm and -1.7% at 500 nm. The higher standard deviation is explainable by the high temporal variation of sky radiance on 25 October
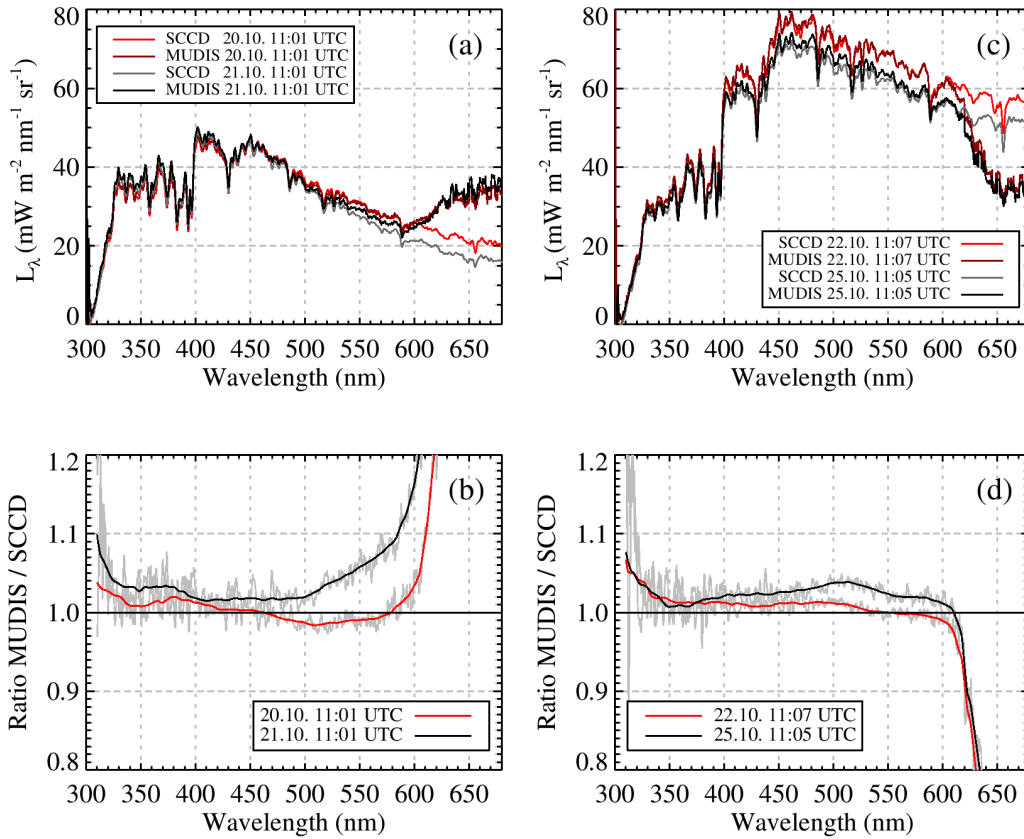
Figure 4.3: Spectral radiance measured in the zenith of the sky with MUDIS and SCCD on 20, 21, 22 and 25 October. A median filter is applied to the ratios displayed in the bottom plots; the underlying grey lines show the unfiltered data.

compared to the other three campaign days (Figure 4.4(b)). FOV differences of the instruments and time asynchronism between MUDIS and SCCD measurements result therefore in a higher variation between those instruments on 25 October.

4.2.3 Statistical Evaluation of MUDIS Sky Radiance Measurements

Due to differences in instrument FOV and up to 10 s asynchronism between MUDIS and SCCD measurements, a random variation between the measurements of both instruments is to be expected. In order to quantify the systematic and random uncertainty, the MUDIS/SCCD spectral sky radiance ratios are calculated for each measured direction. All measurements performed from sunrise to sunset are therefore combined into an individual dataset for each particular measurement day. MUDIS data points that are either compromised by broken fibers, affected by high stray light, oversaturated in the circumsolar region or measured spectral radiance of less than the SCCD detection threshold are excluded from the dataset. MUDIS measurements performed at 84° zenith angle have more obstacles like trees or buildings in their wider FOV compared to SCCD measurements. This leads to systematic errors that are partially attenuated by the intercalibration process; nevertheless, the random uncertainty stays high for horizon points. Therefore, outliers greater than four times the standard deviation (4σ) are also removed from the dataset. An overview over all excluded points is given in Table 4.3. Broken fibers reduce the dataset by a constant amount of 3.5% and less than 1.5% of the measurements

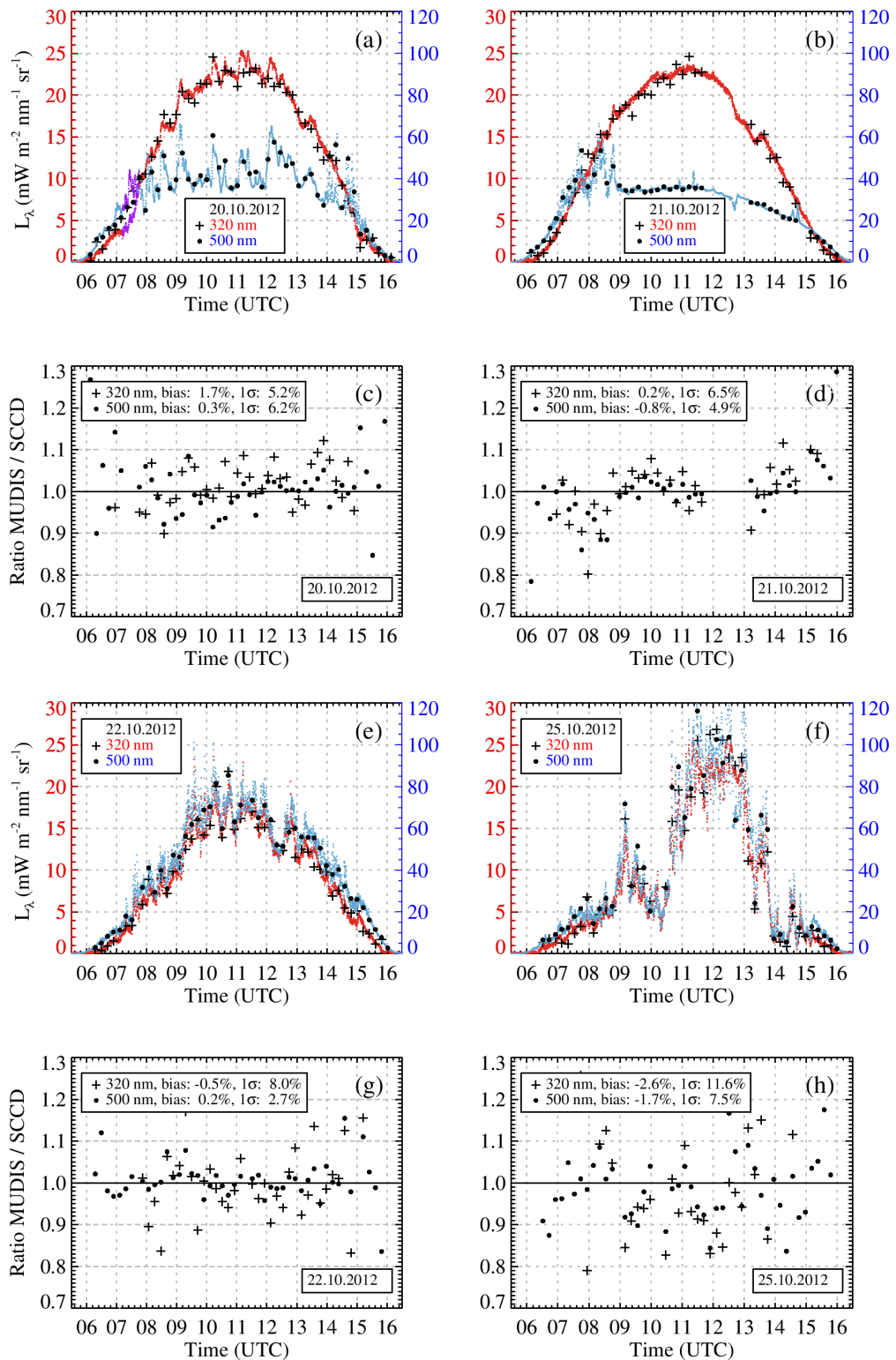Figure 4.4: Diurnal variation of the spectral zenith radiance measured with MUDIS and SCCD on 20, 21, 22 and 25 October. In plot (a), (b), (e) and (f) absolute values of SCCD at 320 nm (crosses) and 500 nm (dots) are shown. In addition, MUDIS data at 320 nm (red line) and at 500 nm (blue line) is shown. In plot (c), (d), (g) and (h) the ratios of synchronized MUDIS and SCCD measurements at 320 nm and 500 nm are shown.

	20 October	21 October	22 October	25 October
Total points	5537 (100%)	4520 (100%)	5198 (100%)	4972 (100%)
Detection threshold	1004 (18.1%)	848 (18.8%)	1533 (29.5%)	2144 (43.1%)
4σ outliers	81 (1.5%)	66 (1.5%)	27 (0.5%)	22 (0.4%)
Broken fibers	196 (3.5%)	160 (3.5%)	184 (3.5%)	176 (3.5%)
Stray light	716 (12.9%)	443 (9.8%)	0 (0%)	63 (1.3%)
Circumsolar region	188 (3.4%)	158 (3.5%)	0 (0%)	0 (0%)
Total rejected	2185 (39.5%)	1675 (37.1%)	1744 (33.6%)	2567 (48.4%)
Total accepted	**3352 (60.5%)**	**2845 (62.9%)**	**3454 (66.4%)**	**2567 (51.6%)**

Table 4.3: MUDIS measurement points that are rejected for the statistical comparison of MUDIS and SCCD at 320 nm, discussed in Section 4.2.3.

are rejected as outliers. The amount of noisy measurements depends on the weather conditions and the chosen time frame. During 20 October (cirrus fibratus covered sky) and 21 October (cloudless), up to 18.8% of the measurements were discarded due to a signal value below the SCCD detection threshold. For campaign days with overcast conditions (22 and 25 October) the amount of rejected datapoints increases up to 43.1%. Stray light due to oversaturation and rejected points in the circumsolar region contribute with up to 16.3% to the rejected points for sunny days and consequently no points should be rejected during overcast days. The few stray light points on 25 October occur during a short broken cloud situation in the afternoon. In total between 51.6% and 66.4% of all ratios are used for the statistical evaluation at 320 nm. At 500 nm less than 3.3 % of the dataset is discarded due to a signal value below the SCCD detection threshold, therefore more ratios can be used for the evaluation at this wavelength.

The remaining dataset of MUDIS/SCCD ratios are displayed in form of histograms at 320 and 500 nm for each of the four campaign days in Figure 4.5. On 20 October the sky was covered mainly by cirrus fibratus clouds. On that day the mean bias of all MUDIS/SCCD sky radiance ratios is 2.1% with a 1σ standard deviation of 8.7% at 320 nm and 0.4% with a 1σ standard deviation of 6.8% at 500 nm. For a mainly clear sky day on 21 October the mean bias is $<0.1\%$ with a 1σ standard deviation of 9.2% at 320 nm and -0.1% with a 1σ standard deviation of 6.3% at 500 nm. For overcast sky conditions on 22 October the mean bias is -1.7% with a 1σ standard deviation of 13.3% at 320 nm and 0.3% with a 1σ standard deviation of 6.0% at 500 nm. For mainly overcast sky conditions on 25 October the mean bias is -7.3% with a 1σ standard deviation of 16.5% at 320 nm and -0.7% with a 1σ standard deviation of 11.1% at 500 nm.

The wavelength dependence of the mean bias and the 1σ standard deviation calculated from the dataset of MUDIS/SCCD sky radiance ratios of the four campaign days is shown in Figure 4.6. The mean bias between 320 and 600 nm is less than 3% for the first three measurement days. On 25 October the mean bias increases to 7% which indicates a change of instrument sensitivity. It is assumed that condensation inside of the MUDIS entrance optics dome, which occurred during that day due to occasional rainfall and high relative humidity, is the cause for the sensitivity change of MUDIS. Comparable to Figure 4.2.2, the mean bias and the standard deviation is increasing rapidly for wavelengths longer than 600 nm on 20 and 21 October, as a result of the second order stray light uncertainty. The mean bias and systematic difference between MUDIS and SCCD is lower for overcast conditions on 22 and 25 October, with a mean bias of less than 4% for wavelengths up to 680 nm. It is assumed that the smaller bias compared to cloudless conditions is a result of the intercalibration process and that the smaller standard deviation is a result of the wavelength dependence of second order
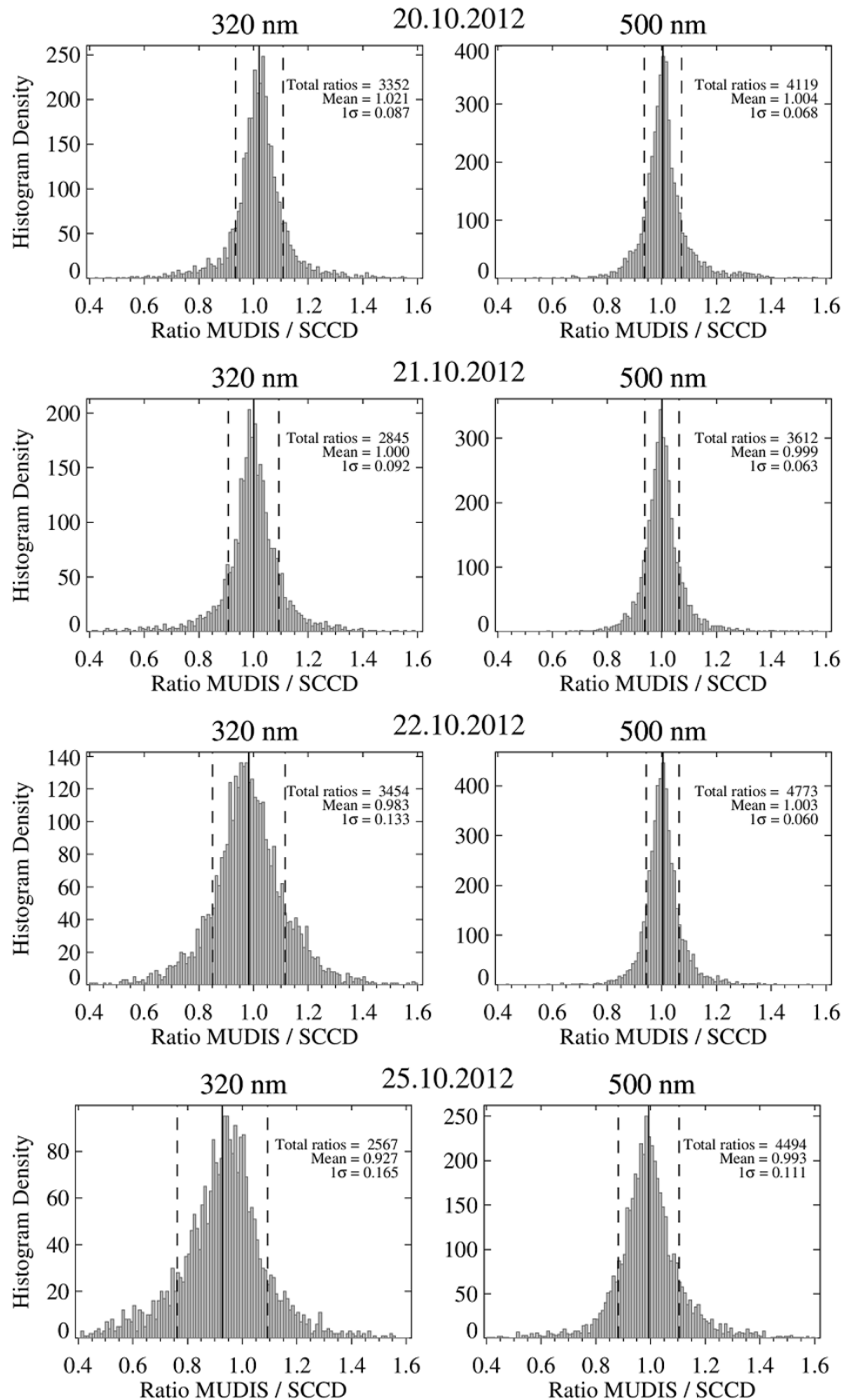
Figure 4.5: Histograms of MUDIS/SCCD spectral sky radiance ratios at 320 and 500 nm for 20, 21, 22 and 25 October. The vertical dashed lines represent the corresponding standard deviations, the vertical solid lines the mean of all examined ratios.

stray light: Overcast days show a smaller variation of spectral differences between UV and IR part of the spectrum due to the absence of cloudless sky.
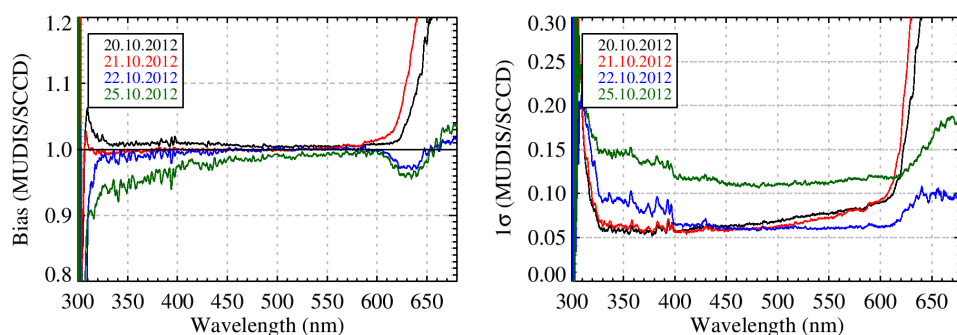
Figure 4.6: Wavelength dependence of the bias (left) and the 1σ standard deviation (right), calculated from MUDIS/SCCD spectral sky radiance ratios for 20, 21, 22 and 25 October.

The 1σ standard deviation calculated from all MUDIS/SCCD ratios during the first two campaign days is between 6% and 9% for 20 and 21 October in the wavelength range between 320 and 600 nm. The standard deviation increases rapidly for wavelengths shorter than 320 nm and longer than 600 nm. It is assumed that the 3% increase of the standard deviation observed between 400 and 600 nm is linked to the FOV difference between the MUDIS and SCCD entrance optics. Rayleigh scattering leads to less spatial variation of sky radiance at shorter wavelengths, thus the FOV difference causes less variation between the MUDIS and SCCD measurements. In addition, uncertainties arising from the applied stray light correction method could also lead to increased uncertainties with longer wavelengths. Both effects should also increase under broken cloud conditions, since clouds enhance sky radiance stronger towards longer wavelengths, compared to cloudless sky (Wuttke and Seckmeyer, 2006). The examination of this assumption is part of the evaluation of the second measurement campaign performed in July 2013 in Section 5, since during the first campaign in October 2012 an insufficient amount of measurements were conducted under broken cloud conditions.

During overcast sky on 22 October the standard deviation is about 6%–7% between 400 and 600 nm. An overcast sky is characterized by a spatial and temporal variation (Figure 4.4) of sky radiance, depending on the anisotropy of the optical thickness and the movement speed of the observed clouds. Mie scattering is the dominating factor here; therefore no significant increase of the standard deviation with longer wavelengths is occurring. A higher standard deviation of 7%–11% is observed between 330 and 400 nm and between 600 and 680 nm. The higher standard deviation at wavelengths smaller than 400 nm might be caused by a combination of low absolute values of sky radiance compared to wavelengths longer than 400 nm and the increasing FOV of MUDIS which increases with shorter wavelengths. On 25 October the variation of sky radiance was significantly higher compared to 22 October (Figure 4.4). FOV differences and the 10 s asynchronism between MUDIS and SCCD are therefore resulting in a standard deviation of about 11%–16% between 320 and 600 nm, which is about 5% higher compared to 22 October.

4.2.4 Spatial Distribution of Sky Radiance

Figure 4.7 shows MUDIS and SCCD sky radiance measurements as a function of zenith and azimuth angle, performed at around 11 UTC on 21 October during cloudless sky conditions.
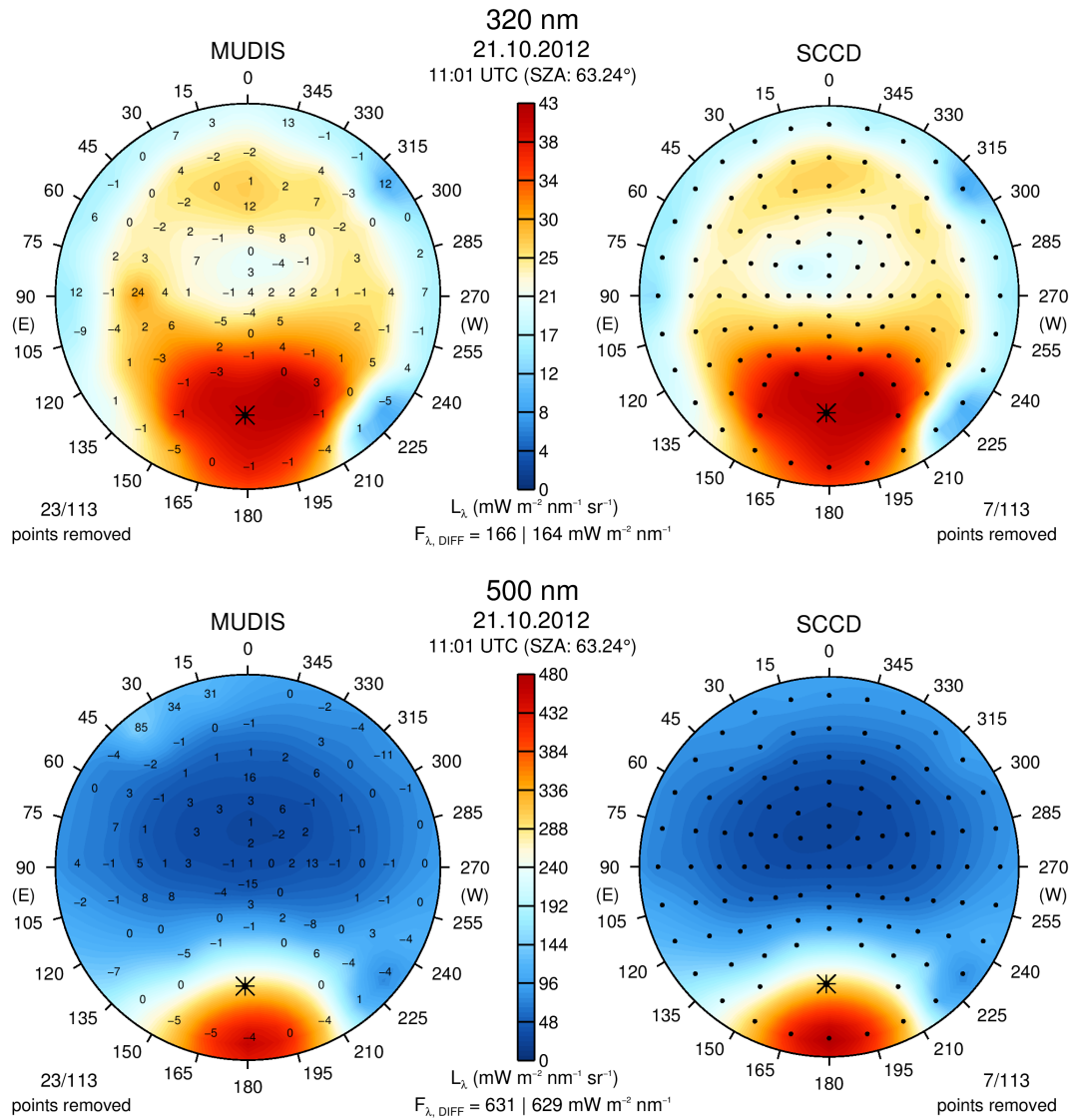
Figure 4.7: Spatial distribution of sky radiance at 320 nm (top) and 500 nm (bottom) measured under cloudless sky on 21 October with MUDIS (left) and SCCD (right). The numbers in the MUDIS sky maps represent the percent difference between MUDIS and the corresponding SCCD measurement.
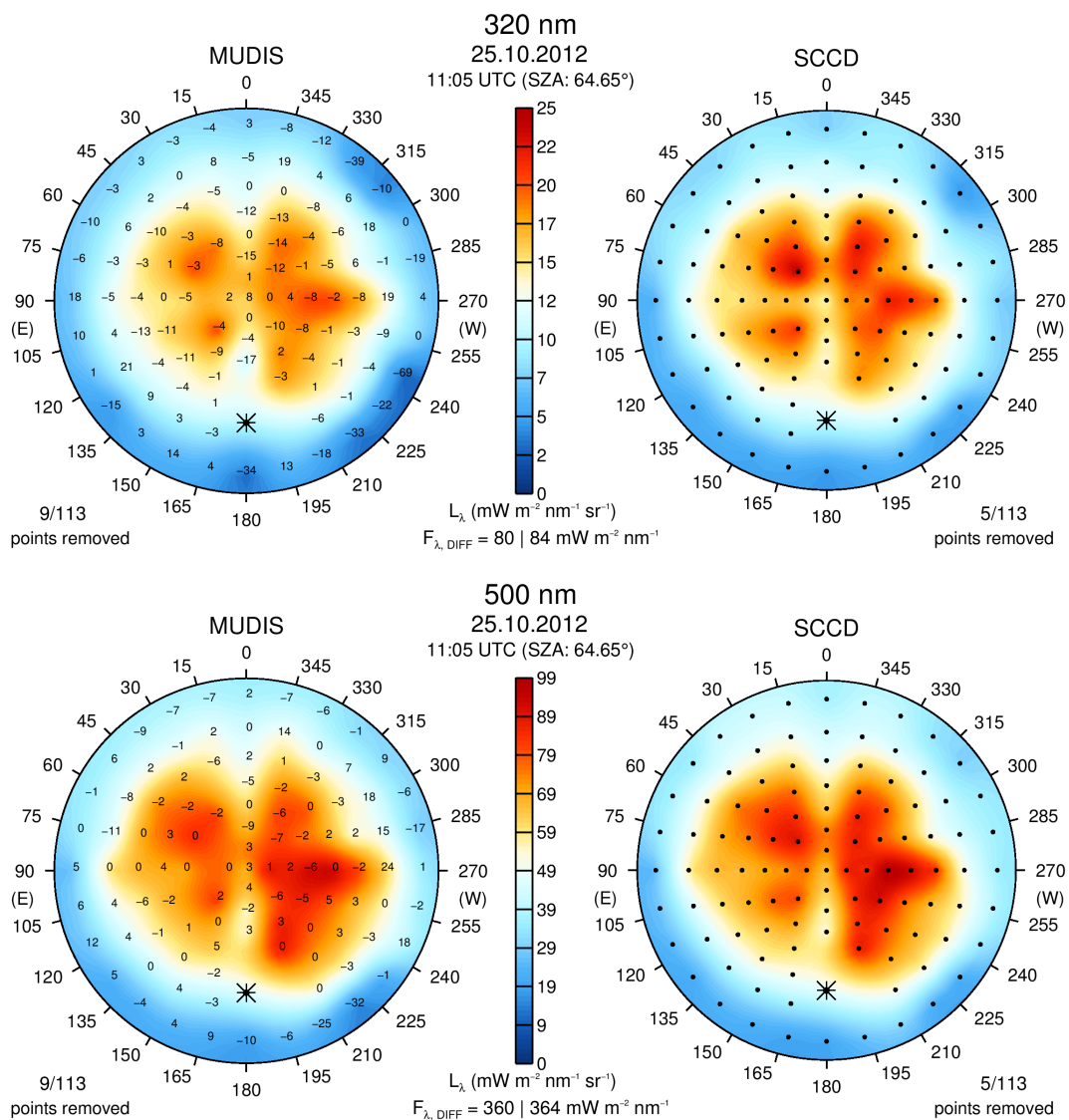
Figure 4.8: Spatial distribution of sky radiance at 320 nm (top) and 500 nm (bottom) measured under overcast sky on 25 October with MUDIS (left) and SCCD (right). The numbers in the MUDIS sky maps represent the percent difference between MUDIS and the corresponding SCCD measurement.

The two representative wavelengths 320 and 500 nm are shown as polar plots (further denoted as sky maps). The black dots in the SCCD sky map represent the measuring pattern. The numbers in the MUDIS sky maps represent the percent difference between MUDIS and the corresponding SCCD measurement. The 23 missing numbers of the MUDIS pattern are measurement points that have been removed due to damaged fibers (4 points), high stray light (12 points) and influence by direct solar radiation in the circumsolar region (7 points). The angular distribution of sky radiance measured with MUDIS and SCCD agrees well for both examined wavelengths. The possible effect of removing that amount of MUDIS datapoints on the calculation of integrated radiometric quantities is examined in Section 4.2.5.

Figure 4.8 shows the spectral sky radiance distribution of a sky covered with stratocumulus clouds at 320 and 500 nm measured with MUDIS and SCCD at 11:04 UTC on 25 October, analogous to Figure 4.7. Due to the absence of direct sunlight, no points have to be removed due to oversaturation and stray light, leaving four points removed due to broken fibers. Again, the angular distribution of sky radiance measured with MUDIS and SCCD agrees well for both examined wavelengths. Note that Figure 4.2 shows the two measurements of MUDIS at the beginning and the end of the SCCD sky scan presented in Figure 4.8. During the 12 min SCCD scan time the sky radiance increased by up to 103%, resulting in a distorted angular distribution of the sky radiance measured by the scanning instrument.

4.2.5 Spectral Actinic Irradiance
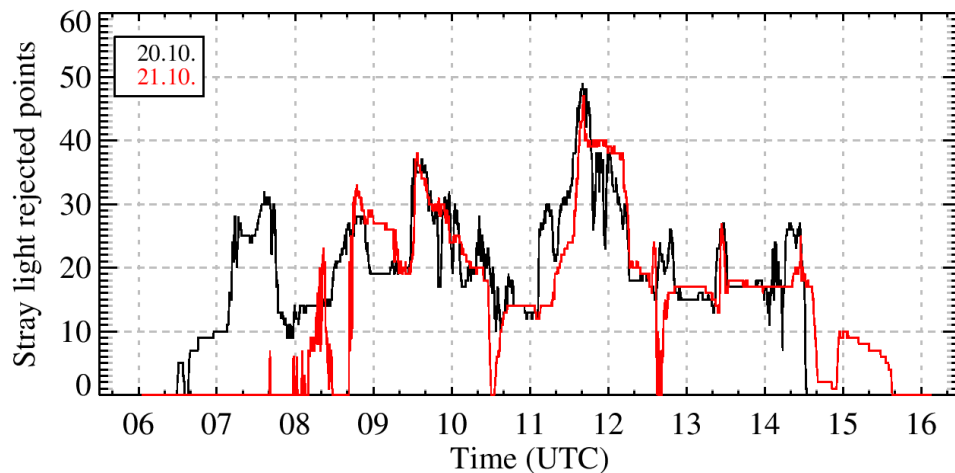
Figure 4.9: Diurnal variation of MUDIS datapoints rejected due to the >20 counts at 285 nm stray light criterion (Section 4.2.5). Up to 49 measurement points have to be discarded during direct sunlight.

The statistical comparison of MUDIS/SCCD ratios provides a good agreement of both instruments. Nevertheless, especially during cloudless conditions up to 49 measurement points have to be discarded due to stray light issues (Figure 4.9). Missing points might lead to significant uncertainties when integrating over the hemisphere. Therefore, an integration of the measured spectral sky radiance over the hemisphere is performed, which yields the downwelling spectral diffuse actinic irradiance $F_{\lambda,DIFF}(\lambda)$ (Seckmeyer et al., 2010). Before integrating the spectral sky radiance, faulty measurement points resulting from four broken
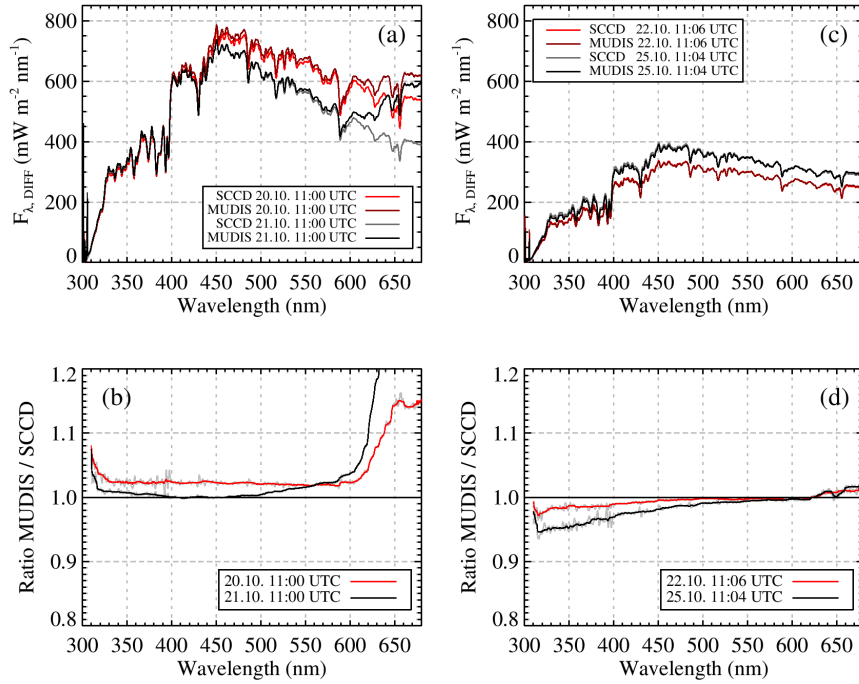
Figure 4.10: Spectral actinic irradiance measured with MUDIS and SCCD on 20, 21, 22 and 25 October. A median filter is applied to the ratios displayed in the bottom plots; the grey lines show the unfiltered data.

fibers, oversaturation in the circumsolar region and measurements with high stray light (>20 counts at 285 nm) are removed from the MUDIS dataset. From the SCCD dataset only points in the circumsolar region are removed. The remaining points of both datasets are interpolated to a 5° grid using kriging interpolation (Isaaks and Srivastava, 1989). The calculation of $F_{\lambda,DIFF}$ is performed after Kylling et al. (2003):

$$F_{\lambda,DIFF} = \int_0^{2\pi} \int_0^{\pi/2} L_\lambda(\theta, \phi, \lambda) \sin(\theta) d\theta d\phi \qquad (4.1)$$

where θ is the zenith angle, ϕ the azimuth angle, λ the wavelength and $L_\lambda(\theta, \phi, \lambda)$ the spectral sky radiance. Figure 4.11 shows the ratio of the spectral actinic irradiance measured with MUDIS and SCCD on 20, 21, 22 and 25 October 2012 at around 11 UTC. In order to remove fluctuations due to remaining differences in instrument bandwidth and wavelength shifts, a median filter is applied. On 20 October (cirrus fibratus) and 21 October (cloudless) the actinic irradiance measured with both instruments agrees within 4% between 320 and 600 nm and increases rapidly beyond 600 nm. On 22 October (overcast) the difference is less than 3% between 320 and 680 nm. On 25 October (overcast) the difference is up to 6%, the higher difference is consistent with the findings of Section 4.2.3, a condensation issue of the MUDIS entrance optics is assumed to be the reason for the systematic difference in the UV.

The diurnal variation of the actinic irradiance at 320 and 500 nm during the four measurement days is shown in Figure 4.11. Measurements of spectral actinic irradiance smaller than $10 \, \mathrm{mWm^{-2}nm^{-1}sr^{-1}}$, which occur at sunrise and sunset, are not taken into account. The bias of MUDIS/SCCD actinic irradiance ratios on 20, 21 and 22 October is in between -1.5% and 1.6%. The 25 October shows again a higher bias of up to -4.8%. The 1σ standard deviation of
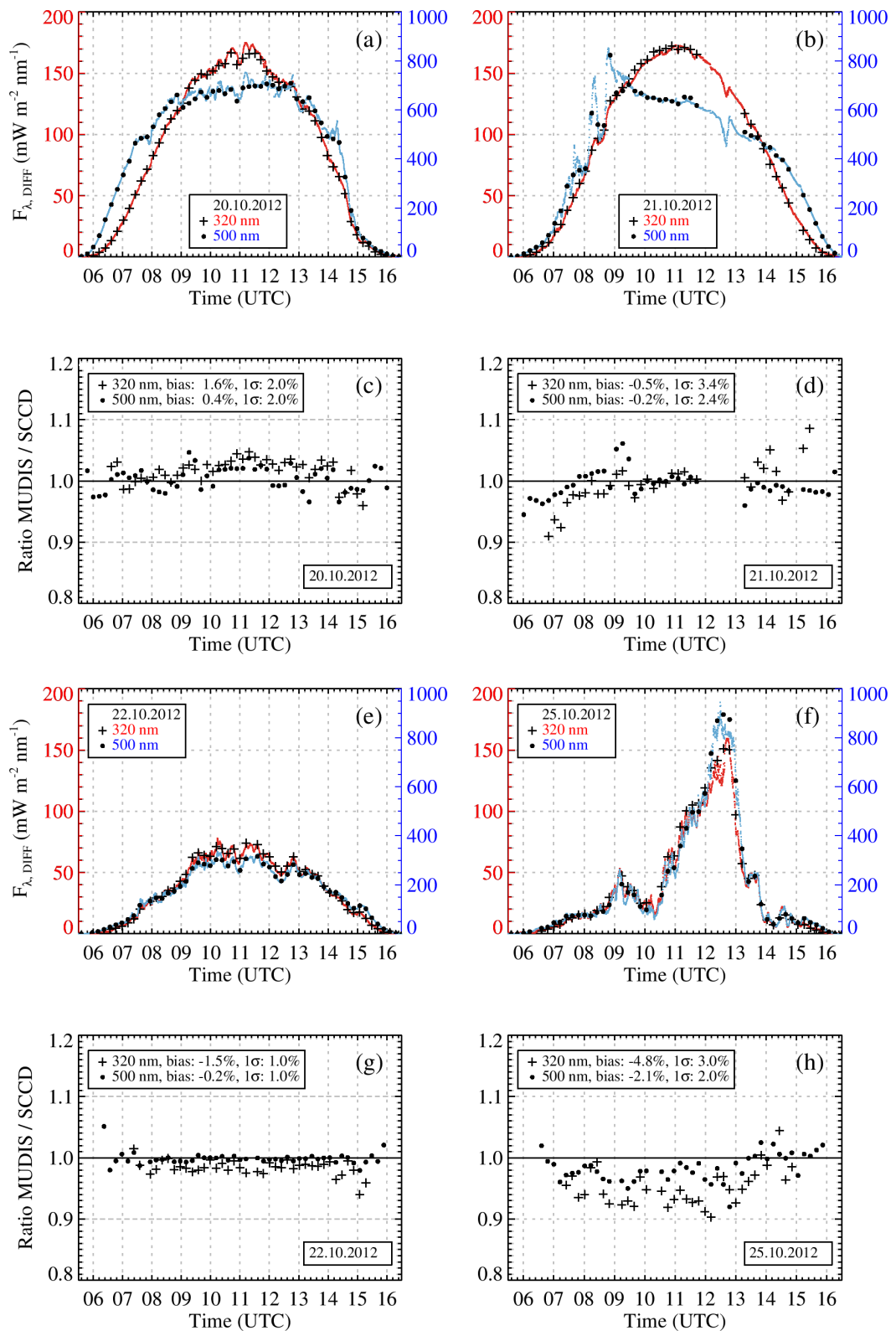
Figure 4.11: Diurnal variation of the actinic irradiance measured with MUDIS and SCCD on 20, 21, 22 and 25 October. In plot (a), (b), (e) and (f) absolute values of SCCD at 320 nm (crosses) and 500 nm (dots) are shown. In addition, MUDIS data at 320 nm (red line) and at 500 nm (blue line) is shown. In plot (c), (d), (g) and (h) the ratios of synchronized MUDIS and SCCD measurements at 320 nm and 500 nm are shown.

all four days is less than 3.4%. Despite the high amount of discarded MUDIS measurement points the actinic irradiance calculated for both instruments agrees well, since the kriging interpolation works quite well with the remaining amount of data points.

4.3 Campaign Summary and Discussion

The first instrument comparison campaign with MUDIS has been conducted in October 2012. Synchronous measurements of MUDIS and SCCD were performed on four days with different meteorological conditions: On 20 October the sky was mainly covered with a thin layer of cirrus fibratus clouds, on 21 October the sky was nearly cloudless and on 22 and 25 October the sky was overcast with stratocumulus clouds. The difference between MUDIS and SCCD measurements of the spectral zenith radiance performed at around 11 UTC on the four campaign days is less than 5% in the wavelength region between 320 and 500 nm. However, the diurnal variation of zenith radiance at 320 and 500 nm is higher with up to 6.5% for cirrus fibratus covered sky and cloudless sky. Overcast days show an even higher standard deviation of up to 11.6%. The high diurnal deviation of zenith radiance results from the different instrument FOVs and the 10 s asynchronism between the instruments. Since only up to 57 measurements per viewing direction are performed with the SCCD per day, a statistical evaluation of MUDIS/SCCD ratios of all 113 viewing directions has been performed for each campaign day. The systematic difference between 320 and 600 nm is less than 3% for the first three days and up to 7% on 25 October, which is probably due to condensation issues of the MUDIS entrance optics dome on that day. As a result the ventilation described in Section 3.2.2 has been developed in order to ensure a condensation-free entrance optics.

The spatial distribution of sky radiance at 320 and 500 nm is investigated at 11 UTC for a cloudless (20 October) and an overcast (25 October) situation and shows a good agreement. However, during cloudless conditions up to 49 MUDIS data points are rendered useless due to stray light when two or more fibers of the MUDIS entrance optics are illuminated by direct sunlight. During cloudless conditions on average 16% of all measurement points are unusable due to stray light caused by oversaturation. As a result of these findings, a shading unit has been developed by Niedzwiedz (2013), in order to improve the data availability under direct sunlight (Section 3.2.3).

Despite the high amount of rejected points due to stray light it is possible to calculate spectral actinic irradiance by integration of MUDIS and SCCD radiance measurements with a difference of less than 5% between 320 and 600 nm. The diurnal variation of MUDIS and SCCD actinic irradiance is shows a bias of less than 5% with a standard deviation of less than 3.4% at 320 and 500 nm.

The applied stray light correction is assumed to cause increased uncertainties in two cases. For a few clear blue sky measurements performed at around noon the bias between MUDIS and SCCD gradually increases for wavelengths longer than 500 nm. Since the correction algorithm is based on a stray light characterization performed under overcast conditions, the observed behavior might be caused by differences between stray light appearing under cloudless and overcast conditions. However, the statistical examination of MUDIS measurements in Section 4.2.3 shows no bias between MUDIS and SCCD in the wavelength region longer than 500 nm. This indicates that either only very few points are affected for a short period of time or the deviations balance out over all measurement directions and over the course of the day. However, the increase of the standard deviation with longer wavelengths for days with cloudless and cirrus fibratus covered sky might be partially caused by the uncertainty of the applied stray light correction method.

The rapidly increasing bias and standard deviation observed for comparisons of MUDIS

and SCCD at wavelengths longer than 600 nm is explainable with the influence of the second order stray light originating from the UV wavelength region. The applied stray light correction method is not capable of correcting the wavelength dependence of second order stray light, therefore the MUDIS performance in the wavelength region between 600 and 680 nm is acceptable under overcast conditions, but shows a high bias and standard deviation compared to the SCCD in the wavelength region between 600 and 680 nm especially during days with cloudless and cirrus fibratus covered sky.

5 Comparison of MUDIS, SCCD and NDACC Instrument

The results of the previous campaign led to improvements of MUDIS. In particular a shading unit and a ventilation system were developed and equipped to the entrance optics dome. The improvements were tested in July 2013 during a second comparison campaign. In addition to MUDIS, SCCD and HSI the NDACC instrument was set up for zenith radiance measurements.

	SCCD	MUDIS	NDACC
Detector	2048 pixel	1024×1002 pixel	1 pixel
ADC	16 bit	12 bit	14 bit
Spectral range	265–900 nm	250–680 nm	280–1000 nm
Spectral sampling interval	0.22–0.39 nm	0.44 nm	0.25 nm
Spatial sampling interval	113 points	113 points	1 point
Temporal sampling interval	12 min	12 sec	21 min
Bandwidth	0.7–1.8 nm	1.5–2.5 nm	0.5–2 nm
Radiance optics FOV	$5°$	$9°–17°$	$5°$
DT (310–400 nm)	<3 $\mathrm{mWm^{-2}nm^{-1}sr^{-1}}$	<0.5 $\mathrm{mWm^{-2}nm^{-1}sr^{-1}}$	<0.03 $\mathrm{mWm^{-2}nm^{-1}sr^{-1}}$

Table 5.1: Technical details and instrument settings of the SCCD, MUDIS and the NDACC instrument.

5.1 Campaign Setup and Weather Conditions

Analogous to the first campaign, MUDIS, SCCD and HSI were set up in July 2013 on a measuring platform at IMuK, Hannover, Germany. In addition to these instruments the spectral radiance in the zenith direction of the sky was measured with the NDACC instrument every 21 min. Concurrent measurements with all instruments have been performed between sunrise and sunset for 8 days. Hence, instrument comparison and MUDIS intercalibration can be carried out on different measurement days. Measurements performed on 14, 15, 16 and 18 July are used for instrument comparison while the intercalibration is based on the measurements performed on 12, 13, 17 and 19 July. The weather conditions at 11 UTC and the number of measurements performed on each campaign day are summarized in Table 5.2. On 14 July an overcast sky with seven-eighths to eight-eighths stratus clouds was observed during the whole day. This date is thus chosen for the evaluation of the MUDIS performance under overcast conditions. On 15 July at 11 UTC two-eighths of the sky were covered with cumulus clouds. Before 6 UTC mainly cirrus fibratus clouds were observed and after 19 UTC the sky was cloudless. Since most of the time shallow cumulus clouds were observed on that day, it is chosen for the evaluation of MUDIS performance during broken cloud conditions. On 16 July the sky was covered between sunrise and sunset with two-eighths to eight-eighths cirrus fibratus clouds and sporadic cumulus humilis clouds. No cloudless day occurred during the comparison campaign, therefore that day was chosen instead. This is also based on results of

	12.07.	13.07.	14.07.	15.07.	16.07.	17.07.	18.07.	19.07.
MUDIS	5117	5111	5098	5089	5080	5068	5054	5041
SCCD	75	76	80	76	77	78	76	77
NDACC	26	39	39	38	38	38	38	38
HSI	195	194	194	193	193	192	192	192
Clouds	Sc	Sc	St	Cu	Ci	Ci,Ac	Cu	Cu
Cloud cover	4/8	7/8	8/8	2/8	6/8	7/8	6/8	5/8
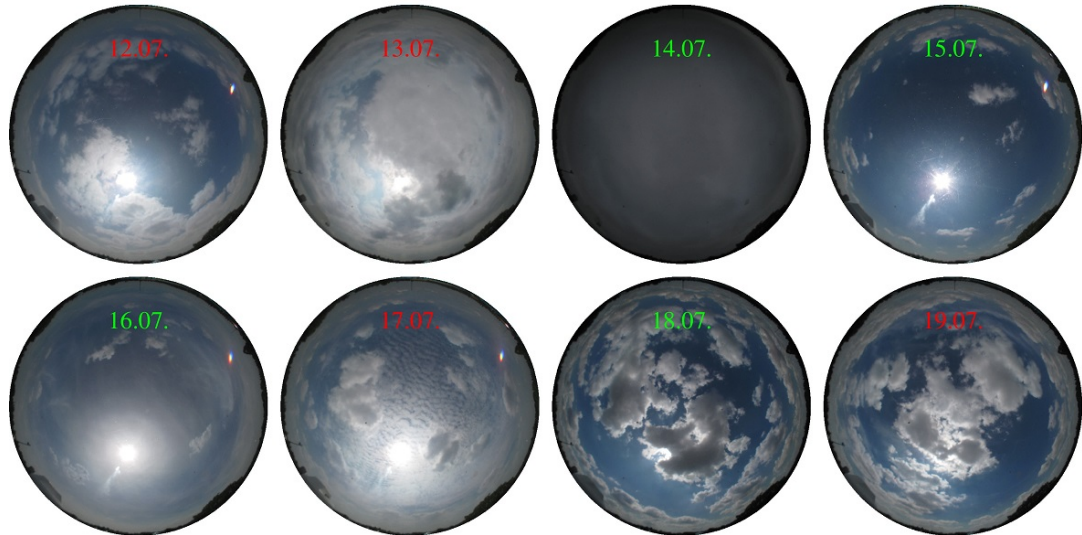
Table 5.2: Number of measurements per day performed with MUDIS, SCCD, NDACC and HSI in July 2013. The numbers in line with the instruments note the measurements performed per day from sunrise to sunset. The allsky pictures captured with the HSI show the weather conditions at 11 UTC on the evaluation days (green) and days used for intercalibration (red). Cloud legend: Stratocumulus (Sc), cirrus (Ci), stratus (St), cumulus (Cu), altocumulus (Ac).

the October 2012 campaign which showed that a cirrus fibratus covered sky comes closest to a cloudless sky in terms of variation of sky radiance (see Figure 4.6). On 18 July the sky was partially covered with two-eighths to seven-eighths by low cumulus clouds until 18 UTC and cloudless after 18 UTC. This day is chosen for the evaluation due to its similar broken cloud coverage compared to the 15 July. The evaluation of the measurements performed on the four days chosen for the instrument comparison are presented in Section 5.2.

5.2 Results

Analogous to Section 4.2 the radiance measurements performed with MUDIS and SCCD on 14, 15, 16 and 18 July 2013 are compared in this section. First of all, the influence of the shading unit mounted to the MUDIS entrance optics dome is examined in Section 5.2.1. Spectral zenith radiance measurements of MUDIS, SCCD and the NDACC instrument are evaluated in Section 5.2.2. In Section 5.2.3 a statistical approach for the examination of the overall performance of all directions measured by MUDIS and SCCD is presented and Section 5.2.4 provides a comparison of spatial sky radiance variations measured with MUDIS and SCCD. In addition, spectral actinic irradiance (Section 5.2.5) is calculated from measurements of both instruments and intercompared in order to check the validity of spatially integrated values.
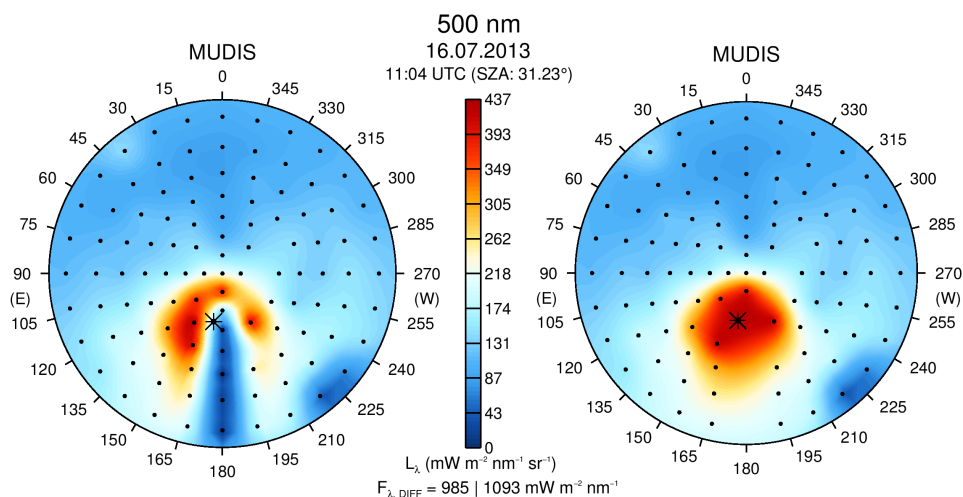
Figure 5.1: MUDIS sky radiance measurement, performed at 11:04 UTC on 16 July. On the left hand side measurement points between circumsolar region and the horizon are shaded by the shadow band. On the right side the shaded points have been removed and the region in between is filled by values determined by kriging interpolation.

5.2.1 Influence of the Shading Unit

For the measurement campaign performed in July 2013 the shading unit described in Section 3.2.3 was equipped to the MUDIS entrance optics dome. Depending on the position of the sun, various fibers of the entrance optics dome are temporally shaded by the shadow band. When calculating spatially integrated radiometric quantities, for example the actinic irradiance, these measurement points need to be identified and removed from the MUDIS datasets. An example is illustrated in Figure 5.1, where a MUDIS sky radiance measurement performed during direct sunlight at 11:04 UTC on 16 July is shown. In the left polar plot the points shaded by the shadow band are clearly recognizable between the circumsolar region and the horizon. A simple approach is used in order to remove these points during this comparison campaign: Each ratio of MUDIS/SCCD sky radiance measurements below 0.7 in a 45° region around the solar azimuth angle is discarded as a point shaded by the shadow band. In the right plot the shaded points are removed and the region in between is filled by values determined through kriging interpolation. The corrected MUDIS actinic irradiance is about 10% higher than the uncorrected actinic irradiance and agrees well with the actinic irradiance calculated from SCCD measurements (Section 5.2.5, Figure 5.13). However, a technique to calculate the exact position of the shadow band has to be developed in the future in order to remove shaded points without the aid of SCCD measurements.

5.2.2 Spectral Zenith Radiance

Spectral zenith radiance measurements performed with MUDIS, SCCD and the NDACC instrument are presented in this section. Due to the spatial scanning character of the SCCD and the wavelength scanning character of the NDACC instrument the zenith direction is measured too infrequently and asynchronously for a direct comparison of all three instruments. Therefore MUDIS measurements are compared consecutively with the SCCD and NDACC measurements.

Figure 5.2: Spectral radiance measured in the zenith of the sky with MUDIS and SCCD on 14, 15, 16 and 18 July. A median filter is applied to the ratios displayed in the bottom plots; the underlying grey lines show the unfiltered data.

Comparison of MUDIS and SCCD Zenith Radiance Measurements

In Figure 5.2 four pairs of MUDIS and SCCD measurements captured around 11 UTC at 14, 15, 16 and 18 July are shown. For overcast conditions on 14 July the difference between MUDIS and SCCD is less than 4% between 310 and 600 nm. Under broken cloud conditions at 11 UTC on 15 July the difference between both instruments is less than 5% between 310 and 600 nm. For a cirrus fibratus covered zenith at 11 UTC on 16 July the difference between MUDIS and SCCD is less than 7% between 310 and 600 nm. During broken cloud coverage at 11 UTC on 18 July the difference is up to 10%. In order to check if the observed spectral variations are random or systematic deviations, the diurnal variation is examined in the following at two exemplary wavelengths (320 nm and 500 nm).

Figure 5.3 shows the diurnal variation of radiance measured in the zenith direction with MUDIS and SCCD at 320 and 500 nm. During overcast sky on 14 July the ratios of zenith radiance measured with MUDIS and SCCD show a bias of -3.7% and a 1σ standard deviation of 5.5% at 320 nm. At 500 nm a bias of 0.9% and a 1σ standard deviation of 2.7% is observed. During the mornings of 15, 16 and 18 July a significantly higher deviation of 15%–20% is observed at 500 nm compared to the afternoon of the same days. In fact, the shape of the bias is similar on these days, with a high MUDIS bias in the morning and a low or zero bias in the afternoon. This systematic diurnal variation may be the result of a tilted viewing direction of this particular MUDIS fiber. During overcast sky on 14 July the systematic difference is not apparent, which is consistent with the parameter studies performed in Section 6.4. The lower diurnal variation of the systematic difference at 320 nm can be explained by the lower influence of tilted viewing angles with shorter wavelengths due to the lower anisotropy of sky radiance in the UV part of the spectrum and due to a wavelength dependence of the tilt for the MUDIS zenith channel (see Figure 3.17).
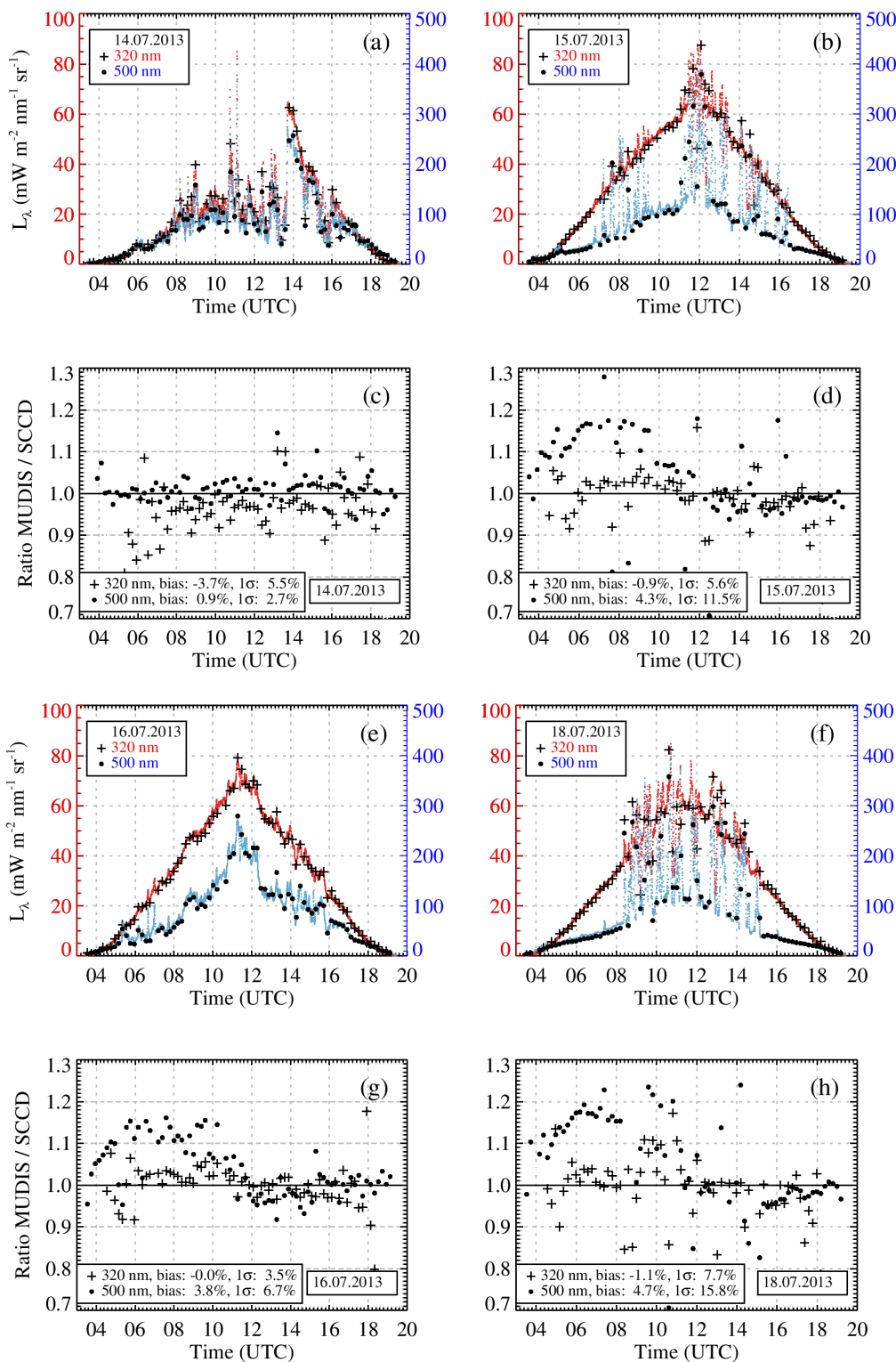
Figure 5.3: Diurnal variation of the spectral zenith radiance measured with MUDIS and SCCD on 14, 15, 16 and 18 July. In plot (a), (b), (e) and (f) absolute values of SCCD at 320 nm (crosses) and 500 nm (dots) are shown. In addition, MUDIS data at 320 nm (red line) and at 500 nm (blue line) is shown. In plot (c), (d), (g) and (h) the ratios of synchronized MUDIS and SCCD measurements at 320 nm and 500 nm are shown.
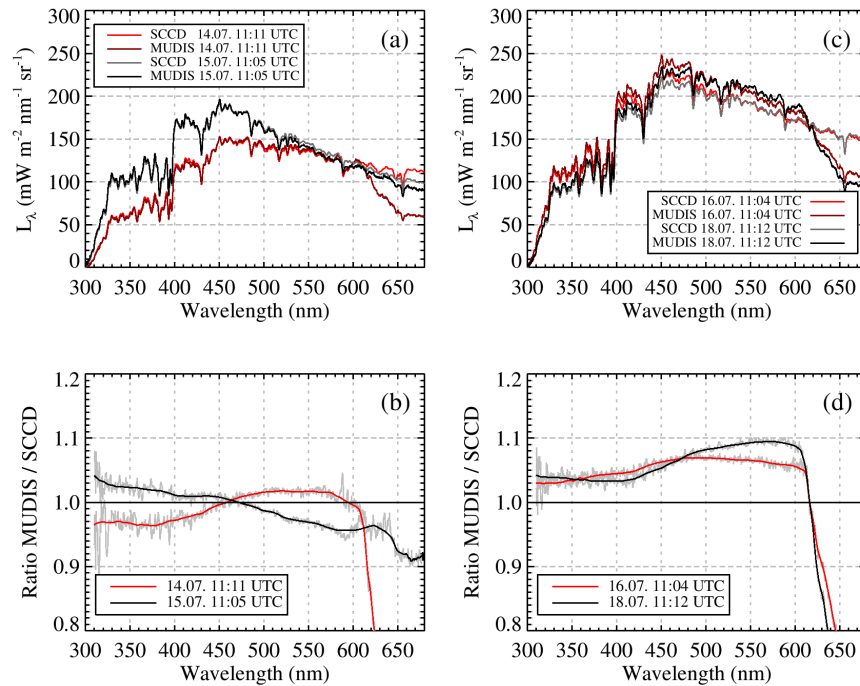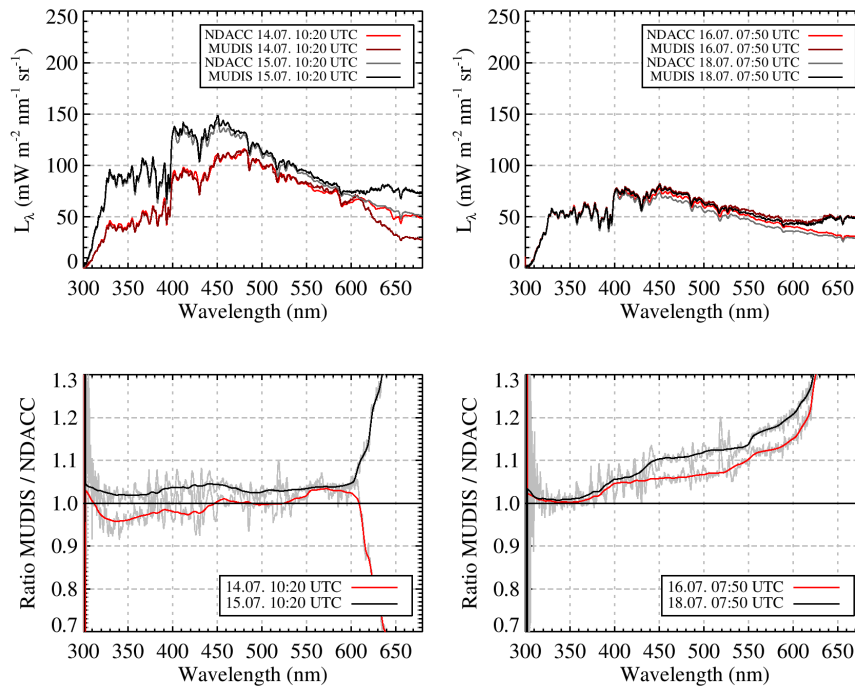
Figure 5.4: Spectral radiance measured in the zenith of the sky with MUDIS and NDACC instrument on 14, 15, 16 and 18 July. A median filter is applied to the ratios displayed in the bottom plots; the underlying grey lines show the unfiltered data.

Comparison of MUDIS and NDACC Zenith Radiance Measurements

In Figure 5.4 four pairs of synchronous MUDIS and NDACC instrument measurements, performed around 10:20 UTC on 14 and 15 July (top left) and around 07:50 UTC on 16 and 18 July (top right) and their ratios (bottom), are shown. The NDACC instrument scans the measured spectra over a time span of 21 min each. Therefore, the four chosen spectra were measured during time spans with little variations of the zenith direction of the sky. On 14 July at 10:20 UTC the zenith was covered with stratus clouds, while the zenith was cloudless on 15 July at 10:20 UTC. The difference between MUDIS and SCCD measured on both days is less than 5% between 310 and 600 nm. For a cirrus fibratus covered zenith at 07:50 UTC on 16 July and a cloudless zenith at 07:50 UTC on 18 July the difference between MUDIS and the NDACC instrument is less than 5% between 310 and 400 nm but exceeds 20% for the wavelength region between 400 and 600 nm. The steep increase of the ratio is assumed to be linked to the tilt of the MUDIS zenith channel. The ratios displayed are also more noisy compared to the MUDIS/SCCD spectral comparisons, since the intercalibration process applied to MUDIS compensates MUDIS/SCCD bandwidth and wavelength shift differences, while those differences between MUDIS and the NDACC instrument are not corrected by the intercalibration.

Figure 5.5 shows the diurnal variation of radiance measured in the zenith direction with MUDIS and the NDACC instrument at 320 and 500 nm. During overcast sky on 14 July the ratios of zenith radiance measured with MUDIS and SCCD show a bias of up to -3.4% and a 1σ standard deviation of less than 2.4% at 320 and 500 nm. Again, a significant diurnal change of the bias is observed for the 15, 16 and 18 July at 500 nm. For days with cirrus fibratus covered sky and broken cloud conditions the bias at 320 nm is up to -2.5% with a standard deviation of up to 9.4%.
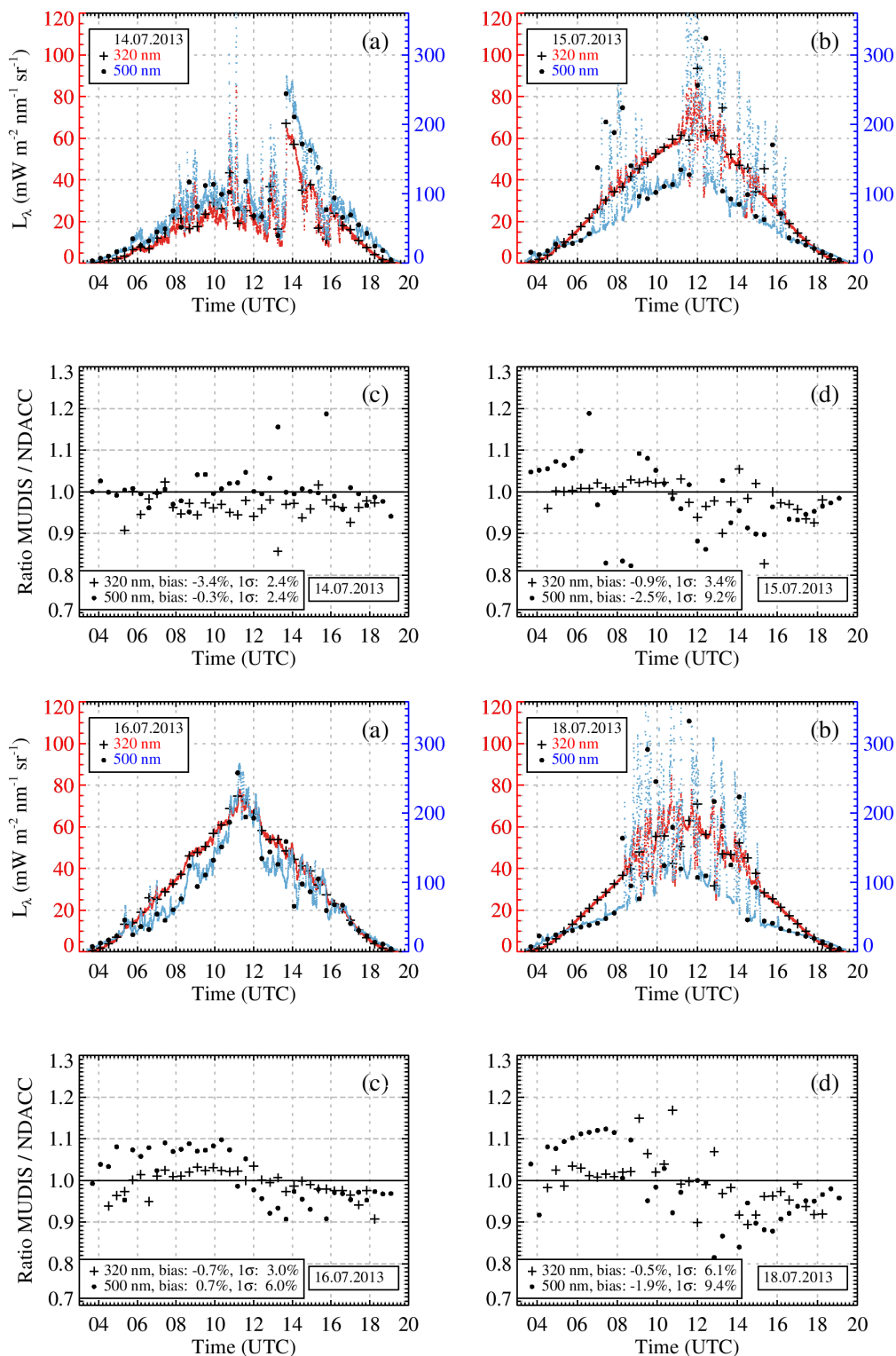
Figure 5.5: Diurnal variation of the spectral zenith radiance measured with MUDIS and the NDACC instrument on 14, 15, 16 and 18 July. In plot (a), (b), (e) and (f) absolute values of SCCD at 320 nm (crosses) and 500 nm (dots) are shown. In addition, MUDIS data at 320 nm (red line) and at 500 nm (blue line) is shown. In plot (c), (d), (g) and (h) the ratios of synchronized MUDIS and the NDACC instrument measurements at 320 nm and 500 nm are shown.

5.2.3 Statistical Evaluation of MUDIS Sky Radiance Measurements

Analogous to Section 4.2.3 the MUDIS/SCCD spectral sky radiance ratios are calculated for each measured direction in order to quantify the variation of the radiance measurements. All measurements performed from sunrise to sunset are therefore combined into an individual dataset for each particular measurement day. MUDIS data points that are either compromised by broken fibers, have spectral radiance of less than the SCCD detection threshold (<3 $mWm^{-2}nm^{-1}sr^{-1}$) and are shaded by the shadow band are excluded from the dataset. Outliers greater than four standard deviations (4σ) which originate mostly from obstacles at the horizon are also removed from the dataset. An overview over all excluded points is given in Table 5.3. Broken fibers reduce the dataset by a constant amount of 3.5% and less than 2.6% of the measurements are rejected as outliers. The fraction of points rejected due to the SCCD detection threshold is lower since shortwave radiance at lower solar zenith angles is higher in July compared to October. During overcast conditions on 14 July up to 24.8% of the measurements were discarded due to a signal value below the SCCD detection threshold. For campaign days with a cumulus and cirrus fibratus covered sky (15, 16 and 18 July), the amount of rejected datapoints from sunrise to sunset is less than 13.7%. The shading unit effectively prevented oversaturation and therefore no more measurements were discarded due to stray light. Measurements that are rejected in the circumsolar region and are shaded by the shadow band contribute less than 3.6% to the rejected points. In total between 68.6% and 78.6% of all ratios calculated from measurements between sunrise and sunset are used for the statistical evaluation at 320 nm. At 500 nm less than 6.7% of the ratios are discarded due to a signal below the SCCD detection threshold, therefore more ratios are used for the evaluation. On 15, 16 and 18 July only 0.5% of the ratios are discarded due to noise at 500 nm.

The remaining dataset of MUDIS/SCCD ratios is displayed in form of histograms at 320 and 500 nm for each of the four campaign days in Figure 5.6. On 14 July the sky was overcast with stratocumulus clouds. For this day the bias between MUDIS and SCCD sky radiance is 0.3% with a 1σ standard deviation of 9.5% at 320 nm and 0.1% with a 1σ standard deviation of 6.4% at 500 nm. For broken cloud conditions on 15 July the bias is -0.6% with a 1σ standard deviation of 6.6% at 320 nm and 0.1% with a 1σ standard deviation of 8.7% at 500 nm. For cirrus fibratus covered sky on 16 July the bias is $<0.1\%$ with a 1σ standard deviation of 4.8% at 320 nm and -0.3% with a 1σ standard deviation of 6.1% at 500 nm. For broken cloud coverage on 18 July the bias is -0.5% with a 1σ standard deviation of 6.7% at 320 nm and 0.1% with a 1σ standard deviation of 9.2% at 500 nm.

	14 July	15 July	16 July	18 July
Total points	8927 (100%)	8475 (100%)	8588 (100%)	8475 (100%)
Broken fibers	316 (3.5%)	300 (3.5%)	304 (3.5%)	300 (3.5%)
Detection threshold	2210 (24.8%)	1157 (13.7%)	1177 (13.7%)	1147 (13.5%)
Stray light	0 (0.0%)	0 (0.0%)	0 (0%)	0 (0%)
Shading unit	212 (2.4%)	306 (3.6%)	304 (3.5%)	303 (3.6%)
4σ outliers	71 (0.8%)	125 (1.5%)	224 (2.6%)	164 (1.8%)
Total rejected	2809 (31.5%)	1888 (22.3%)	2009 (23.4%)	1914 (22.6%)
Total accepted	**6189 (69.3%)**	**6712 (79.2%)**	**6803 (79.2%)**	**6725 (79.4%)**

Table 5.3: MUDIS measurement points that are rejected for the statistical comparison of MUDIS and SCCD at 320 nm, discussed in Section 5.2.3.
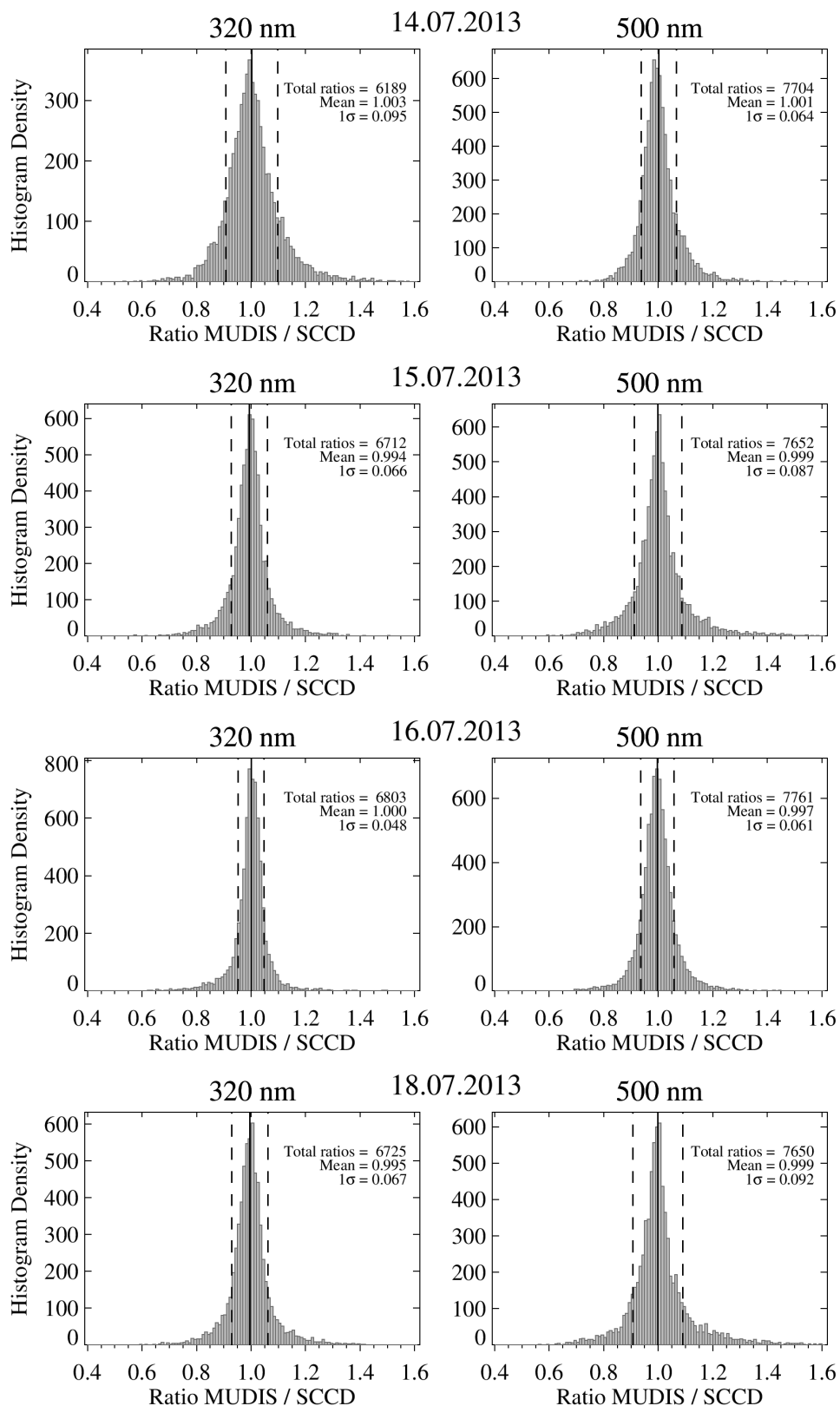
Figure 5.6: Histograms of MUDIS/SCCD sky radiance ratios at 320 and 500 nm for 14, 15, 16 and 18 July. The vertical dashed lines represent the corresponding standard deviations, the vertical solid lines the mean of all examined ratios.

The wavelength-dependence of the bias and the 1σ standard deviation calculated from the dataset of MUDIS/SCCD sky radiance ratios of the four campaign days are shown in Figure 5.7. The bias between 310 and 600 nm is less than 3% for all measurement days. Analogous to the first measurement campaign the bias of all measurement days increases rapidly for wavelengths longer than 600 nm due to limitations of the applied stray light correction method (Section 3.2.8).

On 16 July the smallest 1σ standard deviation, calculated from all MUDIS/SCCD ratios, is observed at 330 nm. It is increasing from 4% at 330 nm to 8% at 600 nm, again showing the typical wavelength dependence on cloudless days. The variation of sky radiance on 15 and 18 July is higher due to cumulus clouds, therefore the standard deviation increases from 5% at 330 nm up to 13% at 600 nm. On the overcast 14 July a standard deviation of less than 8% between 330 and 600 nm, increasing rapidly to about 20% at 310 nm, is observed.
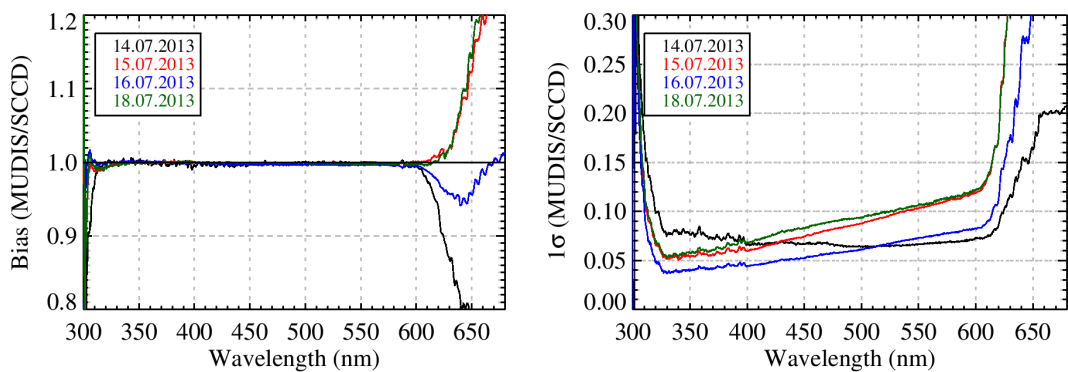
Figure 5.7: Wavelength dependence of the bias (left) and the 1σ standard deviation (right), calculated from MUDIS/SCCD spectral sky radiance ratios for 14, 15, 16 and 18 July.
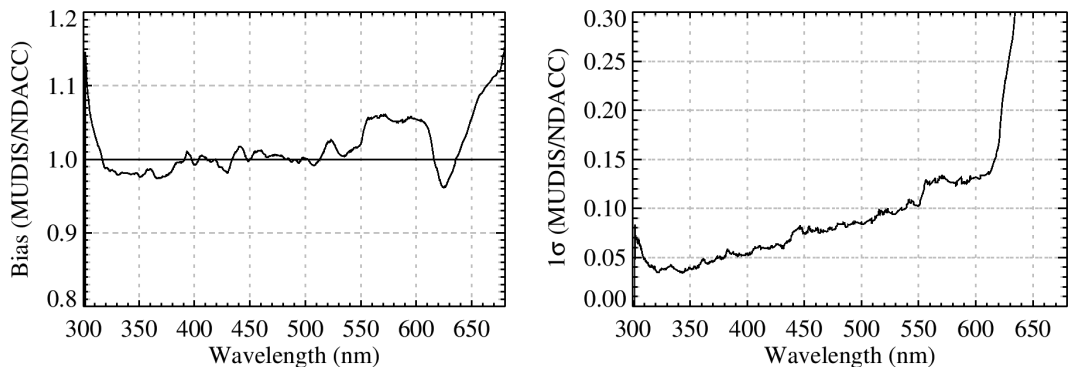
Figure 5.8: Wavelength dependence of the bias (left) and the 1σ standard deviation (right), calculated from all MUDIS/NDACC instrument spectral zenith radiance ratios of the eight comparison campaign days from 12 to 19 July.

In addition, the wavelength dependence of the bias and the 1σ standard deviation has been calculated for the MUDIS/NDACC instrument zenith radiance ratios. Since only very few datapairs are available, the calculation has been performed based on all eight measurement days of the campaign. In Figure 5.8 the results of that calculation are shown. The systematic difference between MUDIS and the NDACC instrument is less than 6% and the 1σ standard deviation ranges between 4% and 13% for the wavelength region 310–600 nm.

5.2.4 Spatial Distribution of Sky Radiance

Figure 5.9 shows sky radiance as a function of zenith and azimuth angle, measured with MUDIS and SCCD at around 11:04 UTC on 16 July. During the measurement process, cirrus fibratus clouds covered the sky. The two representative wavelengths 320 and 500 nm are shown as sky maps. The numbers in the MUDIS sky maps represent the difference between each particular pattern point in percent. Compared to the October campaign the amount of missing points at 11 UTC is reduced from 23 to 11. Since no more points have to be removed due to stray light and the influence of direct radiation, only 4 points were removed due to damaged fibers and 7 points were removed due to being obscured by the shading unit. The observed sky radiance as a function of zenith and azimuth angle of both instruments agrees well for both examined wavelengths. Compared to a cloudless sky the cirrus fibratus covered sky does not show the sky radiance minimum opposite to the sun, since Mie scattering covers up the minimum. Figure 5.10 shows the spectral sky radiance distribution of a sky covered with stratocumulus clouds at 320 and 500 nm measured with MUDIS and SCCD at 11:11 UTC on 14 July, analogous to Figure 5.9. The MUDIS shading unit covers fractions of the sky which are covered with bright clouds, thus resulting in an underestimate of actinic irradiance compared to the SCCD measurements. In Figure 5.11 sky radiance measurements during six-eighths broken cloud coverage at 11:11 UTC on 18 July are shown. Again, the MUDIS actinic irradiance is underestimated compared to the SCCD measurements due to the shading unit as explained before.

An interesting detail that all shown sky maps have in common is the small difference between MUDIS and SCCD measurement directions near to the horizon (84° zenith viewing angle). Since the FOV of MUDIS is up to 17° wide compared to the 5° FOV of SCCD, the MUDIS channels at an 84° zenith viewing angle will partially measure radiance originating from obstacles at the horizon or even the ground. Nevertheless, no significant difference between MUDIS and SCCD is observed for those points. It is assumed that the bias caused by FOV differences of viewing directions is compensated by the intercalibration of MUDIS based on SCCD measurements. This assumption is further examined in Section 6.2.
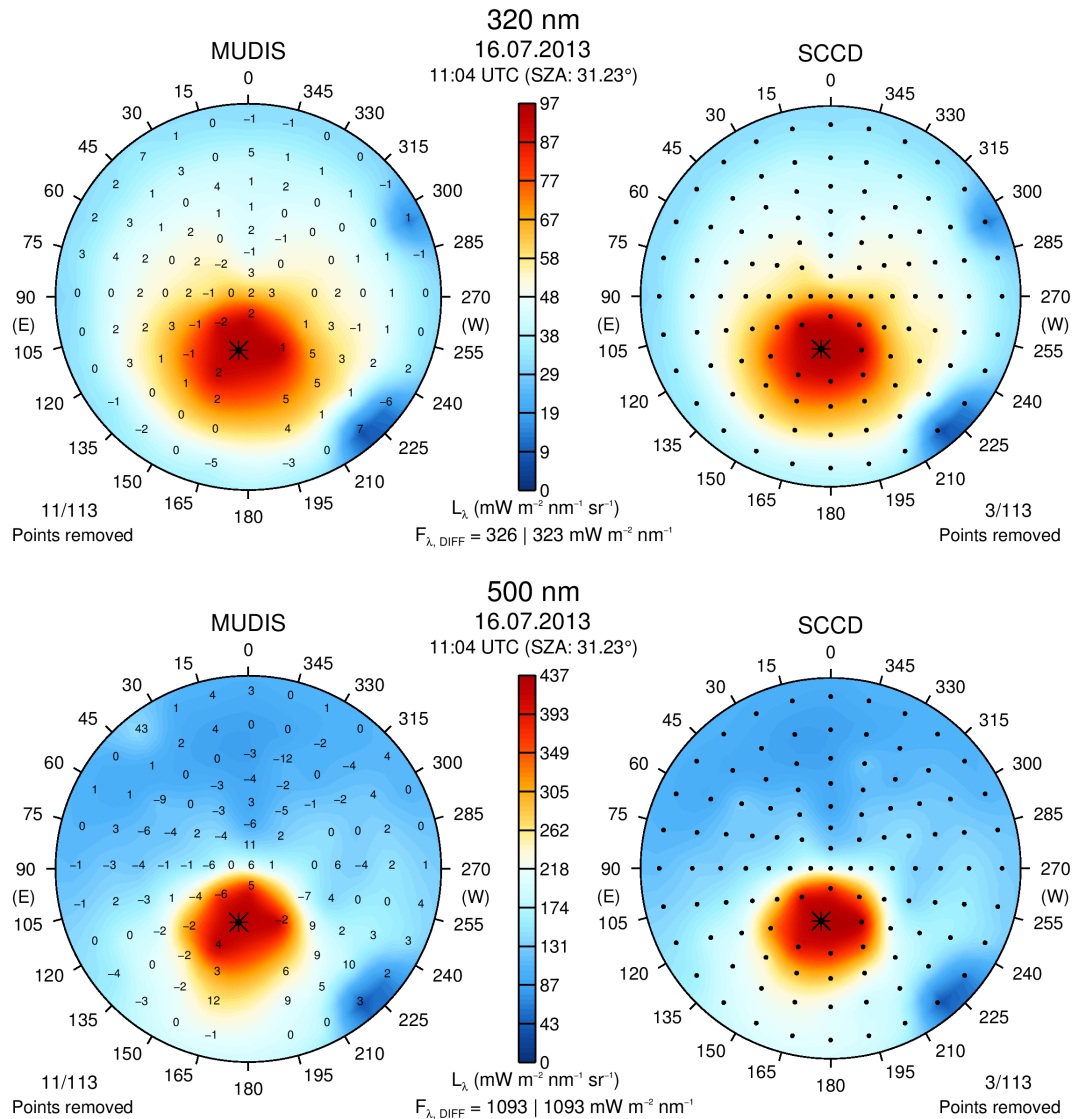
Figure 5.9: Spatial distribution of sky radiance at 320 (top) and 500 nm (bottom) measured during cirrus fibratus covered sky on 16 July with MUDIS (left) and SCCD (right). The numbers in the MUDIS sky maps represent the percent difference between MUDIS and the corresponding SCCD measurement.
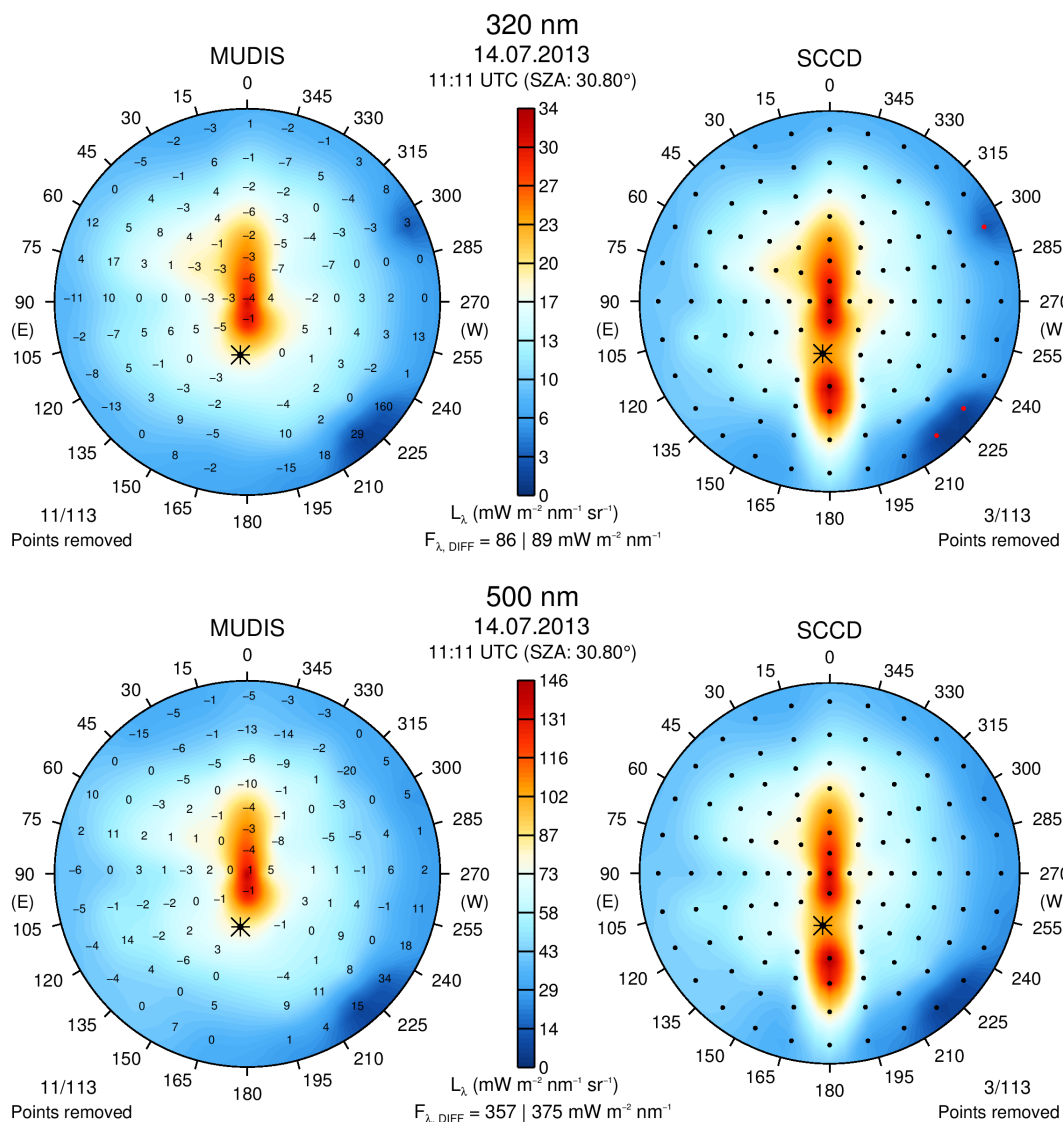
Figure 5.10: Spatial distribution of sky radiance at 320 (top) and 500 nm (bottom) measured under overcast sky on 14 July with MUDIS (left) and SCCD (right). The numbers in the MUDIS sky maps represent the difference between each particular pattern point in percent.
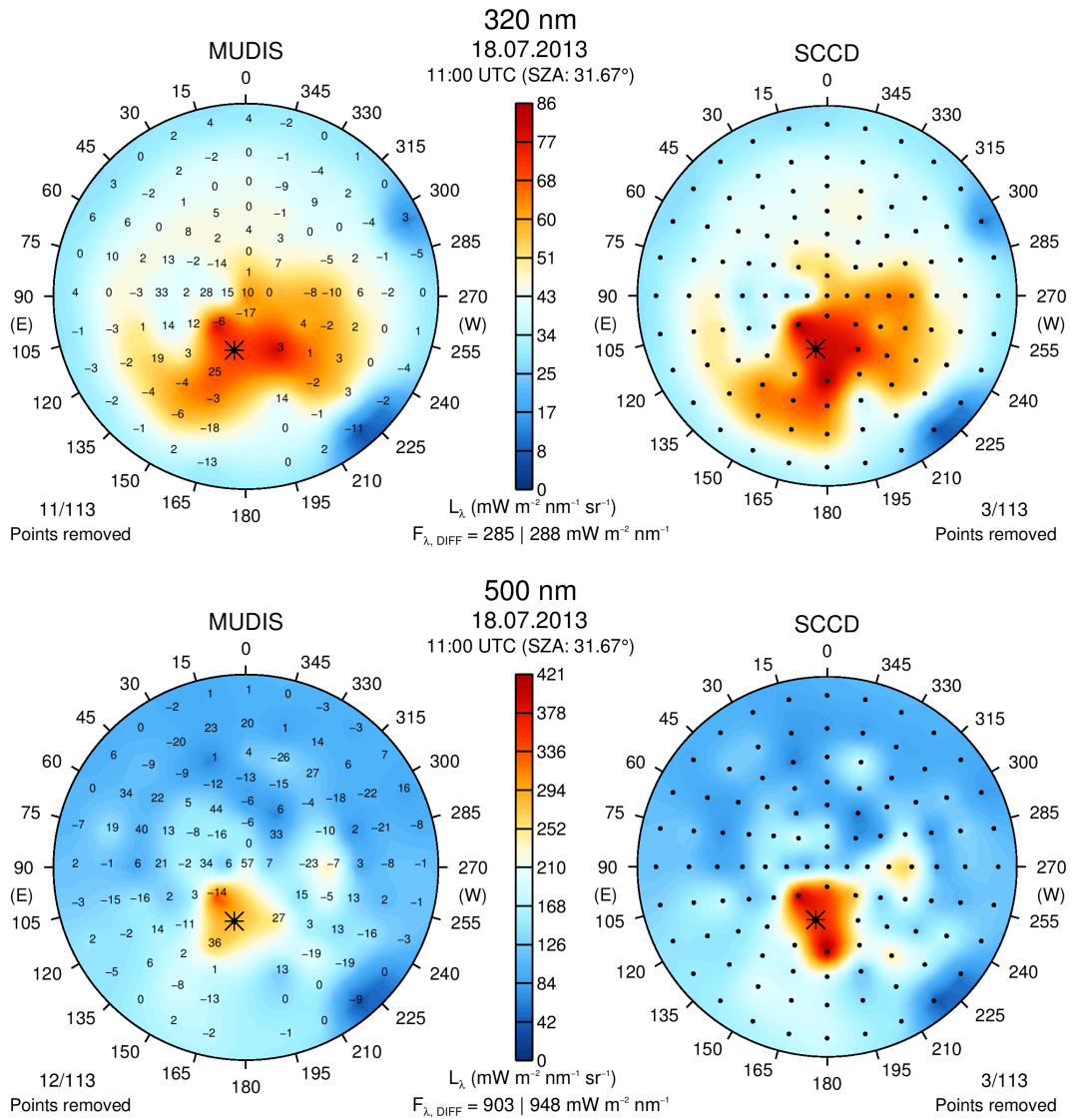
Figure 5.11: Spatial distribution of sky radiance at 320 (top) and 500 nm (bottom) measured during cloudy sky on 18 July with MUDIS (left) and SCCD (right). The numbers in the MUDIS sky maps represent the percent difference between MUDIS and the corresponding SCCD measurement.

5.2.5 Spectral Actinic Irradiance

Analogous to Section 4.2.5, the measured spectral sky radiance is integrated over the hemisphere in order to derive the spectral diffuse downward actinic irradiance. Figure 5.13 shows the ratio of the spectral actinic irradiance measured with MUDIS and SCCD on 14, 15, 16 and 18 July 2013 at about 11 UTC. During overcast sky conditions on 14 July the actinic irradiance measured with both instruments differs by 5% between 310 and 600 nm. The difference is explained by the influence of the shading unit, visible in Figure 5.10. The highest sky radiance observed by the SCCD appears in southern direction, these points are obscured by the shading unit in the MUDIS field of view. For two-eighths broken cloud conditions on 15 July the difference is less than 1% between 310 and 600 nm, showing a good agreement. For cirrus fibratus covered sky on 16 July the deviation is also low with less than 2%. For six-eighths broken cloud conditions on 18 July a higher deviation of up to 6% is observed. The sky map displayed in Figure 5.11 shows that the shading unit is again responsible for the observed underestimate, since it is covering a bright patch of cloud in the circumsolar region. The missing points are interpolated from adjacent cloudless viewing angles, resulting in the increase of variation with longer wavelengths.

The diurnal variation of the actinic irradiance at 320 and 500 nm during the four measurement days is shown in Figure 5.13. Measurements of spectral actinic irradiance smaller than $10 \, \mathrm{mWm^{-2}nm^{-1}sr^{-1}}$, which occur at sunrise and sunset, are not taken into account. The bias of MUDIS/SCCD actinic irradiance ratios on 14, 15, 16 and 18 July varies between -1.7% and 0.1%. The 1σ standard deviation on all four days is less than 2.6%. Despite the broken cloud conditions and the interpolation of points distorted by the shading unit, the actinic irradiance calculated for both instruments agrees well.
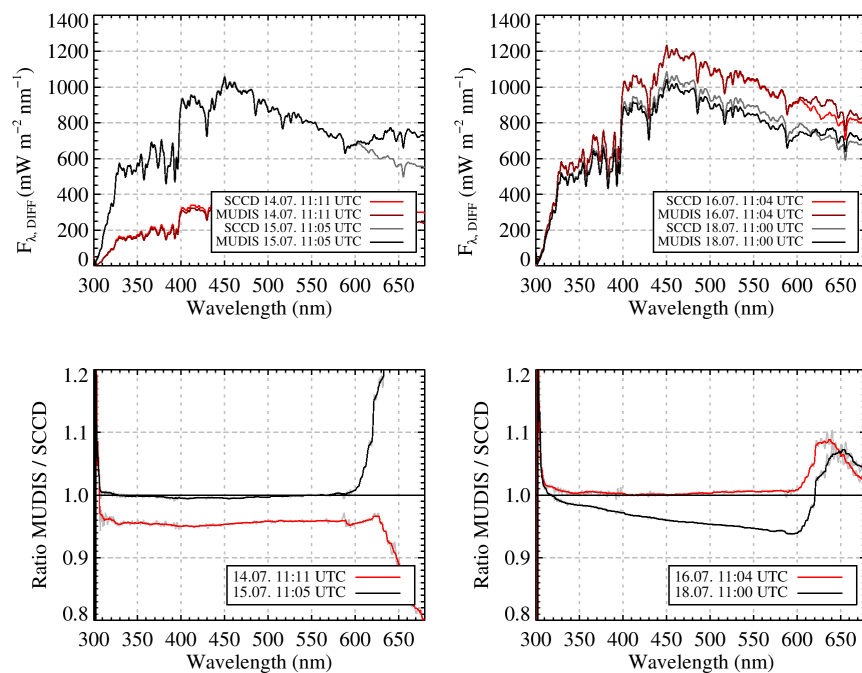
Figure 5.12: Spectral actinic irradiance measured with MUDIS and SCCD on 14, 15, 16 and 18 July. A median filter is applied to the ratios displayed in the bottom plots; the grey lines show the unfiltered data.
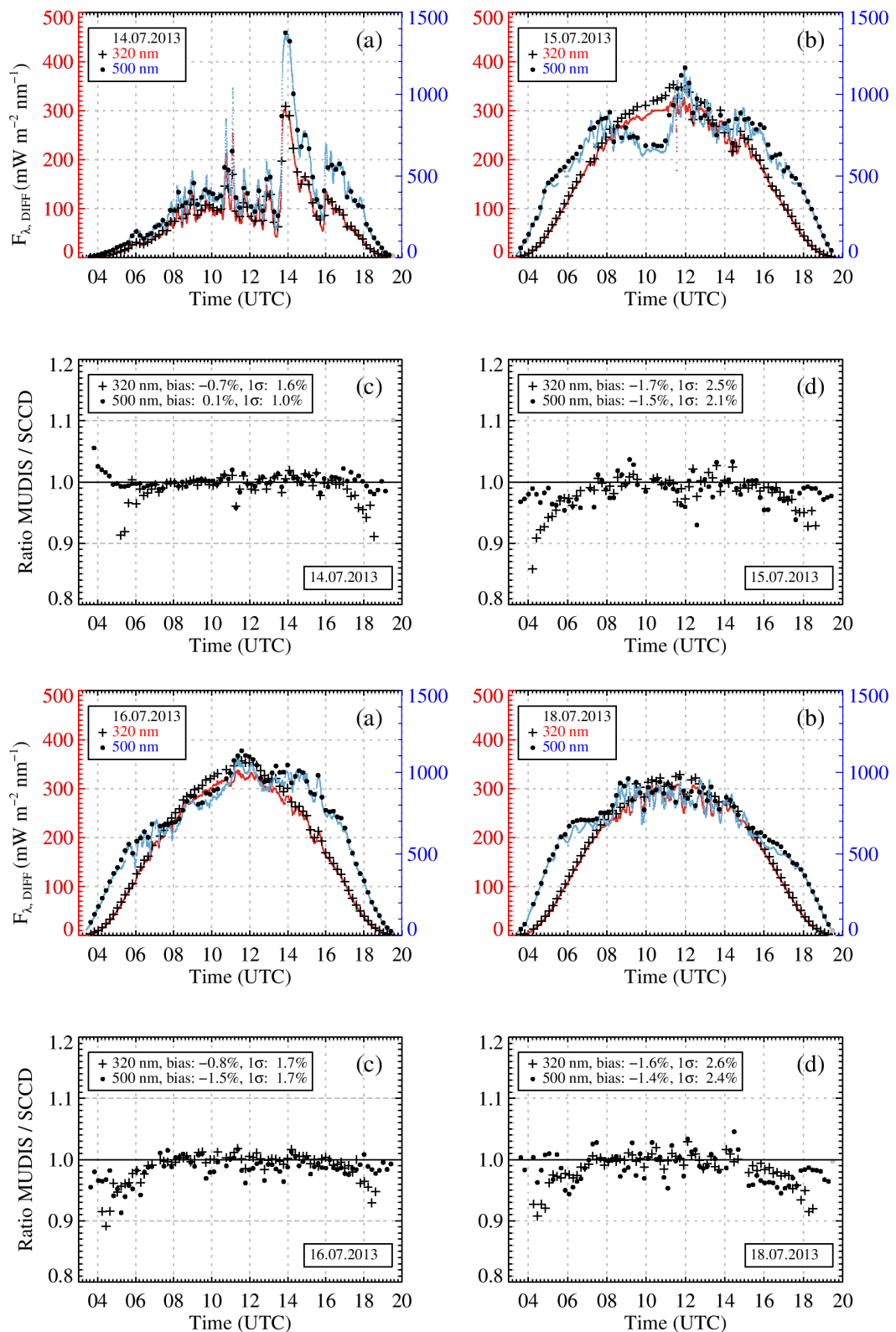
Figure 5.13: Diurnal variation of the actinic irradiance measured with MUDIS and SCCD on 14, 15, 16 and 18 July. In plot (a), (b), (e) and (f) absolute values of SCCD at 320 nm (crosses) and 500 nm (dots) are shown. In addition, MUDIS data at 320 nm (red line) and at 500 nm (blue line) is shown. In plot (c), (d), (g) and (h) the ratios of synchronized MUDIS and SCCD measurements at 320 nm and 500 nm are shown.

5.3 Campaign Summary and Discussion

The second instrument comparison campaign with the MUDIS instrument has been conducted in July 2013. Synchronous sky radiance measurements were performed with MUDIS and SCCD on eight days. In addition, zenith radiance measurements were performed with the NDACC instrument. Four days of measurements (12, 13, 17 and 19 July) were used for the intercalibration of MUDIS and the measurements of the remaining four days were used for evaluation, since they provided different meteorological conditions: On 14 July the sky was covered with stratocumulus clouds, on 15 and 18 July the sky was mostly covered with cumulus clouds and on 16 July the sky was covered with cirrus fibratus clouds. The difference between MUDIS and SCCD measurements of the spectral zenith radiance performed at about 11 UTC on the four campaign days is less than 10% in the wavelength region between 310 and 600 nm. The bias of the diurnal MUDIS/SCCD ratios is less than 4% at 320 nm with a 1σ standard deviation of less than 7.7%. However, a diurnal variation of the bias between zenith radiance of MUDIS and SCCD is observed, increasing with longer wavelengths. It is assumed that this is linked to a tilted viewing angle of the MUDIS entrance optics zenith point or a distortion of the measuring direction by a dust particle on the fiber end.

Spectral zenith radiance measured with MUDIS and the NDACC instrument varies in the wavelength range between 310 and 600 nm by less than 5% around noon. Like the comparison between MUDIS and SCCD a difference of up to 20% at longer wavelengths is observed in the morning for comparisons between MUDIS and the NDACC instrument. This supports the assumption, that a tilted viewing angle of the zenith channel of MUDIS is causing this deviation. At 320 nm the bias lies in between -3.4% and -0.5% with a 1σ standard deviation of less than 6.1%.

A statistical evaluation of MUDIS/SCCD ratios of all viewing directions has been performed for each day of the campaign. The mean bias of all MUDIS/SCCD sky radiance ratios between 310 and 600 nm is less than 3% for all four evaluated campaign days. In the wavelength range between 330 and 340 nm the day with cirrus fibratus covered sky shows the lowest 1σ standard deviation with 4%–5%, followed by days with broken cloud coverage (5%–7%) and the day with overcast sky conditions (7%–8%). Again, an increase of the 1σ standard deviation of up to 13% with longer wavelengths is observed for all non-overcast days. The mean systematic difference calculated from eight days of MUDIS/NDACC zenith radiance ratios is less than 6% between 310 and 600 nm with a 1σ standard deviation of 4%-13% between 310 and 600 nm.

The spatial distribution of sky radiance at 320 and 500 nm is investigated at around 11 UTC for an overcast sky on 14 July, a cirrus fibratus covered sky on 16 July and a sky covered with six-eighths cumulus clouds on 18 July. Especially under partially cloudy conditions the points obscured by the shading unit may lead to differences in actinic irradiance calculated from sky radiance measurements of MUDIS and SCCD. Nevertheless, the bias and standard deviation derived from actinic irradiance measurements performed with MUDIS and SCCD are less than 3% for all four intercomparison days.

Comparable to the first campaign, the reliability of MUDIS decreases rapidly for wavelengths longer than approx. 600 nm due to the influence of second order stray light, rendering the wavelength region between 600 and 680 nm useless. While the bias between MUDIS and SCCD in this wavelength region was acceptable in the first campaign, it is comparably bad for broken cloud and overcast conditions during the second campaign, but shows a good agreement for cirrus fibratus covered sky. This can be explained by the influence of the applied intercalibration method. During the first campaign two of the four days used for the intercalibration process were overcast. During the four days which were used for the intercalibration of the second

campaign, the sky was most of the time covered with broken clouds and in addition cirrus fibratus clouds occurred on two of the four days. Therefore, the stray light induced deviation of the sensitivity and the stray light induced deviation of measurements under cirrus fibratus covered sky balance each other out. It is concluded that a more sophisticated stray light correction method has to be found, if reliable measurements in the wavelength region between 600 and 680 nm are desired.

6 Allsky-based Measurement Simulation Algorithm

The statistical comparisons of radiance measurements performed with MUDIS and SCCD presented in Sections 4.2.3 and 5.2.3 reveal characteristic standard deviations for different meteorological conditions. During cloudless or cirrus fibratus covered sky the observed standard deviation of MUDIS/SCCD radiance ratios increased with longer wavelengths. For overcast sky no wavelength dependence could be observed. It is assumed that a combination of instrument differences like measurement time asynchronism, FOV differences, unintended entrance optics tilt and the wavelength dependence of the temporal and spatial deviations of sky radiance causes the observed standard deviation of MUDIS/SCCD radiance ratios.

In order to quantify the influence of the mentioned uncertainties an algorithm has been developed which simulates the FOV and corresponding viewing directions of both instruments based on allsky pictures. The HSI provides allsky pictures of the sky with a spatial resolution of approx. $0.24°$. With this allsky-based measurement simulator (AMS) algorithm a spectroradiometer measurement is simulated by the following steps:

1. An allsky picture, captured at the time for which the measurement shall be simulated, is chosen (Figure 6.1(a)).

2. The picture is divided into its three color channels in order to derive a wavelength dependent information (Figure 6.1(b)).

3. A linearity correction is applied to each pixel of a chosen color channel (Figure 6.1(c)).

4. The pixels inside of the FOV of each measuring direction of the emulated spectroradiometer are located (Figure 6.1(d)).

5. The FOV pixels are weighted with the angular response of the instrument that shall be emulated (Figure 6.1(e)).

6. The mean count values of all pixels inside the FOV of each particular measuring direction are calculated (Figure 6.1(f)).

By performing these steps for two different instruments and varying one or more instrument parameters, the deviation between both instruments resulting from those differences can be examined. With this algorithm parameter studies of the following instrument differences can be conducted individually or combined:

- **FOV difference.** The variation of radiance measurements performed with the same viewing angle but with different entrance optics can be calculated by deriving ratios of the mean count values taken from two simulations with different FOVs. When using allsky pictures taken on the same measurement day like the MUDIS and SCCD measurements, a similar statistical evaluation like in Section 4.2.3 can be performed in order to derive the deviation resulting from the FOV difference under certain sky conditions.
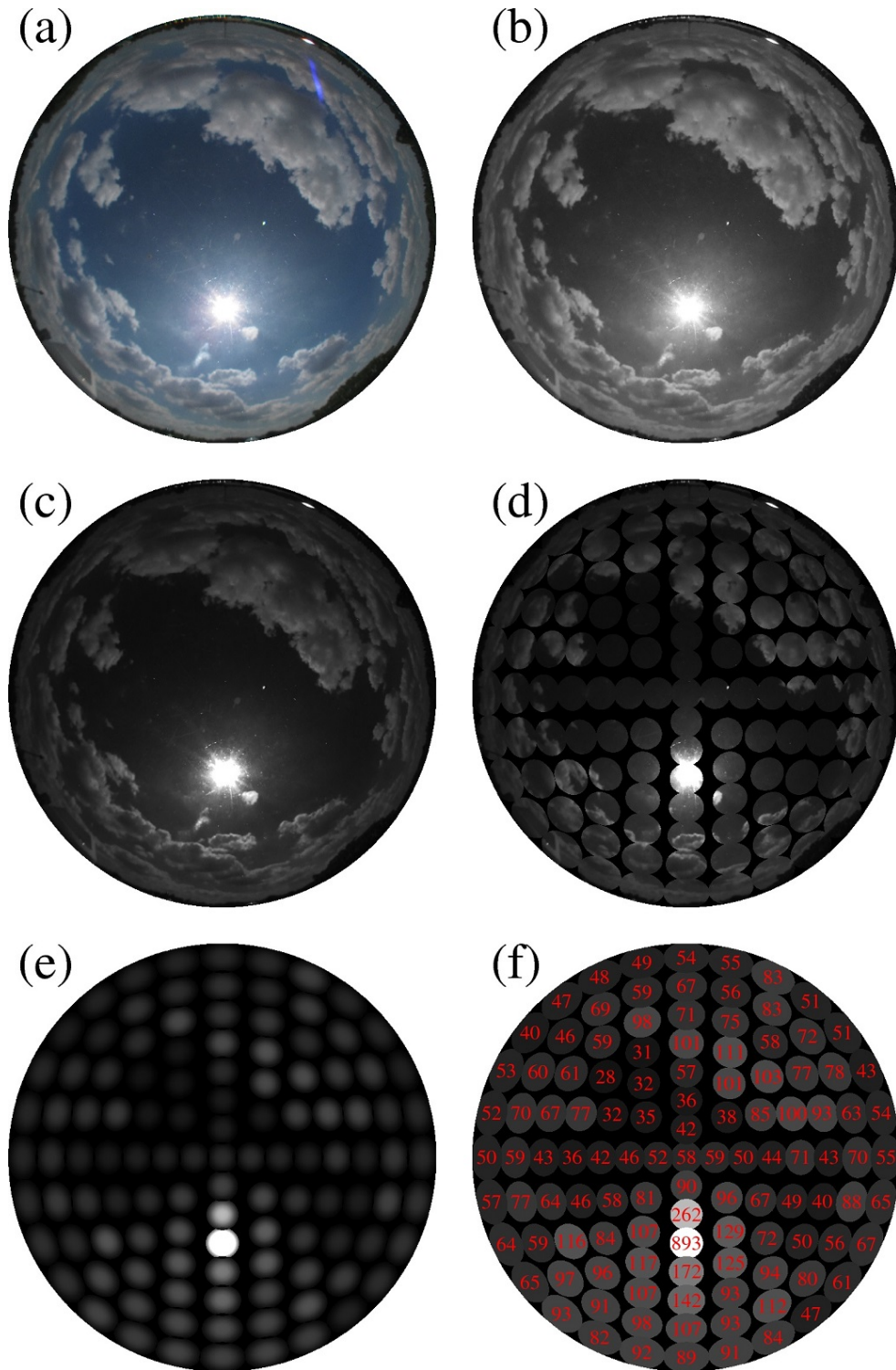
Figure 6.1: In (a) an allsky picture taken on 20 October 2012 at 11 UTC is shown. In (b) a single color channel is selected, in this case the red channel is chosen and displayed as a greyscale picture. The next step is the linearity correction of all pixels, displayed in (c). In (d) only pixels that are inside the FOV of the 113 MUDIS measuring directions are displayed and in (e) those pixels are additionally weighted with the angular response. The mean count values of all pixels inside the FOV of each particular measuring direction are calculated and displayed in (f).

- **FOV wavelength dependence.** The influence of the wavelength dependent FOV of MUDIS can be simulated by assigning different FOVs to the individual color channels during an instrument simulation. Since the allsky pictures consist of a red, green and blue channel they contain limited data about wavelength dependence of the examined instrument differences.

- **Intercalibration influence.** The relatively small systematic differences between MUDIS and SCCD observed near the horizon (e.g., Figure 5.9) are likely caused by a systematic compensation through the intercalibration. The intercalibration procedure can be emulated with the AMS algorithm in order to examine the observed behavior.

- **Unintended entrance optics tilt.** The fibers of the MUDIS entrance optics dome or the SCCD entrance optics might be tilted compared to their intended viewing directions. By altering the zenith and azimuth angles of a simulated sky radiance measurement point pattern and comparing it with its original viewing directions the influence of tilted fibers can be evaluated.

- **Pattern distribution.** By applying different point distribution patterns with varying numbers of measurement points, the influence of the chosen pattern on the sky radiance measurements can be investigated.

- **Time asynchronism.** When allsky pictures are taken with a sufficient high temporal resolution it is also possible to calculate the derivation caused by time asynchronism.

- **Variability of sky radiance.** The sky radiance measured with an instrument is the mean sky radiance inside its entrance optics FOV, which is weighted with the angular response of the entrance optics. Therefore, higher FOVs will smooth the temporal variations of the measured sky radiance. By comparing the temporal variation of simulations with different FOVs the influence on the detected variation can be examined.

On the downside the method is not capable to evaluate the performance of entrance optics in the circumsolar region, since the dynamic range of the HSI is too low for this purpose and pictures oversaturate in this region. In the following section the influence of the uncertainties mentioned above is examined based on allsky pictures of an overcast sky on 14 July and under broken cloud conditions on 18 July.

Different pattern distributions are not investigated in this work, since SCCD sky radiance measurements were performed with a pattern distribution identical to that of MUDIS. The influence of time asynchronism could also not be examined, since the sampling interval of allsky pictures was set to 40 s in the first intercomparison campaign and 5 min in the second campaign. The time asynchronism between MUDIS and SCCD is estimated to be less than 10 s, therefore the allsky pictures were not suitable for the evaluation of its influence. The influence of the FOV on the variability of sky radiance is also not investigated in this thesis.
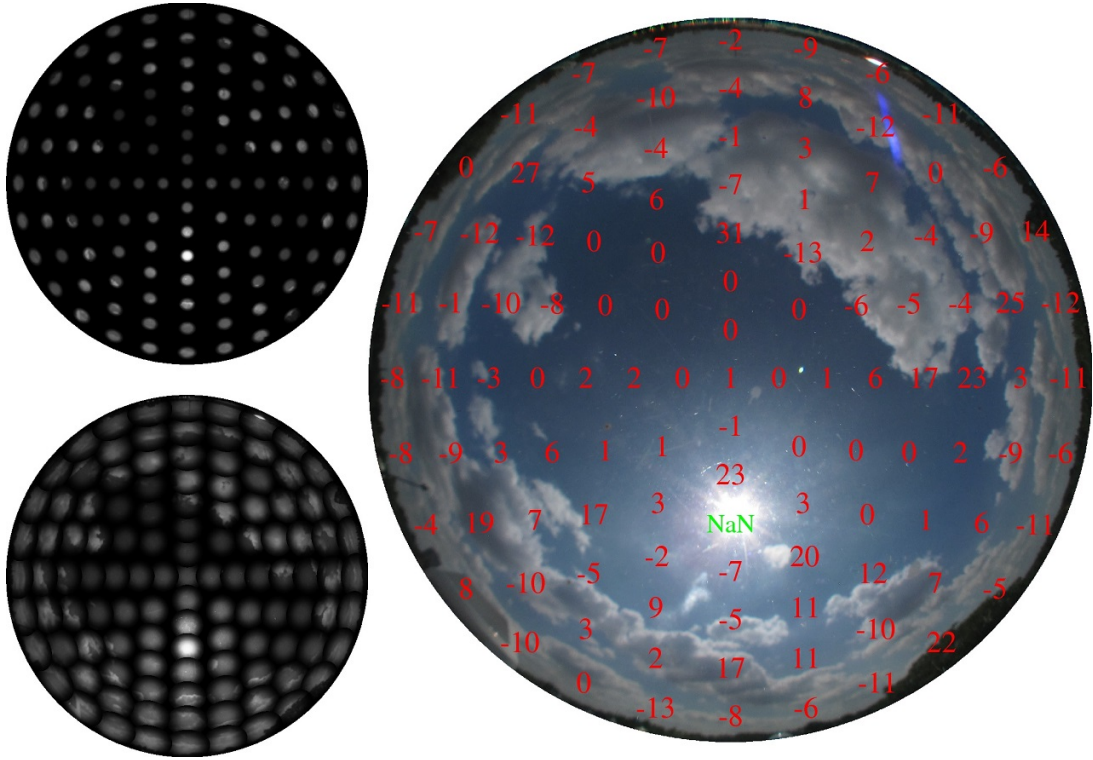
Figure 6.2: FOV induced variations predicted with the AMS algorithm based on an allsky picture captured on 18 July at 11:35 UTC. The two plots on the left side of the figure show the viewing angles simulated with two different FOVs (top: SCCD with 5° FOV, bottom: MUDIS with 9° FOV), applied to the red channel of the allsky picture. The variation in percent, caused by the different FOVs, is shown as a red number at each particular viewing angle in the right plot. Viewing directions in which more than 15% of the pixels are oversaturated or noisy are marked with 'NaN'.

6.1 Influence of FOV Differences

The influence of FOV differences on the standard deviation of measured MUDIS/SCCD radiance ratios is evaluated with the AMS algorithm by emulating MUDIS and SCCD measurements based on allsky pictures captured in 5 min intervals. The angular response of SCCD and MUDIS used for the AMS simulation are presented in Section 3.1.1 and Section 3.2.5, respectively. The angular response of the SCCD entrance optics has a FOV of 5°, but each fiber of the MUDIS entrance optics dome has an individual FOV which is also wavelength dependent. The angular response derived from four MUDIS channels has therefore been averaged and is assumed to be the most probable response. Furthermore, for a first simulation a wavelength independent FOV is assumed and the angular response at 602 nm (position of the maximum response of the red channel) with a 9° FOV has been chosen for all three color channels of the allsky picture. An example for FOV-induced variations for such a setup is shown in Figure 6.2. The variations induced by FOV differences are shown as red numbers in percent in the right allsky plot. Simulated FOVs in which more than 15% of the pixels are oversaturated (>253 counts) or noisy (<5 counts) are not taken into account for further comparisons and are marked with 'NaN' in the allsky picture. Since sky radiance varies less in cloudless situations compared to cloudy situations, the different FOV has a small influence on

Figure 6.3: Histograms created from all 9°/5° ratios of the allsky pictures taken between sunrise and sunset on 14 and 18 July. The vertical dashed lines represent the corresponding standard deviations, the vertical solid lines the mean of all examined ratios. An individual histogram is displayed for each color channel. In the lower six histograms the horizon points at a viewing angle of 84° have been excluded from the dataset.

the measurement results near to the cloudless zenith of the sky. Higher variations occur at the edges of clouds, e.g., in the northern direction. An entrance optics with a larger FOV and a viewing direction near a cloud will perceive the radiance of a higher or lower percentage of clouds compared to the entrance optics with the smaller FOV. A systematic difference occurs close to the horizon, where entrance optics with a 9° FOV will see parts of the horizon, while instruments with a FOV of 5° will be less affected by the horizon.

The systematic difference can also be identified in histograms created from all 9°/5° ratios of the allsky pictures taken between sunrise and sunset on 14 and 18 July (Figure 6.3). At each color channel a minor maximum is observed at ratios of 0.8 to 0.9. When the horizon points are excluded from the histograms, the minor maximum is no longer apparent. The FOV difference causes a systematic deviation for measurements near to the horizon, since the wider FOV partially includes the horizon at flat viewing angles. The 1σ standard deviation induced by different FOVs is less than 2% for overcast sky and shows a significant wavelength dependence for cloudy days, varying between 3.3% and 6.5% from the blue to the red channel.

6.2 Influence of the MUDIS/SCCD Intercalibration

The distortion of horizon points is not found in actual MUDIS measurements, it is therefore assumed that the intercalibration process compensates the majority of the systematical differences for the horizon points. Figure 6.4 shows the systematic difference in percent received by applying the MUDIS intercomparison algorithm to simulated measurements with 9° and 5° FOVs. While most points show no systematic difference, the horizon points are systematically smaller due to the applied calibration factor. When the calibration factors are applied to the simulations shown in Figure 6.3, the minor maximum disappears (Figure 6.5).

Figure 6.4: Results of an emulated MUDIS intercomparison. The three plots with the corresponding numbers, arranged like the MUDIS pattern, represent the correction factors derived for the red, green and blue channel.

6.3 Influence of a FOV Wavelength Dependence

The characterization of the MUDIS entrance optics dome shows that the angular response of the evaluated fibers is wavelength dependent (Figure 3.17). Therefore, the calculations of the FOV differences have been repeated with three individual FOVs for each color channel of the allsky pictures. Since the maximum sensitivity of the red, green and blue color channel is at 602, 527 and 441 nm, respectively, the individual angular responses are derived from the wavelength
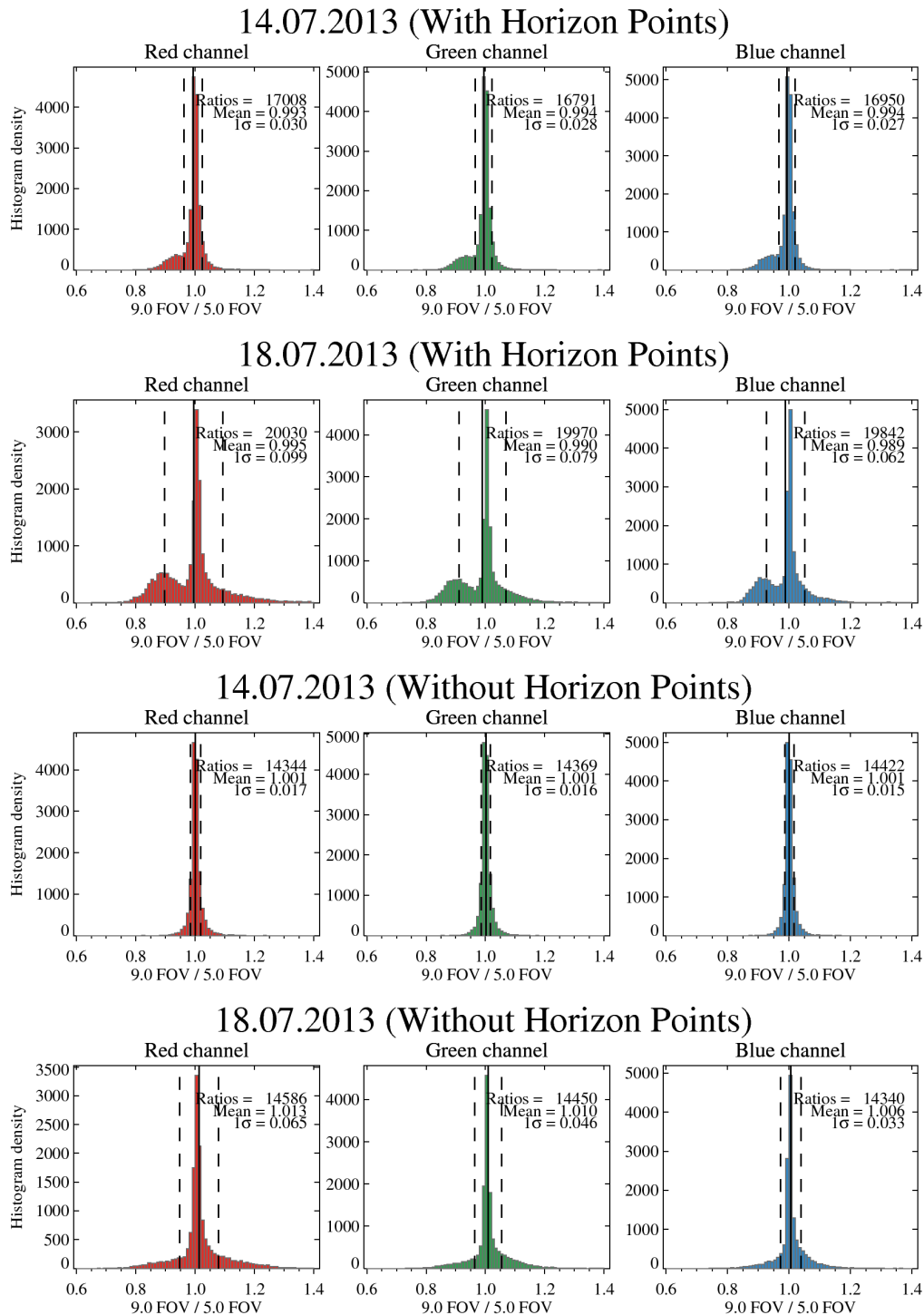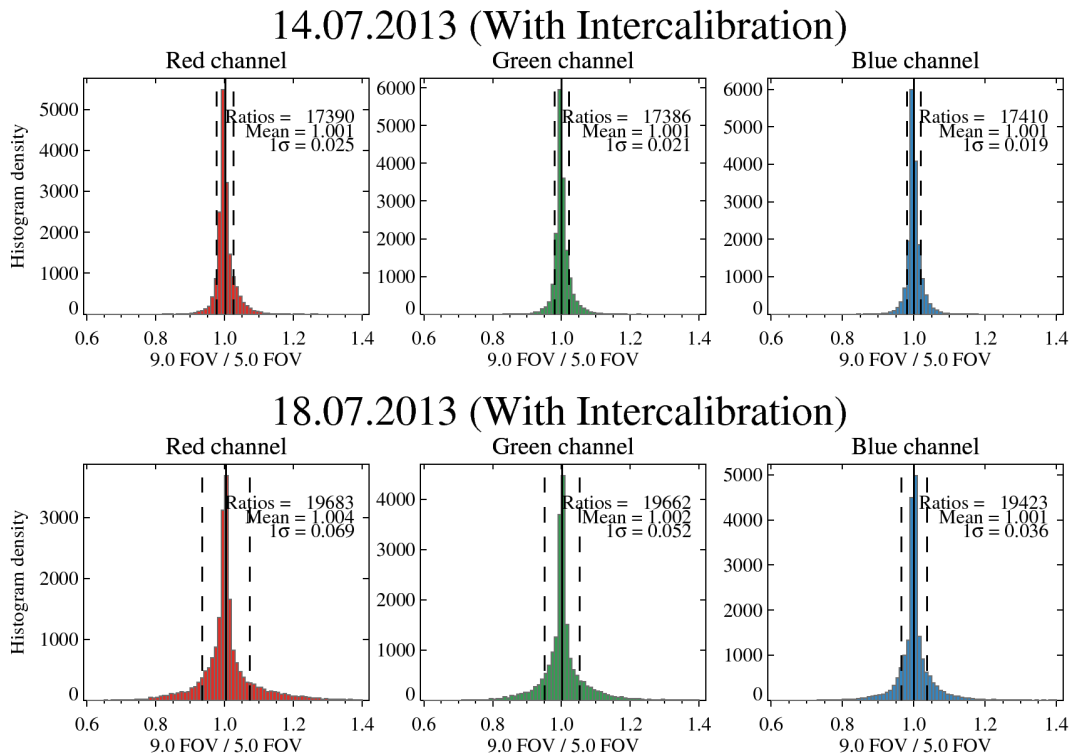
Figure 6.5: Histograms created from 9°/5° ratios of the allsky pictures taken between sunrise and sunset on 14 and 18 July, modified with an emulated MUDIS intercalibration. The vertical dashed lines represent the corresponding standard deviations, the vertical solid lines the mean of all examined ratios. An individual histogram is displayed for each color channel.

dependent mean angular response of four MUDIS channels (Figure 6.6). The chosen responses show a FOV of 9° at 602 nm, 10.5° at 527 nm and 14.1° at 441 nm, respectively. The results of the simulation are shown in Figure 6.7. Since the simulations have been conducted with a 9° FOV before, the red channel shows the same standard deviation compared to Figure 6.5. The wider FOV used for the green and blue channel increase the standard deviation by up to 4% and up to 5%, respectively. It can be concluded, that the wavelength dependence of the FOV equalizes the higher standard deviation of the sky radiance.

6.4 Influence of Entrance Optics Tilt

An unintentional tilt of an entrance optics compared to its expected viewing angle has a significant influence on radiance measurements. Radiance measurements performed during situations in which the cloud scenery viewed in the tilted direction differs from the scenery of the expected direction will have an increased random uncertainty. The characteristic spectral, temporal and spatial distribution of sky radiance under a cloudless sky (Grant et al., 1997; Wuttke et al., 2006) also lead to systematic differences with a diurnal variation. An example of a tilt angle leading to such a systematic difference is shown in Figure 6.8. Illustrated are three allsky measurements performed in the morning, at noon and in the afternoon of 18 July 2013. Two viewing directions are marked with colored rings: The zenith viewing direction is marked green and a viewing direction with a 9° tilt eastwards is marked red. Since the
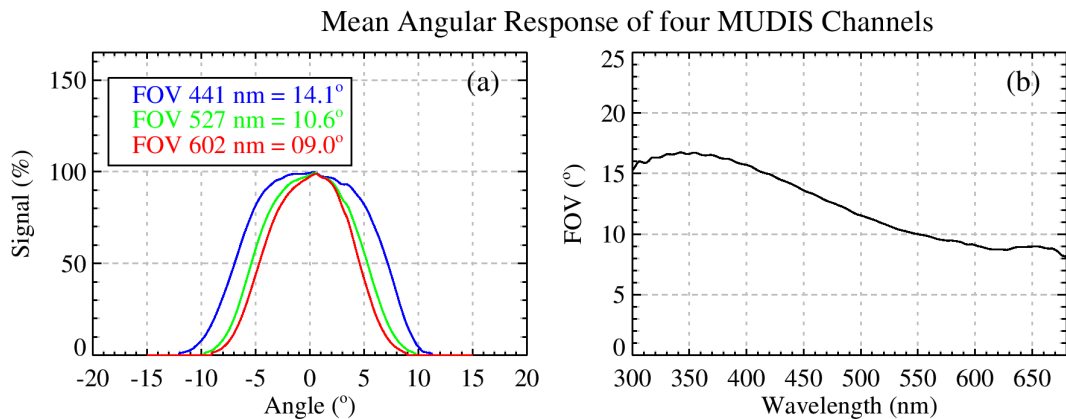
Figure 6.6: In (a) the angular response, derived by averaging the angular response of four MUDIS channels, is shown for three different wavelengths. Plot (b) shows the mean wavelength dependence of the FOV.
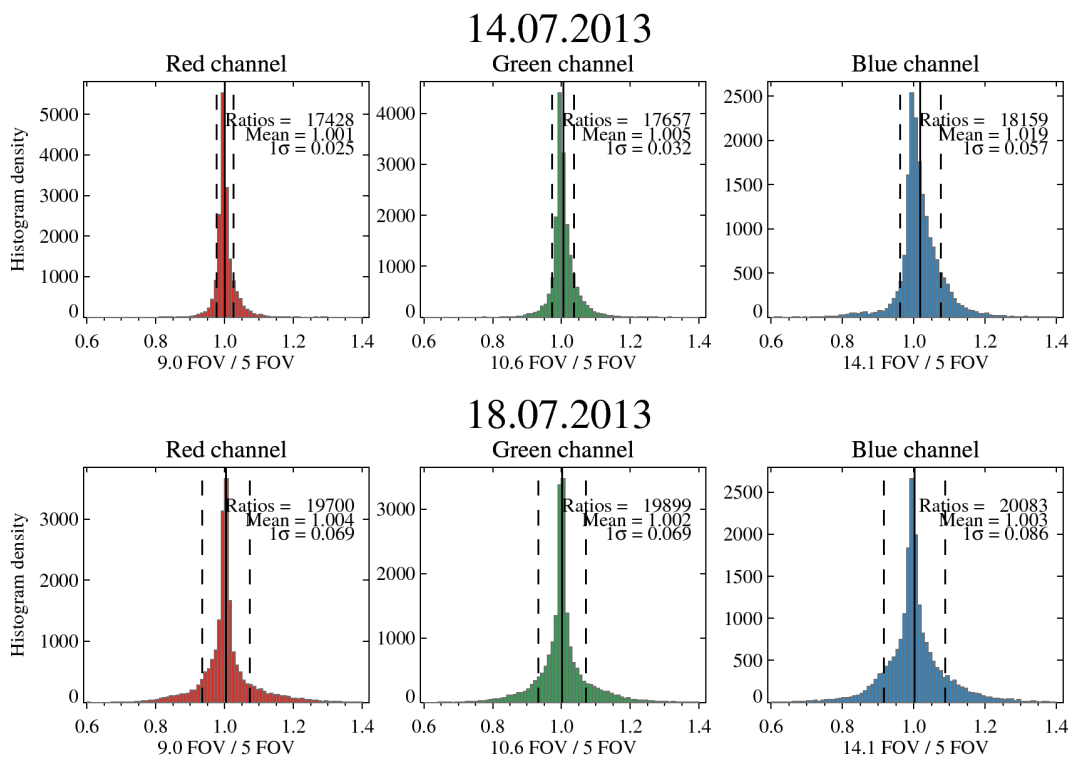
Figure 6.7: Influence of the MUDIS FOV wavelength dependence. Histograms are created from 9°/5°, 10.6°/5° and 14.1°/5° ratios of the allsky pictures taken between sunrise and sunset on 14 and 18 July. The vertical dashed lines represent the corresponding standard deviations, the vertical solid lines the mean of all examined ratios. An individual histogram is displayed for each color channel.

pictures are displayed in 20 greyscales it is apparent, that the spatial variation of sky radiance increases closer to the solar position and decreases towards the roughly oval shaped sky radiance minimum observed in a 90° angle relative to the elevation angle of the sun. In the morning,
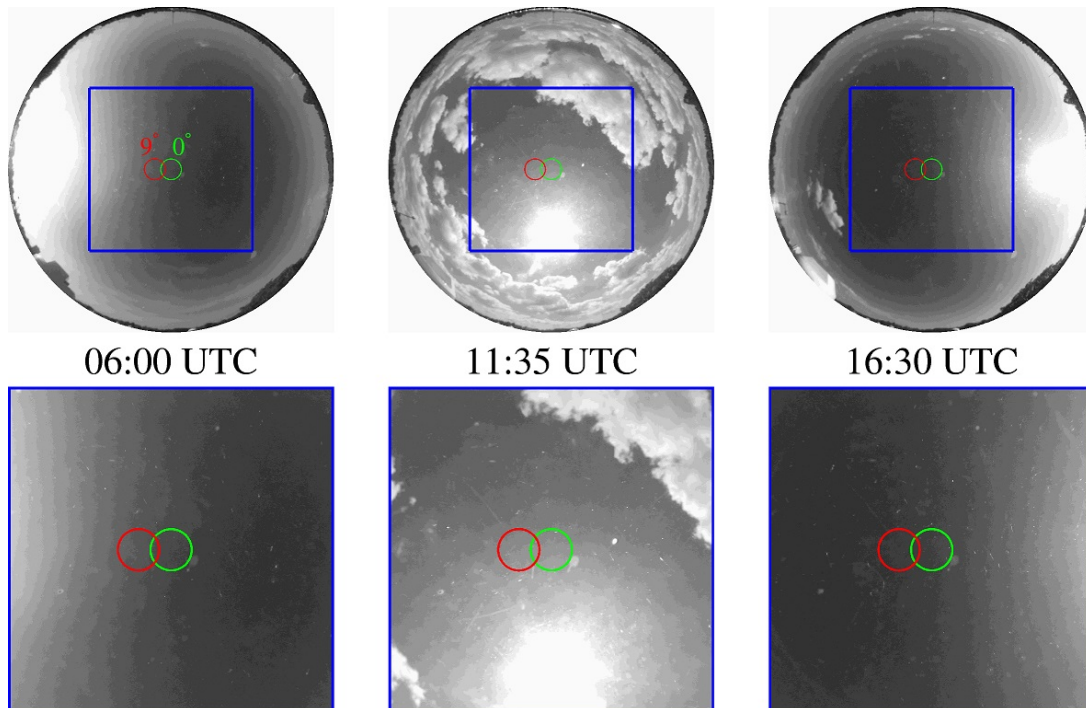
Figure 6.8: Shown is the red channel of three allsky pictures of 18 July 2013, captured at 06, 11:35 and 16:30 UTC. The green ring marks a zenith viewing direction with a FOV of 12°, the red ring marks a viewing direction tilted by 9° eastwards. The pictures are displayed in 20 greyscales in order to visualize the temporal and spatial radiance variation.

an instrument with an entrance optics tilted eastwards will receive more radiance compared to measurements performed directly in the zenith direction. Until noon the solar disc moves towards the south, now an entrance optics tilted eastwards will measured roughly the same amount of radiance compared to the zenith direction due to the oval shape of the radiance minimum. In the afternoon the entrance optics tilted eastwards will receive less radiance compared to the zenith direction. However, the spatial sky radiance variation decreases towards the minimum, therefore the systematic difference will be a little bit smaller compared to the difference observed in the morning. The example also shows that direction and tilt angle have an impact on the observed diurnal variation. Since the tilt of the MUDIS zenith channel has been characterized, the diurnal variation of sky radiance measurements performed with an entrance optics tilted approx. 2.5° eastwards has been calculated with the AMS algorithm and is shown in Figure 6.9. During overcast conditions on 14 July no systematic difference is apparent, nevertheless the entrance optics tilt leads to uncertainty of the measured sky radiance (Figure 6.9(c)). On 18 July a systematic difference of up to 9% at 8 UTC and down to -5% at 15 UTC is observed in Figure 6.9(d). The highest difference is observed for the red channel, since the variance of sky radiance increases with longer wavelengths, as shown before in Figure 4.7. The high uncertainty observed during broken cloud conditions between 8 and 15 UTC is caused by both wavelength dependence and tilt of the angular response of MUDIS.

The overall influence of unintentionally tilted MUDIS viewing directions is hard to quantify, since the characterization of the fiber FOV has only been performed for four viewing direction yet. Therefore a set of random variations of zenith and azimuth angles in the range of $\pm 0 - 3°$ is assumed for the fibers of the entrance optics dome. In Figure 6.10 the results of a simulation,
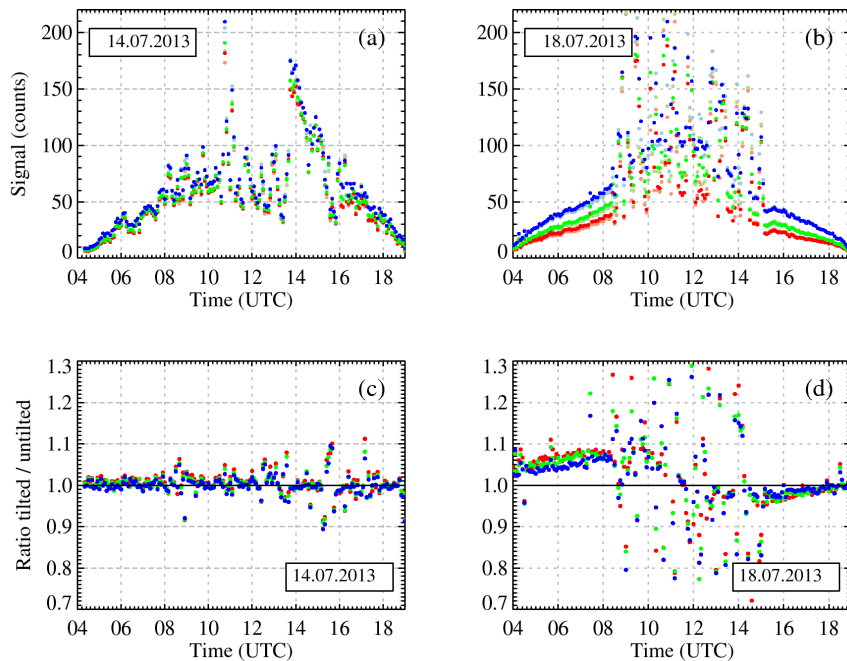
Figure 6.9: AMS simulated diurnal variation of MUDIS zenith sky radiance measurements that are tilted 2.5° eastwards.
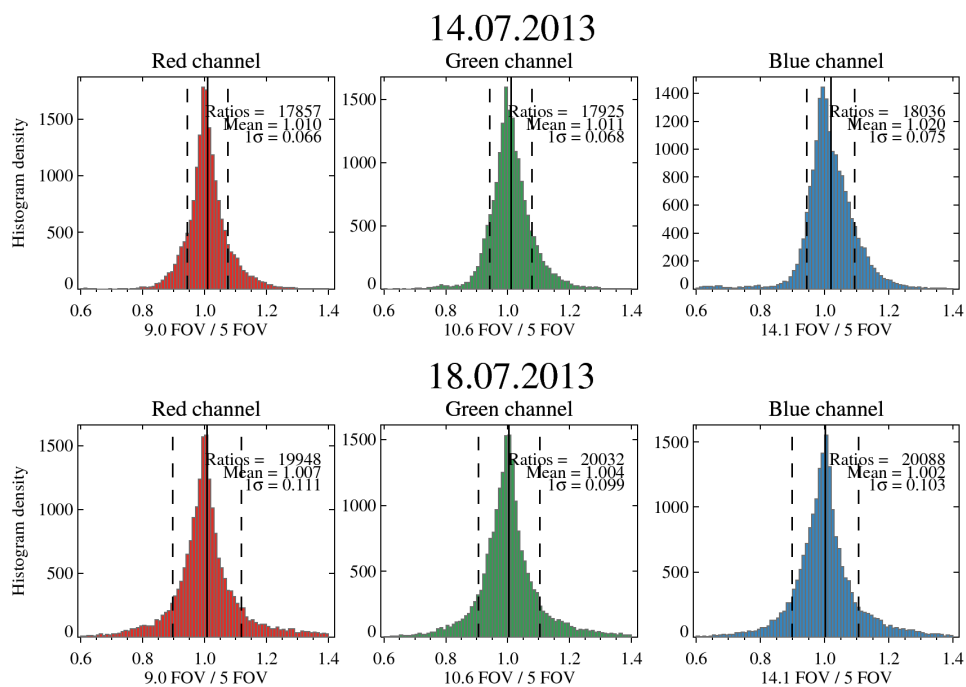
Figure 6.10: Histograms of ratios of randomly tilted/untilted viewing angles. The viewing angles are simulated based on the red, green and blue channel of allsky pictures taken between sunrise and sunset on the 14, and 18 July 2013. The vertical dashed lines represent the corresponding standard deviations, the vertical solid lines the mean of all examined ratios.

showing the influence of this random variation, are presented. The simulations also take the FOV wavelength dependence, the FOV differences between MUDIS and SCCD and the influence of the MUDIS/SCCD intercalibration into account. The standard deviation of the red channel is 4% higher, the green channel is about 3% higher and the blue channel about 2% higher compared to non-tilted simulations. Compared to standard deviations derived from actual MUDIS measurements of the 14 and 18 July the standard deviations calculated for the red and green channel are nearly equal. Since the time asynchronism is not yet considered, the assumed random tilts might be chosen too high. The blue channel shows a standard deviation higher compared to the measurements, it is assumed that the observed wavelength dependence of the FOV tilt described in Section 3.2.5 might be the reason. For more accurate simulations a detailed knowledge of the MUDIS entrance optics is therefore necessary.

6.5 AMS Algorithm - Summary and Discussion

An algorithm is presented that is capable of performing instrument parameter studies based on allsky pictures. Instrument comparison measurements provide only deviations that result from the sum of all instrument differences. Therefore, the AMS algorithm is a useful tool for the evaluation of the influence of individual instrument parameters on the observed standard deviation. By performing the simulations for each color channel of the camera separately, the AMS algorithm provides a limited spectral information and helps to understand observed spectral dependencies.

First of all, the influence of the FOV difference between MUDIS and SCCD has been examined by simulating sky radiance measurements with a 5° and a 9° FOV from datasets of allsky pictures of both cloudy and overcast days. The standard deviation between the simulated instruments, calculated for broken clouds, ranges from 4% for the blue color channel to 7% for the red channel. For overcast sky the standard deviation of approx. 2% for all three color channels has been calculated. Since the MUDIS characterization revealed a wavelength dependent FOV of the used fibers, different FOVs were considered with the AMS algorithm for each color channel, ranging from 9° for the red channel, over 10.6° for the green channel, to 14.1° for the blue channel. The wider FOV for shorter wavelengths compensated the higher variation of the sky for longer wavelengths. Consequently, the simulations showed the highest standard deviations for the blue channel.

For an examination of the influence of incorrectly tilted MUDIS viewing directions the zenith viewing angle of a simulated MUDIS channel has been tilted by 2.5° eastwards. The diurnal shift of the three color channels show a similar diurnal shift for cloudless conditions in comparison to the diurnal shifts observed during MUDIS instrument comparisons on 15, 16 an 18 July (e.g., Section 5.2.2). In order to examine the influence of unintended tilts on the standard deviation calculated from all MUDIS channels, the zenith and azimuth angles of all MUDIS channels have been modified with random values of $\pm 0\text{-}3°$. For broken clouds a 1σ standard deviation of 10% for the blue channel and 11% for the red channel has been calculated with the AMS algorithm. For overcast sky the deviation is approx. 7%. The simulated tilt amplified the influence of sky variance and results in standard deviations similar to those encountered during comparison campaigns. However, the wavelength dependence of the simulated standard deviation is a few percent smaller compared to the instrument comparisons. The difference between simulations and measurements might be explained by the uncertainties arising from the applied simple stray light correction method.

The conducted parameter studies based on allsky pictures of two comparison days finally lead to a better understanding of the impact of each individual instrument difference, therefore, the feasibility of explanations for the observed differences could be tested.

7 Summary and Conclusions

The development, characterization and validation of a novel multidirectional spectroradiometer (MUDIS), capable of measuring sky radiance as a function of zenith and azimuth angle in seconds rather than minutes is described in this work. The instrument enables new possibilities in studying the spectral sky radiance during fast changing cloud conditions without the disadvantages of a scanning instrument. MUDIS is based on an imaging spectroradiometer to which a bundle of optical fibers is attached. Each fiber of the bundle is embedded in a hemispherical dome and directed to a different direction of the sky, enabling MUDIS to simultaneously measure spectral radiance in 113 directions and in an operational wavelength range of 250 to 680 nm.

Two instrument comparisons have been carried out with a point scanning spectroradiometer (SCCD) and a wavelength scanning NDACC spectroradiometer in order to validate sky radiance measurements performed with MUDIS. In addition to the intercomparison methods described in Pissulla et al. (2009) a statistical and an integral instrument comparison was conducted in order to evaluate the performance of MUDIS. Especially the statistical approach enables the examination of instrument performance with regard to various weather conditions.

The first instrument comparison has been carried out between MUDIS and SCCD in October 2012. In order to calibrate MUDIS an intercalibration with the SCCD has been performed. During the campaign up to three MUDIS channels were illuminated by direct sunlight during cloudless conditions. Stray light effects arising from oversaturation and the influence of solar radiation in the circumsolar region rendered approx. 16% of all measurements performed on those days useless. Measurements performed under an overcast sky were not affected from oversaturation, but show a systematic difference due to a condensation issue of the MUDIS entrance optics occurring on those days.

As a consequence of the experiences gained with MUDIS in the first instrument comparison, a rotating shadow band and a ventilation for the entrance optics dome has been developed. Stray light induced by direct sunlight and sensitivity changes due to condensation were therefore no longer an issue during the second instrument comparison, performed with MUDIS, SCCD and the NDACC instrument in July 2013. The systematic difference calculated from of all spectral radiance measurements performed with both instruments under translucent (cirrus fibratus), overcast (stratus) and broken clouds (cumulus) is less than 3% between 310 and 600 nm. The observed standard deviation is highly dependent on the meteorological conditions. Measurements performed under a cirrus fibratus covered sky show a 1σ standard deviation between 4% and 8% between 310 and 600 nm, with a minimum at 330 nm. Measurements performed on days with broken clouds show a higher 1σ standard deviation between 6% and 13% between 310 and 600 nm, again with a minimum at 330 nm. Measurements performed under an overcast sky show a 1σ standard deviation of less than 8% between 330 and 600 nm and up to 18% at 310 nm. Rising standard deviations for wavelengths lower than 330 nm are explainable by the exponentially decreasing sky radiance in the UV and the detection threshold of the SCCD instrument. The observed minimum of the standard deviation at 330 nm can be explained by the interaction of a higher spatial variation of sky radiance at longer wavelengths and instrument differences, namely the measurement time asynchronism, different instrument FOVs and incorrectly tilted MUDIS viewing directions. The uncertainties arising from the applied stray light correction method might also be partially causing the observed gradually

increase of the uncertainty with longer wavelengths.

The rapid decrease of MUDIS performance for wavelengths longer than 600 nm is assumed to be caused by stray light originating from second order diffraction, rendering the wavelength region between 600 and 680 nm useless, as long as the current simple stray light method is not improved.

Variations determined during the instrument comparisons result from the combination of field of view differences, unintended tilts of the MUDIS viewing angles, and several additional instrument parameters. Since most parameters are not changeable and also depend on each other, it is impossible to examine those parameters separately by intercomparison methods. Therefore, an algorithm has been developed that simulates measurements with variable instrument parameters based on allsky pictures. This tool enables instrument parameter studies which help to understand systematic and random differences of sky radiance measurements performed with different spectroradiometers. By performing the simulations for each color channel of the camera separately, the AMS algorithm provides limited spectral information and helps to understand the observed spectral differences. First of all, the influence of the FOV difference between MUDIS and SCCD has been examined by emulating sky radiance measurements with a 5° and a 9° FOV from allsky pictures of both cloudy and overcast days. The standard deviation calculated for broken clouds ranges from 4% for the blue color channel to 7% for the red channel. For overcast sky the standard deviation of approx. 2% for all three color channels has been calculated. Since the MUDIS characterization revealed a wavelength dependent FOV of the used fibers the AMS algorithm considers different FOVs for each color channel, ranging from 9° for the red channel, over 10.6° for the green channel, to 14.1° for the blue channel. In order to evaluate the influence of incorrectly tilted MUDIS viewing directions the zenith and azimuth angles of the MUDIS measurement pattern have been altered with random values of ±0-3°. For broken clouds a 1σ standard deviation of 10% for the blue channel and 11% for the red channel has been calculated with the AMS algorithm. For overcast sky the deviation is approx. 7%. Parameter studies based on allsky pictures of the particular intercomparison days finally lead to a better understanding of the impact of each individual instrument difference. Feasible explanations for the observed differences due to different instrument FOVs, tilts of viewing angles and influences of the intercalibration process could be found. The observed diurnal shift of MUDIS zenith radiance measurements could be reproduced by a simulated eastward tilt of the MUDIS zenith point.

8 Outlook

Several topics need to be addressed in the future in order to further improve the performance of MUDIS:

- **Non-linearity**. A non-linearity characterization with varying input signals should be conducted in order to separate sensor non-linearity and integration time non-linearity.

- **FOV characterization**. The FOV of the MUDIS entrance optics dome needs to be characterized more thoroughly, since an exact knowledge of the angular response and tilt of each MUDIS channel is necessary in order to reduce the uncertainty of performed sky radiance measurements.

- **FOV correction**. It might be possible to correct the MUDIS viewing angles by the application of small apertures to the surface of the weather protection dome of the entrance optics. The apertures could be dimensioned in a way so that a smaller FOV is achieved. This would benefit the temporal variability measured with MUDIS. Before changing the entrance optics, the influence of a smaller FOV on the variation of sky radiance time series should be investigated with the AMS algorithm.

- **Absolute calibration**. A method directly traceable to a primary calibration standard is desirable for the stand-alone operation of MUDIS. The intercalibration performed in this thesis is time consuming, since in addition a fully operational SCCD instrument is needed for this kind of calibration. A possible solution could be a calibration based on an integrating sphere, where one or more entrances of MUDIS are illuminated with a reproducible radiance signal.

- **Horizon shadow band**. As soon as the intercalibration method is replaced by an alternative, the measurements with high zenith angles will be more strongly influenced by the horizon. By applying an azimuthal shadow ring and characterizing the induced systematic difference, the influence of the horizon on MUDIS measurements could be reduced.

- **Shadow band influence**. In this work, MUDIS channels shaded by the shadow band are removed by a simple intercomparison process with SCCD. An algorithm needs to be developed that calculates the position of the shadow band and removes shaded MUDIS points independently.

- **Stray light correction**. The applied simple stray light correction should be improved, since the instrument comparisons indicated an increased uncertainty for wavelengths longer than 500 nm. Beyond 600 nm the measurements of MUDIS are basically useless due to the influence of stray light originating from second order diffraction. A matrix correction method similar to the SCCD instrument could be developed, where second order diffraction is taken into account by using a UV laser or bandpass filter for the stray light characterization. However, since a three-dimensional stray light correction matrix is needed in order to correct the two-dimensional sensor area of the MUDIS imager, a substantially higher processing time is expected.

- **Intercomparison with other instruments.** It is desirable to compare MUDIS with absolute radiance measuring instruments of other institutes by conducting a comparison campaign similar to Pissulla et al. (2009), and applying the enhanced comparison methods described in this work.

Besides further improvements of the instrument performance several applications for MUDIS sky radiance measurements are already planned for the future. Experiments are planned where plants or samples of various materials are exposed to sunlight and sky radiance is measured with MUDIS simultaneously. This will provide sky radiance datasets in a uniquely high temporal resolution. This enables a precise calculation of cause-effect relationships, especially for fast occurring effects. The data can also be used for deriving the UV exposure of a human body in a high temporal resolution. This enables the precise calculation of the time needed to achieve a particular UV dose at different parts of the human body. It will also be tested if MUDIS measurements are suitable for deriving ozone profiles and aerosol properties in high temporal resolutions.

Despite the open tasks concerning the improvement of the instrument, this thesis shows that it is already possible to perform MUDIS sky radiance measurements with acceptable and known uncertainties compared to the present instrumentation.

Appendix

A MUDIS Publication

Simultaneous measurement of spectral sky radiance by a non-scanning multidirectional spectroradiometer (MUDIS)

Stefan Riechelmann[1], Michael Schrempf and Gunther Seckmeyer

Institut für Meteorologie und Klimatologie, Leibniz Universität Hannover, Herrenhäuser Str. 2, D-30419 Hannover, Germany

E-mail: riechelmann@muk.uni-hannover.de

Abstract
We present a novel non-scanning multidirectional spectroradiometer (MUDIS) measuring the spectral sky radiance as a function of zenith and azimuth angle with a high spectral and temporal resolution. The instrument is based on a hyperspectral imager and measures spectral sky radiance in the wavelength range of 250–600 nm at 113 different directions simultaneously. MUDIS has been intercalibrated with a sky scanning CCD spectroradiometer (SCCD). Sky radiance measurements have been performed with both instruments under cloudless and overcast sky. The spectral actinic irradiance derived from those measurements agrees within 8% for wavelengths higher than 320 nm. The bias between synchronous MUDIS and SCCD sky radiance measurements during cloudless and overcast sky is below 5% for 320 and 500 nm with a 1σ standard deviation of less than 10%. MUDIS enables us to perform more than 220 000 spectral sky radiance measurements instead of approximately 6000 SCCD spectral sky radiance measurements per day and to measure spatial variations of spectral sky radiance simultaneously.

Keywords: UV spectroradiometry, UV sky radiance, UV imaging spectroradiometer

(Some figures may appear in colour only in the online journal)

1. Introduction

Measurements of spectral sky radiance and spectral direct irradiance are useful for many applications where knowledge of temporal and spatial information of the radiation field is necessary. Possible applications are the calculation of power yield of tilted solar cells (Beringer *et al* 2011) or the determination of spectral exposure of complex objects like the human body (Seckmeyer *et al* 2013). Sky radiance measurements can also be used to derive aerosol properties (Dubovik and King 2000), cloud properties (Hirsch *et al* 2012), as well as aerosol and trace gas profiles (Hönninger *et al* 2004).

Direct irradiance can be acquired in high temporal resolution, since only a single direction has to be measured (Kouremeti *et al* 2008). The measurement of spectral sky radiance is a more demanding task, since this four-dimensional unit depends on zenith angle, azimuth angle, wavelength and time. Spectral sky radiance as a function of zenith and azimuth angle is commonly derived by sequentially measuring a set of directions in the sky (further denoted as a sky scan). Sky scans of spectral radiance of the UV part of the spectrum have been successfully performed with spectroradiometers based on wavelength scanning double monochromators (Blumthaler *et al* 1996, Weihs *et al* 2000, Wuttke and Seckmeyer 2006, Cordero *et al* 2013). Double monochromator spectroradiometers fulfil high standards in terms of instrument stability, stray light reduction and

---

[1] Author to whom any correspondence should be addressed.

1

wavelength resolution and thus provide excellent performance in the UV. They also have been thoroughly tested through instrument intercomparison campaigns (Lantz *et al* 2008, Pissulla *et al* 2009). However, due to their wavelength scanning principle, they are only capable of measuring a few chosen wavelengths at each sky point in order to perform a sky scan in a reasonable time frame. To overcome this shortage, systems based on charged coupled device (CCD) array spectrometers have been developed, e.g., by Kouremeti *et al* (2008) and Dunagan *et al* (2013) which are capable of measuring spectral radiance spectra simultaneously over their operational wavelength range. Nevertheless, a sky scan still takes several minutes depending on the speed of the positioning device turning the entrance optics, the spatial resolution and the measuring speed of the instrument. Therefore, measurement systems based on CCD arrays still provide poor temporal resolution and lack the capability to simultaneously measure the spectral sky radiance as a function of zenith and azimuth angle. However, this application would be desirable, since sky radiance usually changes rapidly due to movement and change of cloud coverage (Kuchinke *et al* 2004). A technical solution that is capable of measuring sky radiance with high spatial and temporal but low spectral resolution is provided by imager systems with fish-eye lenses (Román *et al* 2012, Tohsing *et al* 2013). Combining a tunable filter (Hardeberg *et al* 2002) or a Fabry–Perot interferometer (Pisani and Zucco 2009) with a fish-eye imager system improves the spectral resolution of such a system. Nevertheless, the wavelength resolution and sampling intervals of those systems are limited and additionally the wavelengths need to be scanned. Also, there is currently no UV transmitting fish-eye lens commercially available which means that UV sky radiance measurements of the whole hemisphere at once cannot be performed by these techniques yet.

To fill the gap of instruments capable of performing simultaneous spectral sky radiance measurements in the UV, we present a novel multidirectional spectroradiometer (MUDIS). The developed instrument performs UV spectral radiance measurements simultaneously in 113 directions of the sky with a high spectral and temporal resolution. We performed an instrument intercalibration with a sky SCCD and present results of an intercomparison between both instruments.

2. Instruments and methods

2.1. Multidirectional spectroradiometer

The developed spectroradiometer is shown in figure 1. The main component of MUDIS is a hyperspectral imager consisting of a UV-sensitive CCD camera (PCO AG, Kelheim, Germany) and an Offner imaging spectrometer. This imager design is commonly used for so-called push broom measurements of two-dimensional sceneries. Instead of measuring each pixel of a scene sequentially, push broom instruments are capable of performing spectral measurements of a whole line of pixels at once (Davis *et al* 2002). However, instead of measuring line by line with a camera lens and an entrance slit, we attached a bundle of optical fibres to the
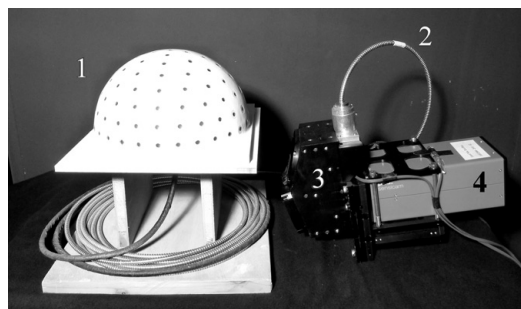

Figure 1. Main components of MUDIS: hemispherical entrance optics dome with weather protection (1), fibre bundle (2), Offner imaging spectrometer (3), UV-sensitive CCD camera (4). Both the camera and the spectrometer are operated in a weatherproof temperature-stabilized box (not shown here).

imager consisting of 113 single fibres lined up to a slit. The other ends of the fibres are embedded in a hemispherical-shaped dome in which the 113 fibres are evenly distributed in zenith and azimuth directions (figure 1). The field of view (FOV) of the fibres is not additionally limited by any optical part. A characterization of the fibres showed a FOV of 10.6° at 600 nm increasing up to 18.4° for shorter wavelengths (figure 2). A single measurement (sky capture) performed with MUDIS therefore simultaneously performs 113 sky radiance measurements in different zenith and azimuth directions.

MUDIS is capable of measuring spectra from 250 to 600 nm with a bandwidth of approximately 2 nm and a sampling interval of 0.4 nm. Figure 3 shows raw data captured with this setup under cloudless (*a*) and overcast (*b*) sky. Under cloudless sky, one fibre of the entrance optics is illuminated by direct sunlight. The corresponding area of the CCD sensor is oversaturated and several adjacent rows are affected by stray light. When measuring sky radiance during overcast sky, no saturation occurs and consequently stray light is less intense. In order to remove stray light in the UV, we apply a simple stray light correction method. Eight sensor rows that are not illuminated and thus only detect stray light during overcast sky (dashed lines in figure 3(*b*)) are averaged and the resulting average stray light spectrum is assumed to be sufficiently representative for the whole sensor area. Furthermore, illuminated sensor rows receive negligible radiation below 290 nm due to ozone absorption in the atmosphere. Each illuminated sensor row is now stray light corrected by a two-step method. First, the previously derived average stray light spectrum is scaled to the signal of the illuminated sensor row at 285 nm. Second, the scaled stray light is subtracted from the row. This method is similar to a stray light correction method developed by Jäkel *et al* (2007), where spectral filters are used to derive a reference stray light for a CCD array spectroradiometer. Nevertheless, we found that stray light originating from oversaturation differs in terms of intensity and spectrum from stray light observed without oversaturation. Rows affected by more than 20 counts of stray light at 285 nm are therefore discarded, since they cannot be corrected properly by this simple method.

2

S Riechelmann *et al*
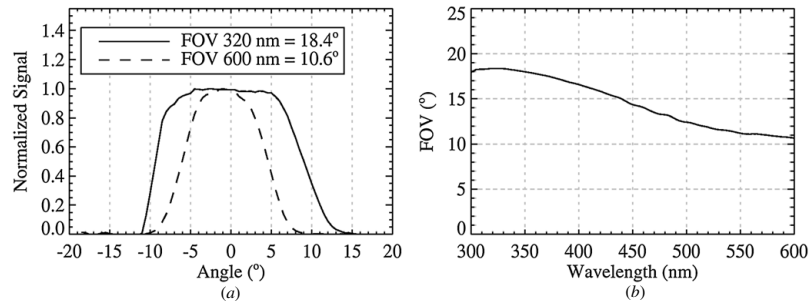
Figure 2. Field of view (FOV) of a typical fibre of the MUDIS instrument. Plot (*a*) shows the different angular response to light with 320 nm and 600 nm, respectively. Plot (*b*) shows the wavelength dependence of the FOV from 300 to 600 nm.
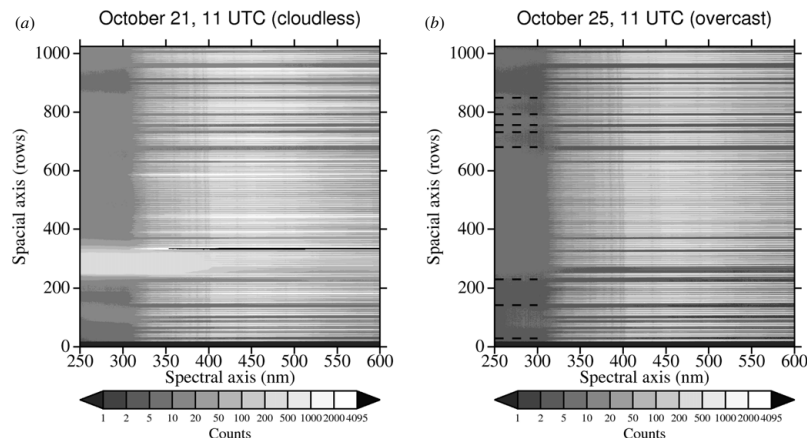
Figure 3. Raw data captured with MUDIS under cloudless (*a*) and overcast (*b*) sky. The measured counts are plotted on a logarithmic scale and saturated values are marked black. Under cloudless sky, one channel is saturated due to direct sunlight and stray light originating from this channel affects several adjacent rows, especially in the UV part of the spectrum. The dashed lines in plot (*b*) mark rows that are not illuminated and are used to derive an average stray light signal.

2.2. Scanning CCD spectroradiometer

The SCCD system consists of a UV-VIS-sensitive CCD array spectrometer (StellarNet, Tampa, FL, USA) with a single radiance entrance optics attached to the instrument via a fibre bundle. The entrance optics has a FOV of 5° and is mounted on a positioning device that is able to scan a desired pattern of points in the hemisphere. A SCCD sky scan identical to the MUDIS entrance optics dome pattern takes about 12 min. The SCCD has been calibrated based on a 1000 W tungsten halogen lamp which has been calibrated by the Physikalisch-Technische Bundesanstalt. Details on the calibration process are described in Pissulla *et al* (2009). Kouremeti *et al* (2008) quantify the uncertainty of this calibration method with up to 5.55% in the UV. The measurements have been stray light corrected with an algorithm adopted from Kreuter and Blumthaler (2009). The SCCD is capable of measuring in a wavelength range of 270–900 nm with a bandwidth of approximately 1 nm and a sampling interval of 0.3 nm. Measurements performed with the SCCD are convoluted with

a suitable slit function in order to achieve a 2 nm bandwidth for better spectral comparison with the MUDIS instrument.

2.3. MUDIS intercalibration

MUDIS is calibrated relative to the SCCD because a direct calibration similar to the SCCD calibration is not feasible. By measuring the same sky radiance scenery simultaneously with a calibrated and an uncalibrated instrument, it is possible to perform a radiometric calibration of the uncalibrated instrument (Röder *et al* 2005). While cloudless sky might be the most suitable scenery for this, task channels with high signal strength like those pointing to the circumsolar region or those saturated by direct irradiance lead to severe stray light contamination of vast regions of the sensor area (see figure 3(*a*)). Therefore, the intercalibration has been performed during overcast sky. The intercalibration has been performed based on 20 SCCD sky radiance scans performed on 22 October 2012 from 8:52 to 12:55 UTC. The solar zenith angle (SZA) during that time was between 69.4° and 63.2°. However, clouds are the dominating factor for the variability

3

Appendix

Meas. Sci. Technol. **24** (2013) 125501   S Riechelmann *et al*

of the spectral radiance in this situation, reducing the received radiance especially in the UV compared to the cloudless sky. Therefore, an average of the 20 measurements is used for the determination of the MUDIS sensitivity in order to reduce uncertainties arising from cloud movement and low signal strength in the UV. However, the resulting sensitivity is still uncertain for wavelengths shorter than 320 nm.

3. Results of instrument comparison

Spectral sky radiance measurements were performed with MUDIS and SCCD in Hannover, Germany on 21 October and 25 October 2012 from 06:00 UTC (sunrise) to 16:00 UTC (sunset). The SZA during the measurements ranges from 90° at sunrise and sunset up to 63.2° at noon on 21 October and 64.6° at noon on 25 October respectively. The days cover two meteorological conditions suitable for instrument comparison: On 21 October the sky was cloudless in the time period of 09:30–16:00 UTC. On 25 October the sky was covered with stratocumulus clouds in the time period of 06:00–14:00 UTC. MUDIS sky captures were performed with an integration time of 100 ms and 64 images were averaged to improve the signal-to-noise ratio of the measurement. Considering data processing time, MUDIS captured the spectral radiance every 12 s in 113 directions simultaneously, which is equal to more than 220 000 sky radiance measurements per day. The SCCD performed sky scans identical to the MUDIS capture pattern every 12 min, which is equal to 52 radiance scans or 5876 sky radiance measurements, respectively. By combining single points of MUDIS captures measured at approximately the same time as points of SCCD sky scans, a MUDIS sky scan synchronous to the SCCD is derived. Unfortunately, due to a failure of the SCCD on 21 October measurements between 11:45 and 13:00 UTC are missing.
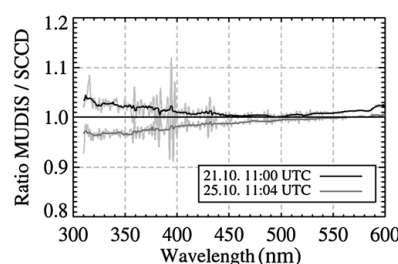
3.1. Comparison of spectral actinic irradiance

One possibility to quantify the difference between the two instruments is achieved by the integration of the measured spectral sky radiance over the hemisphere, which yields the spectral diffuse downward actinic irradiance (Seckmeyer *et al* 2010). Before integrating the spectral sky radiance, we remove faulty MUDIS measurements resulting from four broken fibres, oversaturation in the circumsolar region and measurements with high stray light (>20 counts at 285 nm). The remaining points are interpolated to a 5° grid using kriging interpolation (Isaaks and Srivastava 1989). The calculation of the spectral actinic irradiance $F_{DIFF}(\lambda)$ is performed after Kylling *et al* (2003):

$$F_{DIFF}(\lambda) = \int_0^{2\pi} \int_0^{\pi/2} L(\lambda, \theta, \phi) \sin\theta \, d\theta \, d\phi, \qquad (1)$$

where λ is the wavelength, θ the polar angle (90° zenith angle), ϕ the azimuth angle and $L(\lambda, \theta, \phi)$ the spectral sky radiance.

Figure 4 shows the ratio of the spectral actinic irradiances measured with MUDIS and SCCD on 21 October (cloudless) and 25 October (overcast) 2012 at around 11 UTC. In order to remove fluctuations due to remaining differences in instrument bandwidth and wavelength shifts, a 10 nm median filter is


Figure 4. Median filtered ratios of spectral actinic irradiances measured with MUDIS and SCCD under cloudless sky on 21 October (black line) and under overcast sky on 25 October (dark grey line), 2012. The unfiltered ratios are plotted in light grey.

applied. During cloudless sky, the ratio is decreasing from 1.04 to 1.00 in the wavelength range from 320 to 500 nm and increasing up to 1.02 from 500 to 600 nm. For overcast sky, the ratio is increasing from 0.96 to 1.00 from 320 to 600 nm. Based on this spectral comparison 320 and 500 nm are considered to be representative for the UV and VIS performance of MUDIS and therefore are used for the following temporal and spatial comparisons.

The variation of the actinic irradiance ratios at 320 and 500 nm during a cloudless time period on 21 October and an overcast time period on 25 October is shown in figure 5. Measurements of spectral actinic irradiance smaller than 10 mW m^{-2} nm^{-1}, which occur at sunrise and sunset, are not taken into account. The actinic irradiance measurements of MUDIS and SCCD show a deviation of 6% during cloudless sky and 8% during overcast sky. The ratios of the actinic irradiance measurements are higher at 320 nm compared to 500 nm under cloudless sky and, in contrast, lower at 320 nm compared to 500 nm for overcast sky. We assume that this behaviour is linked to the applied intercalibration method. A transmission change of the entrance optics can be excluded, since the effect occurs in the morning of 21 October as well. During this time, it was cloudy at first and the sky cleared up after 09:30 UTC. Broken clouds occurring on 25 October from 12:00 to 16:00 UTC lead to higher deviations of up to 12% caused by the differences in FOV of the instrument and acquisition time.

3.2. Sky radiance comparison under cloudless and overcast sky

In figure 6, the MUDIS and SCCD sky radiance measurements performed at noon under a cloudless sky are shown for two representative wavelengths (320 and 500 nm) as a function of zenith and azimuth angle as polar plots (further denoted as sky maps). The black dots in the SCCD sky map represent the measuring pattern. In the MUDIS sky maps, the difference of MUDIS to SCCD sky radiance measurements is given in per cent. The 23 missing numbers of the pattern are measurement points that have been removed due to broken fibres (4 points), high stray light (12 points) and oversaturation in the circumsolar region (7 points). At 500 nm, sky radiance

S Riechelmann *et al*
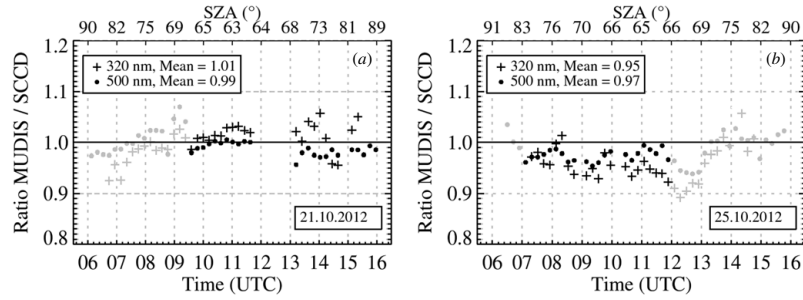
Figure 5. Ratio of diurnal spectral actinic irradiance measured with MUDIS and SCCD at 320 and 500 nm. In (*a*), measurements during a cloudless sky, period from 09:30 to 16:00 UTC on 21 October 2012 are marked with black symbols. In (*b*), the overcast period ranges from 07:00 to 12:00 UTC on 25 October 2012. In both plots, grey-marked ratios correspond to other sky conditions like broken clouds. The SZA corresponding to the measurement time is plotted in the upper *x*-axis.
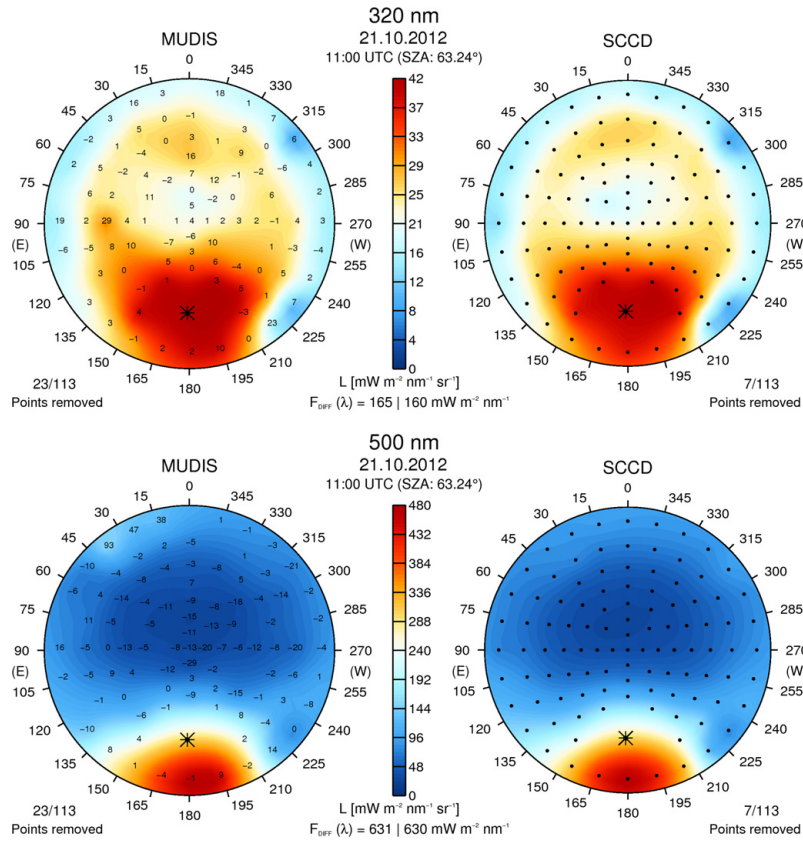
Figure 6. Spectral sky radiance as a function of zenith and azimuth angle for 320 and 500 nm measured with MUDIS and SCCD under cloudless sky on 21 October 2012 at 11:00 UTC. The black dots plotted in the SCCD sky map represent the scan pattern. Numbers plotted in the MUDIS sky map represent the difference between corresponding MUDIS and SCCD measuring points in per cent. The sun symbol marks the position of the sun at the beginning of the sky scan.

measured near the zenith with MUDIS is lower compared to the SCCD, which seems to be a systematic difference for dark blue regions of the sky.

Figure 7 shows the spectral sky radiance distribution of a sky covered with stratocumulus clouds at 320 and 500 nm measured with MUDIS and SCCD at noon time analogous
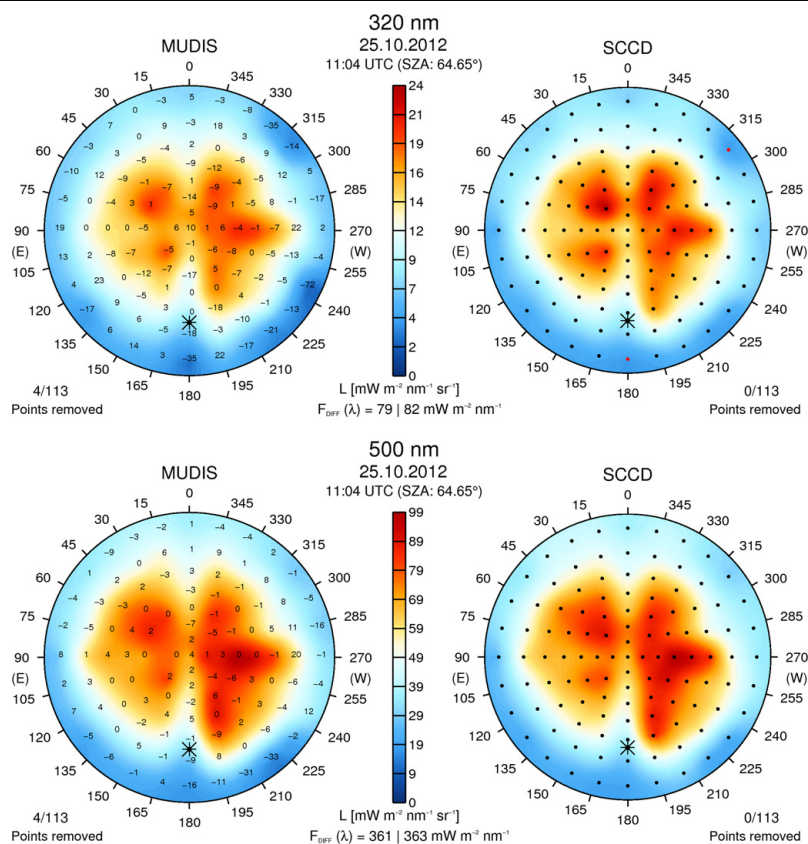
5

Figure 7. Spectral sky radiance as a function of zenith and azimuth angle for 320 and 500 nm measured with MUDIS and SCCD under overcast sky on 25 October 2012 at 11:04 UTC. The black dots plotted in the SCCD sky map represent the scan pattern. Red points are below 5 mW m^{-2} nm^{-1} sr^{-1}. Numbers plotted in the MUDIS sky map represent the difference between corresponding MUDIS and SCCD measuring points in per cent. The sun symbol marks the position of the sun at the beginning of the sky scan.

to figure 6. Clouds lead to a higher spatial and temporal variation of sky radiance compared to cloudless sky. Due to the absence of direct sunlight, no points had to be removed due to oversaturation and stray light, leaving four points removed due to broken fibres. Despite the different FOVs and acquisition times, the measured sky radiance as a function of zenith and azimuth angle of both instruments agrees well.

Histograms of MUDIS/SCCD sky radiance ratios at 320 and 500 nm of the cloudless time period on 21 October (09:30–16:00 UTC) and during overcast sky on 25 October (06:00–14:00 UTC) are shown in figure 8. MUDIS data points that are compromised by broken fibres, affected by high stray light, oversaturated in the circumsolar region or measured spectral radiance of less than 5 mW m^{-2} nm^{-1} sr^{-1} are removed from the dataset. Measurements performed at 84° zenith angle are partly obscured by obstacles like trees, thus leading to high deviations due to the different instrument FOVs. These points and outliers greater than four times the standard deviation (4σ) are also removed from the dataset. The bias between MUDIS and SCCD radiance under cloudless sky on 21 October is 1.7%

with a 1σ standard deviation of 6.1% at 320 nm and −4.4% with a 1σ standard deviation of 8.7% at 500 nm. The 500 nm ratios show a minor maximum at 0.9 which is connected to low values of MUDIS measuring regions of dark blue sky as shown in figure 6. For overcast sky on 25 October the difference is −4.7% with a 1σ standard deviation of 9.9% at 320 nm and −1.6% with a 1σ standard deviation of 6.7% at 500 nm.

3.3. Variation of sky radiance during sky scans

An example of the rapid change of the spectral sky radiance with time is shown in figure 9. Two MUDIS sky captures performed at 11:04 and 11:16 UTC are plotted. It is the same time period in which the SCCD sky scan discussed in figure 8 was performed. Sky radiance at 500 nm increases in this time period by up to 103% while the actinic irradiance increased by up to 41%. Such rapid changes demonstrate the advantage of the MUDIS instrument, which is capable of measuring the spectral sky radiance as a function of zenith and azimuth

S Riechelmann *et al*
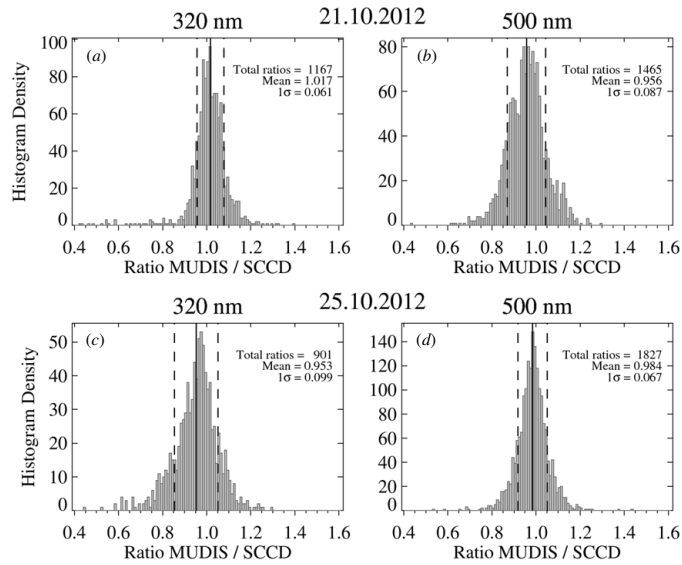
Figure 8. Histograms of MUDIS/SCCD spectral sky radiance ratios at 320 and 500 nm for the cloudless sky period on 21 October (*a*), (*b*) and for an overcast sky period on 25 October (*c*), (*d*). The vertical dashed lines show the corresponding standard deviations. The mean of all examined ratios is represented by the vertical solid lines.
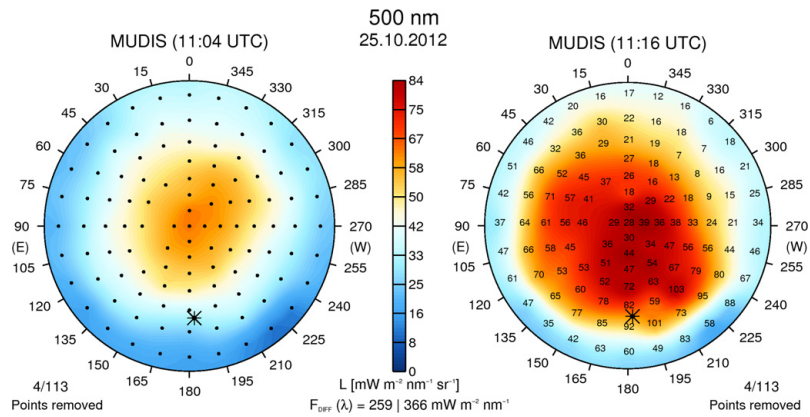
Figure 9. Spectral sky radiance at 500 nm measured with MUDIS under overcast sky on 25 October 2012 at 11:04 and 11:16 UTC. The numbers in the right plot show the increase in percent of the sky radiance at 11:16 UTC compared to the measurements at 11:04 UTC.

angle within seconds, rather than in minutes, compared to CCD array-based scanning instruments.

4. Conclusions

Spectral sky radiance as a function of zenith and azimuth angle has been measured with the novel non-scanning MUDIS and has been intercalibrated and compared with measurements performed by a scanning CCD array spectroradiometer. Actinic irradiance calculated from radiance measurements of both instruments shows a deviation of less than 6% under cloudless sky and less than 8% during overcast

sky. Histograms of sky radiance measurements at two representative wavelengths (320 and 500 nm) show good agreement between both instruments. Despite the inability to measure the circumsolar region with high spatial resolution, the MUDIS bare fibre entrance optics dome with a FOV of 10.6°–18.4° performs well compared to the 5° FOV SCCD entrance optics under various sky conditions. The development of a system capable of measuring sky radiance as a function of zenith and azimuth angle in seconds rather than minutes enables new possibilities to study the spectral influence of fast changing cloud conditions without the disadvantages of scanning processes. MUDIS measurements have been

S Riechelmann *et al*

evaluated for wavelengths above 320 nm. The evaluation of lower wavelengths was limited by the low radiance levels occurring in late October at these wavelengths.

Acknowledgments

References

Beringer S, Schilke H, Lohse I and Seckmeyer G 2011 Case study showing that the tilt angle of photovoltaic plants is nearly irrelevant *Sol. Energy* **85** 470–6

Blumthaler M, Gröbner J, Huber M and Ambach W 1996 Measuring spectral and spatial variations of UVA and UVB sky radiance *Geophys. Res. Lett.* **23** 547–50

Cordero R R, Damiani A, Da Silva L, Laroze D and Labbe F 2013 Spectral UV radiance measured at a coastal site: a case study *Photochem. Photobiol. Sci.* **12** 1193–201

Davis C *et al* 2002 Ocean PHILLS hyperspectral imager: design, characterization, and calibration *Opt. Express* **10** 210–21

Dubovik O and King M D 2000 A flexible inversion algorithm for retrieval of aerosol optical properties from Sun and sky radiance measurements *J. Geophys. Res.: Atmos.* **105** 20673–96

Dunagan S, Johnson R, Zavaleta J, Russell P, Schmid B, Flynn C, Redemann J, Shinozuka Y, Livingston J and Segal-Rosenhaimer M 2013 Spectrometer for sky-scanning sun-tracking atmospheric research (4STAR) Instrument technology *Remote Sensing* **5** 3872–95

Hardeberg J Y, Schmitt F and Brettel H 2002 Multispectral color image capture using a liquid crystal tunable filter *Opt. Eng.* **41** 2532–48

Hirsch E, Agassi E and Koren I 2012 Determination of optical and microphysical properties of thin warm clouds using ground based hyper-spectral analysis *Atmos. Meas. Tech.* **5** 851–71

Hönninger G, von Friedeburg C and Platt U 2004 Multi axis differential optical absorption spectroscopy (MAX-DOAS) *Atmos. Chem. Phys.* **4** 231–54

Isaaks E H and Srivastava R M 1989 *An Introduction to Applied Geostatistics* (New York: Oxford University Press)

Jäkel E, Wendisch M, Blumthaler M, Schmitt R and Webb A R 2007 A CCD spectroradiometer for ultraviolet actinic radiation measurements *J. Atmos. Ocean. Technol.* **24** 449–62

Kouremeti N, Bais A, Kazadzis S, Blumthaler M and Schmitt R 2008 Charge-coupled device spectrograph for direct solar irradiance and sky radiance measurements *Appl. Opt.* **47** 1594–607

Kreuter A and Blumthaler M 2009 Stray light correction for solar measurements using array spectrometers *Rev. Sci. Instrum.* **80** 096108

Kuchinke C, Fienberg K and Nunez M 2004 The angular distribution of UV-B sky radiance under cloudy conditions: a comparison of measurements and radiative transfer calculations using a fractal cloud model *J. Appl. Meteorol.* **43** 751–61

Kylling A *et al* 2003 Actinic flux determination from measurements of irradiance *J. Geophys. Res.: Atmos.* **108** 4506

Lantz K *et al* 2008 2003 North American interagency intercomparison of ultraviolet spectroradiometers: scanning and spectrograph instruments *J. Appl. Remote Sens.* **2** 023547

Pisani M and Zucco M E 2009 Compact imaging spectrometer combining Fourier transform spectroscopy with a Fabry–Perot interferometer *Opt. Express* **17** 8319–31

Pissulla D *et al* 2009 Comparison of atmospheric spectral radiance measurements from five independently calibrated systems *Photochem. Photobiol. Sci.* **8** 516–27

Röder A, Kuemmerle T and Hill J 2005 Extension of retrospective datasets using multiple sensors an approach to radiometric intercalibration of landsat TM and MSS data *Remote Sens. Environ.* **95** 195–210

Román R, Antón M, Cazorla A, de Miguel A, Olmo F J, Bilbao J and Alados-Arboledas L 2012 Calibration of an all-sky camera for obtaining sky radiance at three wavelengths *Atmos. Meas. Tech.* **5** 2013–24

Seckmeyer G, Bais A, Bernhard G, Blumthaler M, Drüke S, Kiedron P, Lantz K, McKenzie R L and Riechelmann S 2010 Instruments to measure solar ultraviolet radiation, Part 4: array spectroradiometers *WMO, Global Atmospheric Watch* (Geneva: World Meteorological Organization) p 43

Seckmeyer G, Schrempf M, Wieczorek A, Riechelmann S, Graw K, Seckmeyer S and Zankl M 2013 A novel method to calculate solar UV exposure relevant to vitamin D production in humans *Photochem. Photobio.* **89** 974–83

Tohsing K, Schrempf M, Riechelmann S, Schilke H and Seckmeyer G 2013 Measuring high-resolution sky luminance distributions with a CCD camera *Appl. Opt.* **52** 1564–73

Weihs P, Webb A R, Hutchinson S J and Middleton G W 2000 Measurements of the diffuse UV sky radiance during broken cloud conditions *J. Geophys. Res.: Atmos.* **105** 4937–44

Wuttke S and Seckmeyer G 2006 Spectral radiance and sky luminance in Antarctica: a case study *Theor. Appl. Climatol.* **85** 131–48

8

Bibliography

Bayer, B. E., 1976: Color imaging array. *Patent*, **US 555477**.

Bedard, N., et al., 2013: Multimodal snapshot spectral imaging for oral cancer diagnostics: a pilot study. *Biomedical Optics Express*, **4 (6)**, 938–949.

Beringer, S., H. Schilke, I. Lohse, and G. Seckmeyer, 2011: Case study showing that the tilt angle of photovoltaic plants is nearly irrelevant. *Solar Energy*, **85 (3)**, 470–476.

Blumthaler, M., J. Gröbner, M. Huber, and W. Ambach, 1996: Measuring spectral and spatial variations of UVA and UVB sky radiance. *Geophysical Research Letters*, **23 (5)**, 547–550.

Cordero, R. R., A. Damiani, L. Da Silva, D. Laroze, and F. Labbe, 2013: Spectral UV radiance measured at a coastal site: a case study. *Photochemical & Photobiological Sciences*, **12 (7)**, 1193–1201.

Cordero, R. R., G. Seckmeyer, D. Pissulla, and F. Labbe, 2008: Uncertainty of experimental integrals: Application to the UV index calculation. *Metrologia*, **45 (1)**, 1.

Davis, C., et al., 2002: Ocean PHILLS hyperspectral imager: Design, characterization, and calibration. *Optics Express*, **10 (4)**, 210–221.

Dubovik, O. and M. D. King, 2000: A flexible inversion algorithm for retrieval of aerosol optical properties from sun and sky radiance measurements. *Journal of Geophysical Research: Atmospheres*, **105 (D16)**, 20 673–20 696.

Dunagan, S., et al., 2013: Spectrometer for sky-scanning sun-tracking atmospheric research (4STAR): Instrument technology. *Remote Sensing*, **5 (8)**, 3872–3895.

Grant, R., G. Heisler, and W. Gao, 1997: Clear sky radiance distributions in ultraviolet wavelength bands. *Theoretical and Applied Climatology*, **56 (3-4)**, 123–135.

Hagen, N., R. T. Kester, L. Gao, and T. S. Tkaczyk, 2012: Snapshot advantage: a review of the light collection improvement for parallel high-dimensional measurement systems. *Optical Engineering*, **51 (11)**.

Hagen, N. and M. W. Kudenov, 2013: Review of snapshot spectral imaging technologies. *Optical Engineering*, **52 (9)**, 090 901.

Hardeberg, J. Y., F. Schmitt, and H. Brettel, 2002: Multispectral color image capture using a liquid crystal tunable filter. *Optical Engineering*, **41 (10)**, 2532–2548.

Hirsch, E., E. Agassi, and I. Koren, 2012: Determination of optical and microphysical properties of thin warm clouds using ground based hyper-spectral analysis. *Atmospheric Measurement Techniques*, **5 (4)**, 851–871.

Hönninger, G., C. von Friedeburg, and U. Platt, 2004: Multi axis differential optical absorption spectroscopy (MAX-DOAS). *Atmospheric Chemistry and Physics*, **4 (1)**, 231–254.

Isaaks, E. H. and R. M. Srivastava, 1989: *An Introduction to Applied Geostatistics*. Oxford University Press, New York.

Jäkel, E., M. Wendisch, M. Blumthaler, R. Schmitt, and A. R. Webb, 2007: A CCD spectroradiometer for ultraviolet actinic radiation measurements. *Journal of Atmospheric and Oceanic Technology*, **24 (3)**, 449–462.

Kapany, N. S., 1958: Fiber optics. *Concepts of Classical Optics*, H. M. Foley and M. A. Ruderman, Eds., Strong, J., San Francisco, 553–579.

Kouremeti, N., A. Bais, S. Kazadzis, M. Blumthaler, and R. Schmitt, 2008: Charge-coupled device spectrograph for direct solar irradiance and sky radiance measurements. *Applied Optics*, **47 (10)**, 1594–1607.

Kreuter, A. and M. Blumthaler, 2009: Stray light correction for solar measurements using array spectrometers. *Review of Scientific Instruments*, **80 (9)**, 096 108.

Kuchinke, C., K. Fienberg, and M. Nunez, 2004: The angular distribution of UV-B sky radiance under cloudy conditions: A comparison of measurements and radiative transfer calculations using a fractal cloud model. *Journal of Applied Meteorology*, **43 (5)**, 751–761.

Kylling, A., et al., 2003: Actinic flux determination from measurements of irradiance. *Journal of Geophysical Research: Atmospheres*, **108 (D16)**, 4506.

Lantz, K., et al., 2008: 2003 North American interagency intercomparison of ultraviolet spectroradiometers: Scanning and spectrograph instruments. *Journal of Applied Remote Sensing*, **2 (1)**, 023 547–023 547.

Niedzwiedz, A., 2013: Personal communication.

Pisani, M. and M. E. Zucco, 2009: Compact imaging spectrometer combining fourier transform spectroscopy with a fabry-perot interferometer. *Optics Express*, **17 (10)**, 8319–8331.

Pissulla, D., 2006: Development of instrumentation measuring sky radiance. Diploma thesis, Leibniz Universität Hannover, Institut für Meteorologie und Klimatologie, Herrenhäuser Straße 2, 30419 Hannover.

Pissulla, D., et al., 2009: Comparison of atmospheric spectral radiance measurements from five independently calibrated systems. *Photochemical & Photobiological Sciences*, **8 (4)**, 516–527.

Riechelmann, S., M. Schrempf, and G. Seckmeyer, 2013: Simultaneous measurement of spectral sky radiance by a non-scanning multidirectional spectroradiometer (MUDIS). *Measurement Science and Technology*, **24 (12)**, 125 501.

Román, R., M. Antón, A. Cazorla, A. de Miguel, F. J. Olmo, J. Bilbao, and L. Alados-Arboledas, 2012: Calibration of an all-sky camera for obtaining sky radiance at three wavelengths. *Atmospheric Measurement Techniques*, **5 (8)**, 2013–2024.

Sansonetti, C. J., M. L. Salit, and J. Reader, 1996: Wavelengths of spectral lines in mercury pencil lamps. *Applied Optics*, **35 (1)**, 74–77.

Seckmeyer, G., 1989: Spektralradiometer für die ökologische Pflanzenforschung. *Licht*, **41**, 7–8.

Seckmeyer, G., M. Schrempf, A. Wieczorek, S. Riechelmann, K. Graw, S. Seckmeyer, and M. Zankl, 2013: A novel method to calculate solar UV exposure relevant to vitamin D production in humans. *Photochemistry and Photobiology*, **89 (4)**, 974–983.

Seckmeyer, G., et al., 2010: Instruments to measure solar ultraviolet radiation, part 4: Array spectroradiometers. Tech. rep., World Meteorological Organization.

Sharpe, M. R. and D. Irish, 1978: Stray light in diffraction grating monochromators. *Optica Acta: International Journal of Optics*, **25 (9)**, 861–893.

Shortis, M. R., J. W. Seager, E. S. Harvey, and S. Robson, 2004: Influence of Bayer filters on the quality of photogrammetric measurement. *Videometrics VIII*, J.-A. Beraldin, S. F. El-Hakim, A. Gruen, and J. S. Walton, Eds., Society of Photo-Optical Instrumentation Engineers (SPIE) Conference Series, Vol. 5665, 164–171.

Tohsing, K., M. Schrempf, S. Riechelmann, H. Schilke, and G. Seckmeyer, 2013: Measuring high-resolution sky luminance distributions with a CCD camera. *Applied Optics*, **52 (8)**, 1564–1573.

Weihs, P., A. R. Webb, S. J. Hutchinson, and G. W. Middleton, 2000: Measurements of the diffuse UV sky radiance during broken cloud conditions. *Journal of Geophysical Research: Atmospheres*, **105 (D4)**, 4937–4944.

Wuttke, S., 2005: Radiation conditions in an Antarctic environment. PhD thesis, Leibniz Universität Hannover, Institut für Meteorologie und Klimatologie, Herrenhäuser Straße 2, 30419 Hannover.

Wuttke, S. and G. Seckmeyer, 2006: Spectral radiance and sky luminance in Antarctica: a case study. *Theoretical and Applied Climatology*, **85 (3-4)**, 131–148.

Wuttke, S., G. Seckmeyer, G. Bernhard, J. Ehramjian, R. McKenzie, P. Johnston, and M. O'Neill, 2006: New spectroradiometers complying with the NDSC standards. *Journal of Atmospheric and Oceanic Technology*, **23 (2)**, 241–251.

Acknowledgments

First of all, I want to thank Prof. Dr. Gunther Seckmeyer for his kind support over the years of my stay at the IMuK. Back in the days as a student I got the opportunity to participate in an intercomparison campaign in Thessaloniki and I was welcomed very friendly by Mr. Seckmeyer, his working group and the participating radiation community. If I look back on the years since, I remember a lot of helpful discussions, advices and moments of joy during our work together. During my time as a PhD student I had the freedom to try out many of my own ideas in a very interesting working field. I never took that for granted and therefore I am very thankful for the degree of freedom you put your trust in me and my decisions.

My sincere thanks also go to my former and current colleagues I've worked with at the IMuK. I especially thank Michael Schrempf for being awesome, both as a colleague and as a friend. He helped me out countless times when I needed help at campaigns and greatly contributed to many scientific discussions which were crucial for my thesis. Many thanks also to Ansgar Stührmann for being such a great room colleague and to Angelika Niedzwiedz for helping me out on many occasions in the lab and during the preparation of meetings.

Working in an experimental group is impossible without technical support, therefore I greatly appreciate the help of Holger Schilke – without you I most certainly would only have conducted zenith radiance comparisons due to the lack of a working sky scanner. Especially important for the success of this thesis was the help Uli Meyer provided to me. By fruitful discussions and his outstanding technical skills countless technical issues connected to the development of MUDIS could be solved, if someone reminds me of MacGyver, it is Uli.

I am also grateful that several people took the time to read my thesis and provide me with a lot of helpful advices, namely Matthias Brakebusch, Susanne Benze, Michael Schrempf, Ansgar Stührmann, Darius Pissulla and Theres Riechelmann. I owe you one!

Last but not least I want to thank my wife Theres for always supporting me with patience and tolerance for my strange day rhythms in the final writing phase... and for never leaving the room when I started countless scientific discussions concerning my thesis. Thank you for so much!

Curriculum Vitae

Personal Data

Name	Stefan Riechelmann
Date of birth	21.01.1982
Place of birth	Burgwedel
Family status	married

Working Career

since 12/2008	Research associate at Leibniz Universität Hannover
04/2010 - 04/2012	Representative of scientific associates at IMuK
05/2005 - 06/2005	Student assistant at Leibniz Universität Hannover
06/2004 - 09/2004	Traineeship at Volkswagen Nutzfahrzeuge Hannover
06/2003 - 09/2003	Temporary worker at Hannover Rueckversicherungs-AG
06/2002 - 09/2002	Temporary worker at Hannover Rueckversicherungs-AG
08/2001 - 06/2002	Civilian service at DRK-Sozialstation Wedemark

Education

since 12/2008	PhD student in meteorology at Leibniz Universität Hannover
10/2002 - 10/2008	Diploma student in meteorology at Leibniz Universität Hannover
06/2001	Abitur at Gymnasium Mellendorf

Stays Abroad

02/2011	Participant of a measurement campaign at King George Island, Antarctica
07/2006	Participant of a measurement campaign at Aristotle University of Thessaloniki, Greece

List of Publications

1. Riechelmann, S., M. Schrempf, and G. Seckmeyer, 2013: Simultaneous measurement of spectral sky radiance by a non-scanning multidirectional spectroradiometer (MUDIS). *Measurement Science and Technology*, **24 (12)**, 125 501.

2. Tohsing, K., M. Schrempf, S. Riechelmann und G. Seckmeyer, 2014: Validation of spectral sky radiance derived from all-sky camera images - a case study. *Atmos. Meas. Tech. Discuss.*, **7, 69-97**.

3. Voskrebenzev, A., S. Riechelmann, A. Bais, H. Slaper und G. Seckmeyer 2014: Estimating probability distributions of solar irradiance. *Theoretical and Applied Climatology* (accepted).

4. Cordero, R., G. Seckmeyer, A. Damiani, S. Riechelmann, J. Rayas, F. Labbe und D. Laroze, 2014: The world's highest levels of surface UV. *Photochemical & Photobiological Sciences*, Photochem. Photobiol. Sci., **13, 70-81**

5. Seckmeyer, G., M. Schrempf, A. Wieczorek, S. Riechelmann, K. Graw, S. Seckmeyer und M. Zankl, 2013: A Novel Method to Calculate Solar UV Exposure Relevant to Vitamin D Production in Humans. *Photochemistry and Photobiology* **89,** 974-983.

6. Tohsing, K., M. Schrempf, S. Riechelmann, H. Schilke und G. Seckmeyer, 2013: Measuring high-resolution sky luminance distributions with a CCD camera. *Applied Optics* **52,** 1564-1573.

7. Cordero, R. R., A. Damiani, G. Seckmeyer, S. Riechelmann, F. Labbe, D. Laroze und F. Garate, 2013: Satellite-derived UV climatology at Escudero Station, Antarctic Peninsula. *Antarctic Science*, **25**, 791-803

8. Seckmeyer, G., M. Klingebiel, S. Riechelmann, I. Lohse, R. L. McKenzie, J. Ben Liley, M. W. Allen, A.-M. Siani und G. R. Casale (2012), A Critical Assessment of Two Types of Personal UV Dosimeters. *Photochemistry and Photobiology* **88,** 215-222.

9. Cordero, R. R., G. Seckmeyer, S. Riechelmann, A. Damiani und F. Labbe (2012), Monte Carlo-based uncertainty analysis of UV array spectroradiometers. *Metrologia* **49,** 745.

10. Seckmeyer, G., A. Bais, G. Bernhard, M. Blumthaler, S. Drueke, P. Kiedron, K. Lantz, R. L. McKenzie und S. Riechelmann, 2010: Instruments to Measure Solar Ultraviolet Radiation, Part 4: Array Spectroradiometers. *In WMO, Global Atmospheric Watch.* **pp. 43**. World Meteorological Organization, Geneva.

Conference Contribution

Riechelmann, S., M. Schrempf, G. Seckmeyer, (2013) Spektrale Strahldichtemessungen: Einfluss des Oeffnungswinkels verwendeter Eingangsoptiken auf das Messergebnis. *DACH*, Innsbruck, Austria.